Measuring and tuning specific particle aggregation rates using an optomagnetic cluster experiment

Haenen, Stijn R.R.

Award date:
2019

Measuring and tuning specific particle aggregation rates using an optomagnetic cluster experiment

Master Thesis

S.R.R. Haenen

Supervisors: M.R.W. Scheepers & dr. L.J. van IJzendoorn

Molecular Biosensing for Medical Diagnostics (MBx)
Department Applied Physics - University of Technology Eindhoven

TU/e

Abstract

Biosensing based on particle mobility (BPM) is a biosensing technique with the potential for continuous monitoring. With this method the presence of a target molecule is detected by a change in the mobility of a tethered particle. One of the challenges of this system is to make it work properly for target molecules that have a too strong affinity to their recognition molecule. Therefore the need exists for a way to tune the affinity of a binder to its target in the BPM geometry. In this project it was investigated if the affinity of a model target-binder complex can be tuned using the steric repulsion between PEG coated surfaces, measured in a particle aggregation experiment.

A DNA sandwich assay was designed of which the specific particle aggregation rate can be measured with the optomagnetic cluster (OMC) experiment. In the OMC experiment magnetic fields are used to accelerate particle aggregation kinetics and light scattering is used to detect particle clustering. Streptavidin coated silica particles were functionalized with biotinylated DNA docking strands. An analyte DNA molecule, which is complementary to the DNA docking strands on the particles, was used to induce a specific interaction between the particles. The superparamagnetic silica microparticles were selected, out of a selection of three different particles, as the most suitable particle for the OMC experiment, due to their highly monodisperse size distribution and smooth particle surface. Using a four-step magnetic actuation protocol particle aggregation rates of these silica particles can be measured.

The non-specific interactions between the silica particles have been reduced with BSA (bovine serum albumin) and casein molecules. The non-specific aggregation rate was reduced to $(6 \pm 3) \times 10^{-3}\,\mathrm{s}^{-1}$. The maximum experimentally measurable aggregation rate in the OMC experiment is $1 \times 10^{-1}\,\mathrm{s}^{-1}$, which implies a dynamic range of over one order of magnitude. The magnetically induced specific aggregation rates have been measured as a function of the analyte concentration. The result of this measurement showed a clear difference between the non-specific interaction and specific interaction. At low analyte concentrations, the probability of aggregation increases with the analyte concentration, at higher concentrations the probability of aggregation decreases with the concentration due to saturation of the docking strands.

To tune the particle aggregation rate, particle have been coated with PEG molecules of different molecular weights: 5, 10, 20, and $30\,\mathrm{kDa}$. For the particles with a $30\,\mathrm{kDa}$ PEG functionalization, a significant decrease in the aggregation rate was observed. A simulation of the aggregation process of the DNA model system has been performed to interpret the measurement results. According to the simulation, the decrease in aggregation rate is caused by either a decrease in the association rate between a single docking and analyte DNA strand, which means that the affinity is decreased, or by an increase of the inter particle distance, or by a combination of both effects. In order to determine which of the two effects causes the decrease in aggregation, further research is necessary.

Contents

Introduction

Fast and accurate diagnostics are key to provide better health care. This can be achieved with point-of-care (POC) diagnostics instead of in-vitro diagnostics at (external) laboratories[1]. Analysing for example blood samples, or even continuously monitoring of biomarkers can be done with POC devices such as biosensors[2]. A biosensor measures the concentrations of target molecules, such as proteins, drugs, or a microbe, in a sample taken from the body. This sample can be for example a blood-, saliva-, or urine-sample[3]. The well-known continuous glucose monitoring system is just one example of the ongoing developments in the biosensing field[4, 5, 6].

Recently a new biosensing technique for continuous monitoring was proposed based on measuring particle mobility: BPM. This system is based on tethered particle motion (TPM) where the position of a particle, that is tethered to a surface, is tracked over time[7]. When a particle makes a second bond via a target molecule to the surface, the range of motion of the particle is reduced, which causes a decrease in the mobility of the particle. When the bond breaks, the range of motion of the particle increases again. The target concentration is quantified by the number of switching events between the freely tethered state and the bound states. In case of a high affinity binder, the equilibrium in the reaction between the bound and free state has a predominance to the bound state. The particle will be longer in the bound state which results in a low number of switching events. This makes it difficult to measure high affinity targets. In order to get this equilibrium more to the free state, the dissociation should be increased and the association rate decreased.

Tuning the affinity between the target molecule and the binders usually requires complex and effortful protein engineering. In this project a possibly simpler way of tuning the specific aggregation rate is investigated. For this purpose a cluster experiment is performed using DNA functionalized particles that can aggregate specifically via a complementary analyte DNA molecule. The first goal of this project is to suppress the non-specific interactions between the particles and test if it is possible to distinguish the specific from the non-specific aggregation. Subsequently the possibility of tuning the specific aggregation rate is investigated. This is done by coating the particles with PEG molecules in a higher surface density than the DNA molecules, such that each DNA molecule has several PEG neighbours. PEG is commonly used to make surfaces antifouling and to decrease non-specific interactions between particle surfaces, working as an entropic spring[8]. The entropic repulsion between PEG coated surfaces may lead to a decrease in the association rate between the target on one particle and the binder on the other particle.

The formation of particle dimers is induced and measured using an optomagnetic cluster (OMC) experiment. The OMC experiment is based on accelerated particle aggregation using magnetic attraction and quantifying dimer concentrations using optomagnetic readout based on light scattering on rotating dimers, developed by Ranzoni et al[9]. Scheepers et al.[10] developed a measurement protocol to quantify the particle aggregation rate, but they only measured non-specific aggregation rates. In this project a model system is used to measure specific aggregation rates with OMC experiments. This model system (see Fig. 1) consists of streptavidin coated magnetic particles that are functionalized with biotinylated DNA docking strands. In an external magnetic field the particles become magnetized and due to the dipole-dipole interaction the particles form magnetic dimers. In the presence of the target DNA molecule, which is the analyte strand, a bond can be formed between the particles, resulting in a chemical dimer. By measuring the number of chemical dimers that are formed in a certain time, the aggregation rate can be determined.

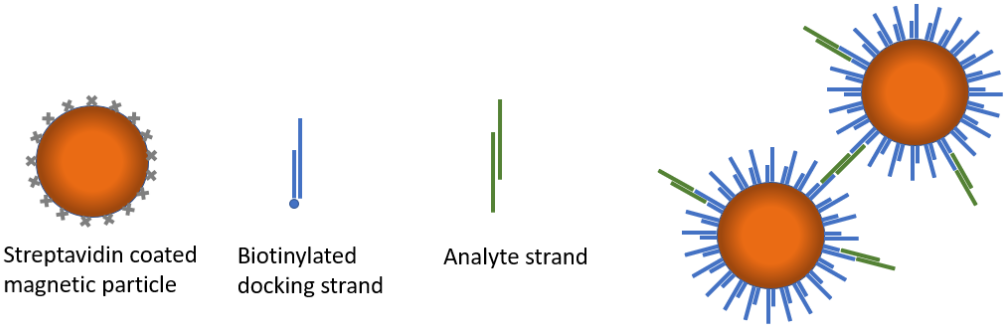

Fig. 1: **The model system that is used in this project.** The model consists of streptavidin coated microparticles that are functionalized with biotinylated docking strands. Two functionalized particles can bind to each other via an analyte strand. The docking and analyte strands consists of hybridized single DNA strands

Chapter 1 explains the multi-step particle aggregation process, the superparamagnetic properties, and the binding kinetic of DNA molecules. In chapter 2, the materials and methods are given. In chapter 3, the principles of the OMC experiments are explained in detail, and it is described how the dimer concentration and aggregation rate can be determined. Chapter 4 focuses on which particle type is the most suitable for the OMC experiments in this projects. Chapter 5 focuses on the effect of the functionalization on the non-specific and specific aggregation. The measurements of the aggregation rates of this project are given in this chapter. In chapter 6 a simulation of the chemical aggregation is discussed, which is used to interpret the experimental results as will be described in chapter 7. The conclusion of this project is given in chapter 8.

Chapter 1

Theory

The optomagnetic cluster (OMC) experiment used in this project is based on the formation of magnetic and chemical particle dimers. The formation process of a chemical dimer, in the absence or presence of an interparticle interaction, involves several steps which are explained in the first two sections of this chapter. To accelerate the dimer formation process, superparamagnetic particles are used. The physics behind this magnetic acceleration is explained in the third section. Quantifying dimer concentrations happens with light scattering on rotating dimers. The torques that a rotating dimer experiences are discussed in the fourth section. The particles of a dimer can bind chemically to each other via complementary DNA strands. The binding kinetics of DNA molecules is explained in the fifth section of this chapter. The last section is about the properties of a PEG molecule.

1.1 Thermal particle aggregation

Two individual particles (monomers) can react into a two-particle cluster (dimer), with an aggregation rate κ_{agg}. The dimer that is formed can subsequently dissociate with a dissociation rate κ_{dis}, see equation 1.1.

$$m_1 + m_2 \underset{k_{dis}}{\overset{k_{agg}}{\rightleftharpoons}} d \tag{1.1}$$

This aggregation process is schematically depicted in more detail in Fig. 1.1. Forming a chemical dimer of the particles involves three consecutive steps: A diffusion step in which two particles encounter each other, an orientation step in which the reactive sites on the particles become aligned, and a chemical binding step in which particles form a bond. Each step will be discussed in detail.

The first step is the diffusional encounter step, which describes the collision rate of particles due to random Brownian motion. The average encounter rate of particles that move solely due to Brownian motion can be

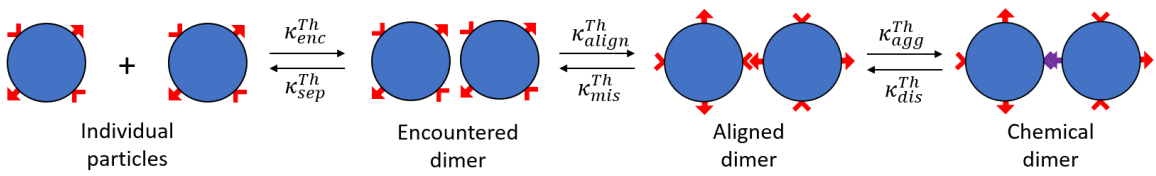

Fig. 1.1: **Schematic representation of the chemical dimer formation.** The three steps that are involved in the formation of a chemical dimer out of two individual particles are: the encountering, the alignment step, and the chemical aggregation. Each step is quantified with a thermally induced rate.

calculated with the diffusion limited rate equation[11]

$$\kappa_{enc}^{Th} = \frac{4k_BT}{3\eta}, \tag{1.2}$$

where k_BT is the thermal energy and η is the viscosity of the medium. The encounter rate depends on the temperature and is independent on the size of the particles. The separation rate κ_{sep}^{Th} describes the rate at which two collided particles move away from each other. A minimal distance has to be defined, at which the particles can be considered as individual. In the work of Biancaniello et al. [12] and Wang et al. [13] it is demonstrated that at a distance of $40\,\mathrm{nm}$ the interaction energy of two particles of $500\,\mathrm{nm}$ is less than $1\,\mathrm{k_BT}$. Therefore $40\,\mathrm{nm}$ is used as the minimal distance at which two particles are separated from each other. The typical time to diffuse this distance can be calculated using the equation for Brownian motion:

$$\langle \Delta x^2 \rangle = 6Dt = \frac{k_BT}{\pi\eta R}\, t \tag{1.3}$$

in which D is the diffusion constant. The estimated thermal separation rate is the inverse of the typical time and is given by

$$\kappa_{sep}^{Th} = \frac{k_BT}{\langle \Delta x^2 \rangle \pi\eta R} \tag{1.4}$$

For particles that are used in this project, with a radius $R = 250\,\mathrm{nm}$, that move in a water-based medium ($\eta = 1 \times 10^{-3}\,\mathrm{Pa \cdot s}$) at room temperature, the encounter rate is about $5 \times 10^{-18}\,\mathrm{m^3\,s^{-1}}$, which is the same as $3 \times 10^{9}\,\mathrm{M^{-1}\,s^{-1}}$. The separation rate is in this case $3 \times 10^{3}\,\mathrm{s^{-1}}$, which corresponds to a typical existence time of an encountered dimer of about $300\,\mu\mathrm{s}$.

The next step in the particle aggregation process is the orientation step. To form a chemical bond between the molecules on the surface of the particles, the molecules should be close to each other. Therefore the particles have to align their reactive spots. This might happen due to Brownian rotation, which is the random rotation of the particles. The typical existence time of an encountered dimer is $300\,\mu\mathrm{s}$, which is much shorter than the typical time of a full rotation that can be calculated with [14]

$$t_{rot} = \frac{4\pi R^3 \eta}{k_BT} \tag{1.5}$$

For a particle with a radius of $250\,\mathrm{nm}$, the typical rotation time is about 50 milliseconds. Within the existence time an encountered dimer, the particles can rotate about 2 degrees. It depends on the surface density of reactive spots whether or not the alignment can happen before the separation. With a low surface density, an aligned dimer will, most likely, be formed out of two individual particles that encounter each other already in the aligned orientation. In the case of a homogeneous reactive surface, the particles are always aligned, which corresponds to an infinite alignment rate and a zero mis-alignment rate (κ_{mis}^{Th}).

The last step in the reaction scheme of Fig. 1.1 is the formation of a chemical dimer out of an aligned dimer. This step describes the reaction between the molecules on the surfaces of the two particles. This reaction is quantified by the thermal aggregation rate κ_{agg}^{Th} and the dissociation rate κ_{dis}^{Th}. The physics behind these two rates is explained in more detail in section 5 of this chapter. This project focuses on the quantification of this very last step in the dimer formation process.

1.2 Magnetically induced particle aggregation

In order to accelerate the particle aggregation process, magnetic particles in combination with an external magnetic field are used. The three different steps of the particle aggregation process are influenced by the magnetic interactions. For example, the encounter step is enhanced due to the attractive dipole-dipole interaction of the magnetic particles. Also the orientation step is different, because the Brownian rotation is

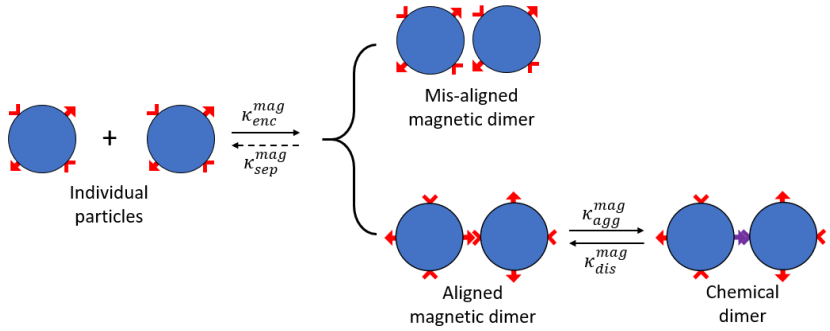

Fig. 1.2: **Schematic representation of the magnetically induced chemical dimer formation**. First a magnetic dimer will be formed, this can be either an aligned or a mis-aligned magnetic dimer. This step is one directional due to the strong dipole-dipole interaction. An aligned magnetic dimer can become a chemical dimer, depending on the magnetically induced aggregation rate κ_{agg}^{mag}. A mis-aligned dimer cannot form a chemical cluster.

suppressed by the interaction between the magnetic field and the magnetic moment of a particle. An overview of the magnetically induced dimer aggregation process is depicted in Fig. 1.2.

The faster encounter step is the result of an attractive interaction between the magnetic particles. In an external magnetic field, the magnetically induced encounter rate is faster than the thermal encounter rate ($\kappa_{enc}^{mag} > \kappa_{enc}^{T}$). The separation of two magnetic particles is very unlikely, the magnetic separation rate $\kappa_{sep}^{T} \to 0$. This is caused by the high magnetic potential of two magnetized particles in proximity, which is much larger than the thermal energy. The magnetic potential of two magnetic particles can be estimated by using equation 1.6 and considering point dipoles. The magnetic potential of two point dipoles at a distance d_0 can be determined by integrating the force, which is induced by the dipole-dipole interaction[15], from infinity to d_0:

$$U_{mag} = \int_{d_0}^{\infty} -\frac{3\mu_0 m_1 m_2}{2\pi r^4} dr = -\frac{\mu_0 m_1 m_2}{2\pi d_0^3}, \tag{1.6}$$

where m_1 and m_2 are the magnetic moments of the two points dipoles (in $\mathrm{A\,m^2}$), r is the distance between the two point dipoles, and μ_0 is the vacuum permeability. In equation 1.6, it is assumed that the two moments of the dipoles are parallel to each other. A typical magnetic moment of $0.5\,\mathrm{fA\,m^2}$ ($\chi_V = 2$, $R = 256\,\mathrm{nm}$, $B = 4\,\mathrm{mT}$) gives a magnetic potential of $-1\,\mathrm{k_B T}$ at a distance of $2.3\,\mu\mathrm{m}$ at room temperature. Decreasing the distance to the diameter of the particles ($511\,\mathrm{nm}$) results is a potential of about $-80\,\mathrm{k_B T}$. Due to this high potential, two encountered magnetic particles, that form a magnetic dimer, cannot be separated by the thermal fluctuations as long as the magnetic field is on. The strong magnetic interaction makes the separation rate of Fig. 1.2 equal to zero.

Every magnetic particle has a certain magnetic anisotropy axis. In an external magnetic field, a particle tends to align this axis to the magnetic field. This alignment suppresses Brownian rotation of the particles. Therefore, it is assumed that the two particles of a magnetic dimer do not rotate with respect to each other. In other words, the contact area of one magnetic dimer is always the same. When the reactive molecules of both particles are located in this contact area, the dimer is aligned well to form a chemical dimer, such a dimer is called an aligned dimer. In the other case, when no or only one particle has its reactive molecules in the contact area, the dimer is called a mis-aligned dimer. Such a dimer cannot transform into a chemical dimer, because the alignment of the molecules on the surface is not correct. The probability of forming an aligned dimer depends on the surface density of reactive spots, the more reactive molecules on the surface the higher the chance of forming an aligned dimer. In the limit of a homogeneous surface coverage, the chance of forming an aligned dimer is equal to one.

An aligned dimer is required for the formation of a chemical dimer, so the reaction has a dead end when a mis-aligned dimer is formed. For an aligned dimer, the magnetically induced aggregation rate κ_{agg}^{mag} is larger than the thermal aggregation rate, and will increase with increasing magnetic field strength, as shown by Scheepers et al.[16]. The magnetically induced aggregation rate is directly related to the thermal aggregation rate.

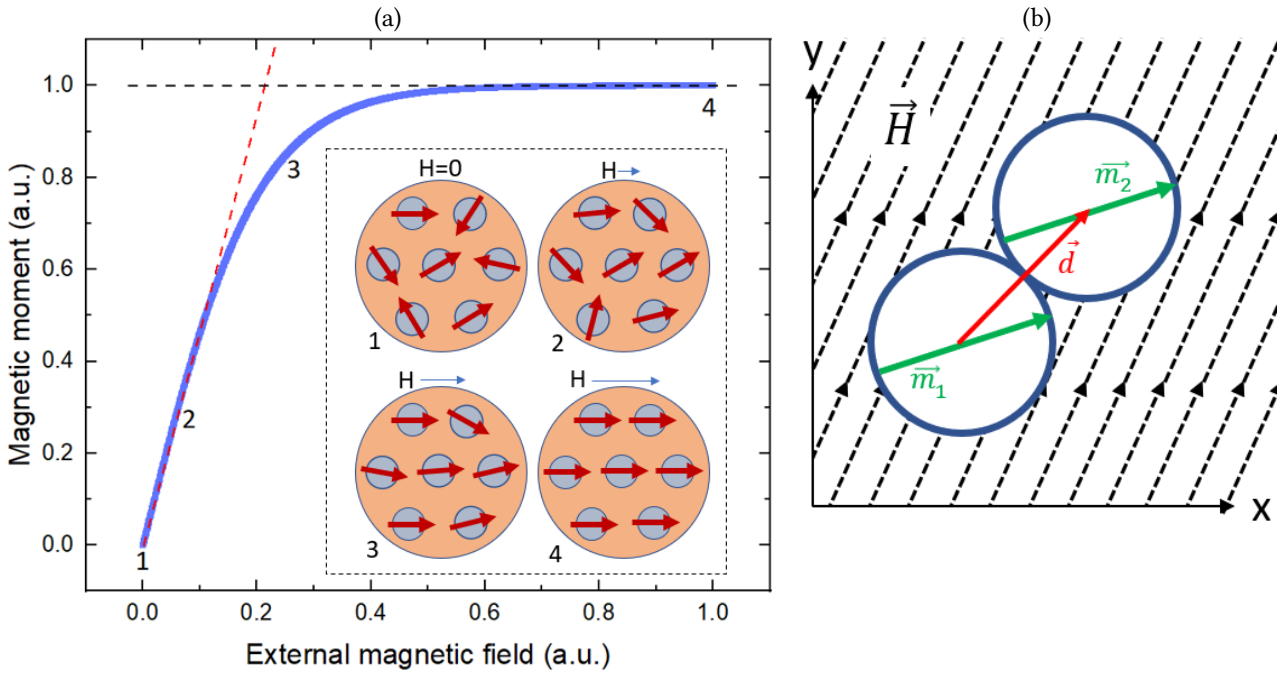

Fig. 1.3: **Magnetic particles in an external magnetic field. (a)** The graph shows the magnetic moment of an ideal superparamagnetic particle against the external magnetic field. The black dashed line corresponds to the saturation magnetization, the slope of the red dashed line is the magnetic susceptibility χ. The insert shows a possible orientation of the grains inside the particles for 4 different magnetic field strengths. **1**: At zero field, the domains of the grains all have a random orientation, which results in a zero net magnetic moment. **2**: At small fields, the moments of the every grain have a preferred orientation but the thermal fluctuations are significant. **3**: At larger fields, the moments have a preferred orientation and the thermal fluctuations become less significant. **4**: At very high fields, all domains are aligned parallel to the field and the thermal induced fluctuations are negligible, the magnetic moment is saturated.
(b) Sketch of a dimer of two particles in a magnetic field, showing the vectors that are used in equation 1.8: the magnetic moments of the two particles $\vec{m_1}$, $\vec{m_2}$, the vector between the two particles $\vec{d}$, and the uniform magnetic field $\vec{H}$.

1.3 Superparamagnetism

The particles used in this project have the property to behave non-magnetic in the absence of a magnetic field, but in the presence of a weak magnetic field the particles become magnetic. This superparamagnetic behaviour is caused by small magnetic grains made of iron-oxide[17]. Each superparamagnetic particle contains many grains that are randomly dispersed in silica or polystyrene matrix. Without an external magnetic field each grain has a non-zero magnetic moment at each point in time, but the direction of the magnetic moment of each grain is random. The typical flipping time of the direction of the magnetic moment, called the Néel relaxation time is strongly dependent on the size of a grain[18]. The relative small grains will flip many times per second, but the larger ones might not flip thermally during the typical time of an experiment. However, due to the random orientation of the magnetic moments of each individual grain, the total magnetization of a particle is zero in the absence of an external magnetic field.

In the presence of an external magnetic field, the magnetic moments of the grains align with the field, such that the net magnetization of the particle become non-zero. At a low external magnetic field strength, the magnetization M of the particle increases linearly with the magnetic field strength H, see equation 1.7. The slope of this linear regime is the magnetic volume susceptibility χ.

$$M = \chi H, \tag{1.7}$$

At higher field strengths, the magnetic moment of the particles saturates, this behaviour is described by

the Langevin curve, see Fig. 1.3a. The maximum moment depends on the saturation magnetization of the magnetic material and the amount of magnetic material in a particle.

By turning on and off an external magnetic field, the magnetic interaction between the particles can be controlled.

1.4 Magnetic and viscous torque

A dimer of two superparamagnetic particles can be forced to rotate in a viscous medium using a rotating external magnetic field. This field induces a magnetic torque on the dimer. The magnetic dimer will follow this rotating field when the magnetic torque is larger than the viscous torque, which is the result of the drag forces that a particle experiences when it moves through a medium. In this section the origin of both torques will be explained in more detail.

The magnetic torque can be determined as follows. The free energy of the system is in a minimum when the magnetic moments of the two particles aligned with the external magnetic field and when the magnetic moments of the two particles are parallel to each other. The total magnetic torque can be determined from the magnetic energy. In the case of a dimer with two particles of the same size R, this energy is given by[19]

$$U_M = -\vec{m}_1 \cdot \mu_0 \vec{H} - \vec{m}_2 \cdot \mu_0 \vec{H} + \frac{\mu_0}{4\pi} \frac{1}{(2R)^3} \left[\vec{m}_1 \cdot \vec{m}_2 - 3(\vec{m}_1 \cdot \hat{d})(\vec{m}_2 \cdot \hat{d}) \right], \tag{1.8}$$

in which μ_0 is the vacuum permeability, $\vec{d}$ is the vector between the two center points of the two particles, $\vec{m}_1$ and $\vec{m}_2$ are the magnetic moments of the two particles, and $\vec{H}$ is the magnetic field strength in $\mathrm{A\,m^{-1}}$. These vectors are depicted in Fig. 1.3b. Equation 1.8 can be simplified with $\vec{A} \cdot \vec{B} = |A||B|cos(\theta)$, where θ is the angle between $\vec{A}$ and $\vec{B}$. This simplification gives

$$\begin{aligned} U_M = &- m_1 \mu_0 H \cos(\phi_f - \phi_1) - m_2 \mu_0 H \cos(\phi_f - \phi_2) + \\ &\frac{\mu_0}{4\pi} \frac{m_1 m_2}{(2R)^3} \left[\cos(\phi_1 - \phi_2) - 3\cos(\phi_1 - \phi_d)\cos(\phi_2 - \phi_d) \right], \end{aligned} \tag{1.9}$$

where ϕ_f, ϕ_1, ϕ_2, and ϕ_d are respectively the orientations of the field, the moment of particle 1, the moment of particle 2, and the vector between the two particles. A torque is induced when the moments of the particles are not aligned with the field and when the moments of both particles are not parallel to the major axis of the dimer (which is vector $\vec{d}$). The torque is given by *

$$\tau_{mag} = \frac{\partial U}{\partial(\phi_f - \phi_i)} + \frac{\partial U}{\partial(\phi_i - \phi_d)} \tag{1.10}$$

In order to solve this equation, two assumptions are made: the magnetic moment of both particles is equal ($m_1 = m_2 = m$) and the moments are aligned in the same direction ($\phi_1 = \phi_2 = \phi$). Equation 1.10 can now be rewritten to

$$\tau_{mag} = 2m\mu_0 H \sin(\phi_f - \phi) + \frac{\mu_0}{4\pi} \frac{m^2}{(2R)^3} 3 \sin\left(2[\phi - \phi_d]\right) \tag{1.11}$$

A rotating dimer also experiences a viscous torque due to the drag force of the fluid on the particles. The total torque on a dimer can be described as approximately two times the torque of a single particle that is rotating around its center of mass plus two times the torque that is induced by a translational movement of a particle in a circle with radius R. The drag force that a particle experiences by a translational motion through a medium is given by Stokes's law [20]

$$F_d = 6\pi\eta R v, \tag{1.12}$$

*The absolute value of the torque is given, so the sign and direction can be ignored.

where η is the viscosity of the medium and v is the velocity of the particle. The particle moves with a velocity that is equal to ωR, with ω the angular frequency in $\mathrm{rad\,s^{-1}}$. The torque is the cross product of the radius of the rotation with the drag force. In the case of a dimer that consists of two equally sized particles, this rotation radius is equal to the radius of the particles. This results in a torque due to the drag force of a translational motion that is given by

$$|\tau_{drag,trans}| = 6\pi\eta\omega R^3 \tag{1.13}$$

A single particle that is rotating experiences also a torque depending on the angular frequency ω, the viscosity and the radius. In the appendix A1, the derivation of the rotational torque is given, which has the result

$$|\tau_{drag,rot}| = 8\pi\eta\omega R^3, \tag{1.14}$$

The total viscous torque that is induced by a rotation is two times the sum of equation 1.13 and 1.14:

$$|\tau_{vis}| = 28\pi\eta\omega R^3 \tag{1.15}$$

For the calculation of the maximum rotation frequency, the relation $\tau_{mag} = \tau_{vis}$ should be solved for the maximum value of the magnetic torque. In order to solve this, the expression for the magnetic torque is simplified by assuming that the relaxation of the magnetic moment is much faster than the typical rotation. This assumption means that the magnetic moments are always aligned with the field, or in other words $\phi_f = \phi$. Now the maximum magnetic torque is induced when the dimer axis is at an angle of $45\,\mathrm{deg}$ with the magnetic field and thus $\sin(2[\phi - \phi_d]) = 1$. This results in a maximum rotation frequency, which is also called the critical frequency, of

$$\omega_{crit} = \frac{\mu_0 \chi^2 H^2}{168\eta} \tag{1.16}$$

A typical magnetic field strength that is used in this project is about $4\,\mathrm{mT}$. A particle with a susceptibility of 2 that is rotating in water has a maximum rotation frequency of about $48\,\mathrm{Hz}$.

1.5 DNA binding kinetics

Deoxyribonucleic acid (DNA) is a biological molecule that carries the genetic information of an organism. The basis of a DNA molecule is a nucleotide, which consists of a phosphate group, a deoxyribose, and a nucleobase. A phosphate group of a nucleotide can bind to the deoxyribose of another nucleotide, in this way, the so-called 'backbone' can be formed as shown in Fig. 1.4a. The information of the DNA is in the sequence of the four different nucleobases: Adenine (A), Thymine (T), Guanine (G), and Cytosine (C). The backbone with the nucleobases form a strand. Normally a DNA molecule contains two of such strands and is therefore called double stranded. The strands are bound to each other via hydrogen bonds between the nucleobases. Adenine can bind to thymine with two hydrogen bonds, guanine can bind to cytosine with three hydrogen bonds. The G-C binding is stronger due to the extra hydrogen bond [21].

In this work, a DNA strand is abbreviated as a sequence with the letters A, T, G, or C, starting with the 5-prime end and ending with the 3-prime end. In this way, the left strand of Fig. 1.4a is notated as 5'-ACTG-3', or just ACTG. The right strand (CAGT) matches completely with the left one and is thus complementary. The phosphate group is attached to the 5^{th} carbon atom of the deoxyribose-ring and is therefore called the 5'-end. Two complementary strands bind in such a way that the 5' to 3' directions of both strands are opposite, like in the figure: the left one is directed downwards and the right one upwards. If the direction is not opposite, the nucleobases are not aligned well and the hydrogen bonds cannot be formed.

Making a bond between two single stranded DNA molecules lowers the entropy (ΔS), which is unfavourable, but the loss in entropy can be overcome by an increase in enthalpy (ΔH). The total change in energy of a reaction is given by the Gibbs free energy $\Delta G = \Delta H - T\Delta S$, where T is the temperature in Kelvin. For

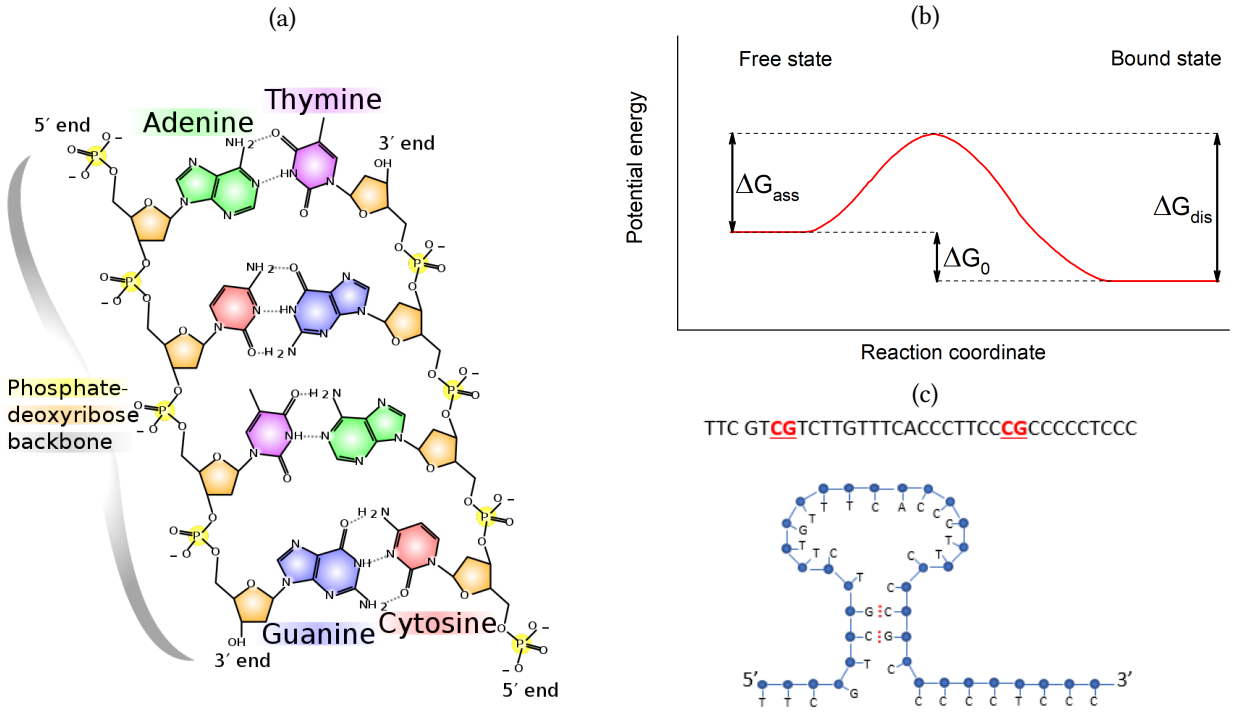

Fig. 1.4: **Structure and binding kinetics of DNA. (a)** Structure of a double stranded DNA molecule, showing the phosphate-deoxyribose backbone with the 5'end and the 3'end, and showing the four different bases: Adenine, Thymine, Guanine, and Cytosine[22]. **(b)** Energy diagram showing the energy barrier that has to be overcome to react. The barrier for the association is ΔG_{ass}, and for dissociation ΔG_{dis}. The energy difference between the bound and free state is the binding energy which is given by ΔG_0. **(c)** The sequence of a single stranded DNA molecule, of which the red underlined bases can bind to each other to form the shown hairpin structure.

two DNA molecules that are complementary, the binding energy depends on the number of basepairs and on the sequence of base pairs of both strands. For example the sequence 5'-CG-3' that binds to 3'-GC-'5, has a reaction energy $\Delta G = (-7.8 + 0.0297\ T)10^{-20}$ J, that is equal to $-2.2\,\mathrm{k_B T}$ at room temperature.

The reaction between two complementary single stranded DNA strands can be described by a general reaction energy diagram as shown in Fig. 1.4b. The bound state has the lowest energy and is therefore the preferential state. But to get in this bound state, the system has to overcome a free energy barrier. This barrier can be based on entropy (for example the molecules have to be in a certain position before the reaction can happen), or based on an increase in enthalpy (for example a high temperature is required). The barrier height is given by the Gibbs free energy, where the barrier for association (ΔG_{ass}) is lower than for the dissociation (ΔG_{dis}). The difference is equal to the binding energy ΔG_0.

The association and dissociation rate can be calculated with the following equation [23]

$$\kappa_{ass} = \kappa_t \nu \exp\left(\frac{-\Delta G_{ass}}{k_B T}\right), \qquad \kappa_{dis} = \kappa_t \nu \exp\left(\frac{-\Delta G_{dis}}{k_B T}\right) \tag{1.17}$$

in which $k_B T$ is the thermal energy, κ_t is the transmission coefficient and ν is the attempt frequency for the molecule to cross the barrier, this frequency is based on the molecule vibrations. The energy barrier for the dissociation is at least equal to the binding energy. The binding energy of two complementary DNA strands increases with the number of basepairs. Thus, the dissociation rate decreases exponentially with the number of base pairs. The typical binding time of a double stranded DNA molecule of 20 basepairs is usually longer than a year at room temperature *.

A single stranded DNA molecule is very flexible compared to a double stranded molecule, the persistence lengths are respectively 2 nm and 50 nm [25, 26]. Due to the flexibility of a single stranded DNA molecule,

*Based on dissociation rate $\kappa_{dis} = 1 \times 10^{-4}\,\mathrm{s}^{-1}$ at a temperature of 40 °C[24] and equation 1.17.

and the unbound nucleobases, a single stranded DNA molecule is able to bind to itself. This results in a so-called hairpin, of which an example is shown in Fig. 1.4c. In this project, the formation of hairpins is undesired and should be suppressed. Therefore, the DNA strands are designed to have weak hairpin bonds. The strength of these bonds is quantified with a melting temperature T_m. At this temperature, $50\,\%$ of the time the bonds are broken due to the thermal energy. A single stranded DNA molecule can switch between a hairpin state (H) and a free state (F), which can be represented by the reaction equation

$$F \underset{k_{dis}}{\overset{k_{ass}}{\rightleftharpoons}} H \tag{1.18}$$

The ratio between the concentration of F and H depends on the association and dissociation rates as follows

$$\frac{F}{H} = \frac{\kappa_{dis}}{\kappa_{ass}} = \exp\left(\frac{-\Delta G_0}{k_B T}\right) \tag{1.19}$$

At the melting temperature, the ratio between F and H is equal to unity. Using $\Delta G = (-7.8{+}0.0297\,T)10^{-20}$ J, which is the energy for the hairpin of Fig. 1.4c, and equalizing equation 1.19 to 1, gives a melting temperature of $4.8\,^{\circ}\mathrm{C}$.

A low hairpin melting temperature makes the hybridization of two complementary single stranded DNA molecules easier. The hybridization of single stranded DNA molecules is also called annealing of DNA. During the annealing process the reactions of equation 1.20 can happen. A free single stranded DNA molecule F can hybridize with its complementary stand to form a double stranded DNA molecule D, it can also form a hairpin H. The bond between the complementary DNA strands that are used in this project strands is strong, with a typical melting temperature of about $45\,^{\circ}\mathrm{C}$. The bond of the hairpin is much weaker, with a typical melting temperature of $5\,^{\circ}\mathrm{C}$. The annealing process starts at a high temperature ($90\,^{\circ}\mathrm{C}$) where the DNA molecules are most of the time in the free (unbound) state. Decreasing the temperature increases the probability to stay in a bound state. At a temperature in between the melting temperatures of the hairpin and the double stranded molecule, most of the double stranded DNA molecules survive, and most of the hairpins break up. When a hairpin breaks, it can form a hairpin again or it can bind to its complementary DNA strand. Once a double stranded DNA molecule is formed, it is unlikely that the molecule dissociates. Thus more and more stable doubled stranded DNA molecules are formed over time and the number of hairpins decreases. This leads to a high concentration double stranded DNA molecules at the end of the annealing process. This process is the most efficient with a large difference between the melting temperatures.

$$\begin{array}{ccccc} F & + & F & \underset{k_{ass,H}}{\overset{k_{dis,H}}{\rightleftharpoons}} & D \\ {\scriptstyle \kappa_{ass,H}}\downarrow\uparrow{\scriptstyle \kappa_{dis,H}} & & {\scriptstyle \kappa_{ass,H}}\downarrow\uparrow{\scriptstyle \kappa_{dis,H}} & & \\ H & & H & & \end{array} \tag{1.20}$$

1.6 Properties of PEG

Polyethylene glycol (PEG) is a polymer with the chemical structure H-(O-CH_2-CH_2)$_N$-OH, which consist of N repetitions of the monomer (O-CH_2-CH_2) that is shown in Fig. 1.5a. The number of repetitions determines the length and the molecular weight of the PEG molecule. The PEG molecule is usually coiled, but can be stretched or squeezed. Each monomer of a PEG molecule have many possible orientations with respect to the previous one. The radius of gyration for a PEG molecule can be estimated with the Flory radius [27], which is given by:

$$R_F = aN^{3/5} \tag{1.21}$$

in which a is the Khun length, which is $0.35\,\mathrm{nm}$, and N is the number of repetitions of the monomer.

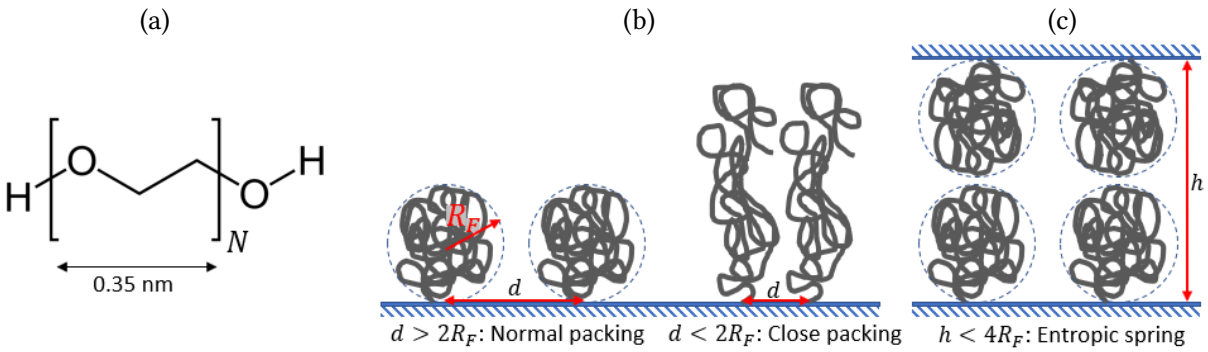

Fig. 1.5: **Shape of the PEG molecule: (a)** The chemical structure of a PEG monomer H-(O-CH_2-CH_2)$_N$-OH. **(b)** PEG molecules that are functionalized on a surface, when the distance between two PEG molecules is larger than $2R_F$ the PEG molecule can have their preferential size and shape. With closer packing, the PEG molecules are extended which is entropically unfavourable. **(c)** Two surfaces that are functionalized with PEG molecules repel each other when the distance between the surfaces become smaller than $4R_F$, due to the PEG molecules that act like an entropic spring.

Stretching the polymer to larger sizes than the Flory radius is unfavourable due to a decrease in entropy. Most micro-states are available for the polymer when it has a size in the order of the Flory radius, versus only one available state in the fully stretched case. In the same way, compressing the molecule is also unfavourable. The shape of a PEG molecule that is functionalized on a surface depends on the density of the PEG molecules, see Fig. 1.5. When the distance between the PEG molecules is larger than the Flory diameter, the PEG molecules will have a mushroom shape at a size of the Flory diameter. But with a higher density ($d < 2R_F$) the PEG molecules have less space and are forced to a stretched shape.

When a particle surface is densely coated ($d \sim 2R_F$) with PEG molecules, the PEG layer can act like an entropic spring, as shown in Fig. 1.5c. A functionalized surface repels other surfaces, when the surface to surface distance becomes smaller than 4 times the Flory radius. Also a functionalized surface is shielded by the PEG molecules to interact with other molecules. This property makes PEG a widely used polymer to prevent particle clustering[28].

Chapter 2

Materials and methods

This chapter describes details of the experimental procedures and chemical protocols. The reader can continue with chapter 3 and can inspect the procedure in this chapter if experimental details are needed.

2.1 Annealing of DNA

The DNA strands that are used in this project are obtained from IDT [29]. The exact sequence of the docking and analyte strands are given in chapter 5 in table 5.1. Complementary DNA strands are annealed in a TE buffer ($10\,\mathrm{mM}$ Tris, $1\,\mathrm{mM}$, pH 8.0). Strands (*A* and *B*) are diluted with TE buffer to a concentration of $100\,\mu\mathrm{M}$. Subsequently $6.25\,\mu\mathrm{L}$ of both solutions are mixed in a DNA-low-bind EPP (Eppendorf AG.). Next, $5\,\mu\mathrm{L}$ of the 5xTE-buffer (TE + $0.5\,\mathrm{mM}$ NaCl) and $7.5\,\mu\mathrm{L}$ of the 1xTE-buffer are added. The final solution contains both oligos *A* and *B* at a concentration of $25\,\mu\mathrm{M}$ and NaCl at a concentration of $0.1\,\mathrm{mM}$.

This solution is heated to $95\,^{\circ}\mathrm{C}$ with a thermal cycle machine (Bio-Rad, T100). At this temperature, all the hydrogen bonds between the nucleobases of the DNA strands are broken which means that all DNA will be in single stranded form. The temperature is decreased slowly to $4\,^{\circ}\mathrm{C}$, at a rate of $1\,^{\circ}\mathrm{C}$ every 35 seconds. In this way, the probability to form the intended stable double stranded DNA molecule is larger than any hairpin or misaligned configuration. When the annealing is done, the DNA strands are stored in a freezer at $-20\,^{\circ}\mathrm{C}$.

2.2 Gel electrophoresis

In order to determine if the annealing process is successful, a polyacrylamide gel electrophoresis (PAGE) experiment is performed. In this experiment, the DNA strands are pulled through a *4-20% Mini-PROTEAN® TBE* Gel (ThermoFisher) with electrostatic forces. This gel has a density gradient in the direction of the electric field. The DNA strands experience more and more drag the further they move. The end position of the DNA strands in the gel, after pulling for about two hours, gives information about the size of the DNA strands.

The gel is loaded in the electrophoresis device and filled with a TBE-buffer ($89\,\mathrm{mM}$ Tris, $89\,\mathrm{mM}$ Boric acid (H_3BO_3), $2\,\mathrm{mM}$ EDTA, pH 8.3). Nucleic Acid Sample Loading Buffer is purchased from Bio-Rad Laboratories to track the samples while running. The DNA samples are loaded into the gel, together with this loading buffer. Also the O'GeneRuler Ultra Low Range DNA Ladder (Thermo Fischer Scientific) is loaded into the gel. This ladder, which contains 11 different DNA fragments of 10 to 300 basepairs, is used as reference sample.

The samples with the DNA molecules are prepared as follows: The DNA strands are mixed with $1.0\,\mu L$ of the loading buffer and diluted with demiwater to get a sample volume of $5\,\mu L$ and a DNA concentration of 0.5, 1.0, or $1.5\,\mu M$. The loading buffer helps to settle the sample in the well and make it less diffusive. Also, the loading buffer contains a dye that makes is possible to track the DNA molecules during the PAGE experiment.

The loaded sample does not only contain the annealed DNA strands, but also the single stranded *docking strand A* and *B*. Comparing the end positions of the single stranded and doubled stranded DNA molecules in the gel, gives information about the efficiency of the annealing process. The single stranded molecules are smaller and should move a larger distance. When the distances are similar, the annealing failed.

After loading the samples, the electrophoresis devices is closed with a cover and the electrodes are connected to a power supply. A potential between the two electrodes of $90\,V$ is applied for 1:45 hour, where the top electrode is negative. The negative charged DNA strands are pulled through the gel downwards, due to the electric field.

Afterwards, the gel in removed from the electrophoresis device and placed in a plastic lid that is filled with $50\,mL$ TBE-buffer. $5\,\mu L$ of SYBR ® Gold Nucleic Acid Gel Stain (10 000X Concentrate in DMSO [30]) is added to the gel. This stain solution contains fluorescent stains that can bind to the DNA. The fluorescent stains are used for the localization of the DNA molecules. The lid with the gel is shaked gently in the dark to prevent bleaching of the fluorescent stains. After an incubation time of 15 minutes, the gel is washed with water and placed on a glass plate that is on top of an ultraviolet lamp. The stains light up due to the ultraviolet light, and are imaged with a camera. The resulting picture is shown in Fig. S.1, in the supplementary information S1.

2.3 Particle functionalization

Silica-magnetic microparticles ($511\,nm$) with a streptavidin coating are bought from *Microparticles GmbH*. The concentration of the stock solution is $10\,mg\,mL^{-1}$ ($130\,pM$). The stock solution is first mixed with a vortex mixer for 10 seconds. The streptavidin coated particle and biotinylated DNA docking strands are incubated in PBS buffer, in a protein-low-bind epp (Eppendorf AG.). The particles and DNA strands are incubated for 2 hours in a Thermomixer at $1200\,RPM$ at room temperature ($20\,^{\circ}C$). The particle and DNA concentrations are respectively $6.5\,pM$ and $5 \times 10^5\,pM$. The DNA is added in a 5 times excess to get the maximum coverage. The high ionic strength ($150\,mM$) of PBS is required for an efficient functionalization, because both the particles and the DNA strands have a negative charge and thus repel each other. In PBS, this charge is screened by the ions in solution, the Debye length is $0.8\,nm$ [31].

After incubation of the DNA with the particle, the solution is magnetically washed. The magnetic particles are pulled to the edge of the epp and the PBS with the remaining DNA strands are removed by using a pipette. The remaining (unbound) DNA should be removed to prevent unintended reaction between analyte strands (that are added later) and docking strand that are not attached to microparticles. After the washing step, a PBS buffer is added that contains $10\,mg\,mL^{-1}$ BSA, and $1\,mg\,mL^{-1}$ casein from bovine milk (both from Sigma Life Science). The epp now contains DNA-functionalized particles, at a concentration of $2\,pM$, BSA and casein molecules, and PBS.

In order to break up clusters, that have formed non-specifically during the functionalization process, 5 ultrasonic pulses of 0.5 seconds are sent through the solution using a sonic finger (Hielscher) at $50\,\%$ intensity. Finally, the solution is mixed gently for 1 hour in a rotating fin.

For some experiments the particles are functionalized with DNA and PEG. For this functionalization less DNA is used: $3 \times 10^4\,pM$ instead of $5 \times 10^5\,pM$. The DNA is mixed with a particles solution of $6.5\,pM$ and incubated for 1 hour. After the incubation, an excess of biotinylated PEG molecules is added, $1\,\mu L$ of a $1\,mM$

PEG solution. The PEG is also incubated for 1 hour. After this incubation the functionalization continues according to the original functionalization protocol.

2.4 Measuring zeta-potential

The surface charge of the particles is quantified by the zeta-potential. The zeta-potential is measured with the zetasizer (Malvern Zetasizer, Nano ZS). For this measurement the particles are diluted in demi-water to a particle concentration of $0.1\,\mathrm{mg\,mL^{-1}}$, which is about $1.3\,\mathrm{pM}$. The diluted solution is loaded into a disposable folded capillary cell (*DTS1070, Malvern*), that is subsequently loaded into the Zetasizer. The zeta-potential is measured three times for each sample that is loaded into the Zetasizer. The average zeta-potential (and variance) of the particles in solution is determined by measuring three samples.

2.5 VSM measurement

The magnetic susceptibility of the particles is determined using a vibrating-sample magnetometer (VSM). The device that is used for this measurement is the VSM SQUID (MPMS-SVSM, Quantum Design). Samples of $50\,\mu\mathrm{L}$ are loaded into a non-magnetic plastic capsule. This capsule is attached to the vibrating rod of the VSM. The magnetic moment of the sample is measured at $-20\,^{\circ}\mathrm{C}$ for varying magnetic field strengths in the range of -6×10^5 to $6 \times 10^5\,\mathrm{A\,m^{-1}}$.

2.6 Biotin-atto supernatant assay

To quantify the DNA coverage on the particles, an indirect supernatant assay is performed. The fluorescent biotin-atto655 dye is used for this assay. First, the fluorescence intensity of the dye is calibrated by measuring the fluorescence of samples of different biotin-atto concentration in the range of 10 to 10 000 nM. The fluorescence is measured at an excitation wavelength of $646\,\mathrm{nm}$ and an emission wavelength of $679\,\mathrm{nm}$, with a resolution of $5\,\mathrm{nm}$ (Fluoroskan Ascent PF).

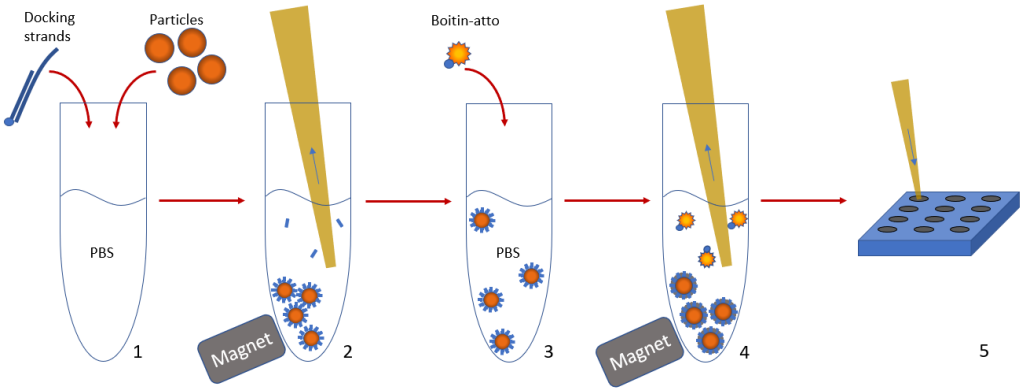

Fig. 2.1: **The indirect supernatant assay.** The five steps that are involved with the indirect supernatant assay are: **1)** Incubating the particles with DNA docking strands in PBS. **2)** Washing the particles out of the solution with a magnet and removing the DNA solution with a pipette. **3)** Adding a biotin-atto PBS solution and incubate. **4)** Washing the solution with a magnet and remove the supernatant with a pipette. **5:** Load the supernatant into the well plate of the Fluoroskan.

Next, the binding capacity of the streptavidin coated particles is determined. The biotin-atto655 is added at different concentrations to a constant amount of streptavidin coated particles. Tween is added ($1\,\mathrm{mg\,mL^{-1}}$) to this solution to make the b-atto molecules less reactive with the wellplate of the Fluoroskan, which suppresses fluctuations in the fluorescence signal. After incubating for 1 hour, the solution is washed magnetically. The supernatant contains no dyes as long as the concentration is far below the binding capacity. Once the biotin-atto concentration that is added to the particles approaches the binding capacity, the concentration in the supernatant increases. Subsequently the fluorescence intensity of the supernatant is measured. The binding capacity is determined by comparing the fluorescence of the calibration (F_{cal}) with the fluorescence of the supernatant (F_{meas}). This is done for different biotin-atto concentration ($[b]$) at the same particle concentration $[p]$, using equation 2.1.

$$A = \left(1 - \frac{F_{meas} - F_0}{F_{cal} - F_0}\right) \cdot \frac{[b]}{[p]}, \tag{2.1}$$

With a similar experiment, the amount of DNA on the surface of the functionalized particles can be determined, the steps of this experiment are depicted in Fig. 2.1. First the particles are functionalized with DNA as described above. Particles and DNA are incubated at concentrations of respectively $6.5\,\mathrm{pM}$ and $5 \times 10^5\,\mathrm{pM}$ in PBS. After two hours of incubation, the solution is washed magnetically and the remaining DNA and PBS are removed (step 2). Next, a biotin-atto concentration of $300\,\mathrm{nM}$ is added to the particles (step 3). Tween is added ($1\,\mathrm{mg\,mL^{-1}}$) to this solution. After incubation for 1 hour, the solution is washed again and the supernatant is removed and loaded into the well plate. The fluorescence intensity gives information about the DNA surface coverage of the particles: with low DNA surface coverage, most of the biotin atto can bind to the particles, so the biotin-atto concentration in the supernatant is low and thus the fluorescence intensity is low as well. In the same way, a high DNA surface capacity results in a high fluorescence intensity.

2.7 Sample preparation for OMCE

In order to measure the specific aggregation rates using the DNA model system, samples of different analyte concentrations are measured with the OMC experiment. The samples are prepared as shown in Fig. 2.2. The particles that are functionalized with docking strands are mixed with an analyte solution, resulting in a particle solution of $1.3\,\mathrm{pM}$. The analyte and particles are incubated for five minutes in a rotating fin. After the incubation the solution is loaded into the glass cuvette and placed in the setup.

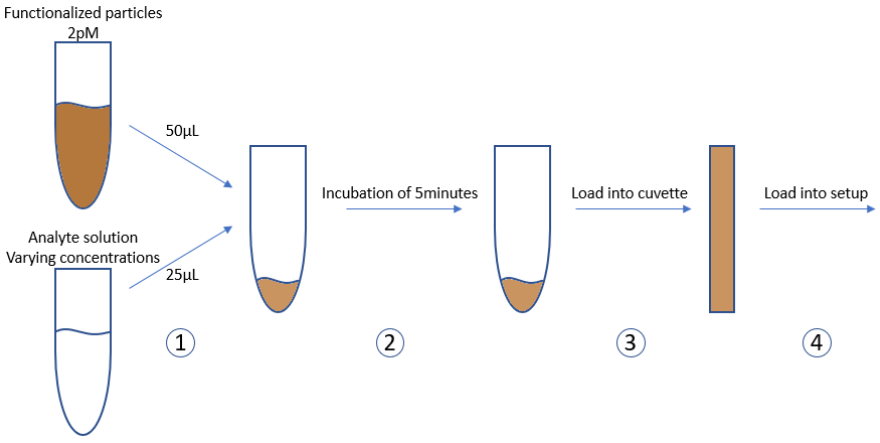

Fig. 2.2: Protocol of preparing a sample: **1)** Mix $50\,\mu\mathrm{L}$ of the functionalized particles with $25\,\mu\mathrm{L}$ of analyte solution. **2)** Incubate for 5 minutes. **3)** Load the obtained solution in the glass cuvette. **4)** place the cuvette in the OMC setup.

Chapter 3

The optomagnetic cluster experiment

In this project the magnetically induced aggregation rate κ_{agg}^{mag} will be measured with the optomagnetic cluster (OMC) experiment, which has been developed by Ranzoni et al. [9]. With this method, the dimer concentration of microparticles can be quantified, based on light scattering. The κ_{agg}^{mag} (from Fig. 1.2) can be quantified using a four-step actuation protocol. This chapter describes the experimental setup, the measurement principle, and the four-step actuation protocol with which the aggregation rate can be determined.

3.1 Experimental setup

The experimental setup of the OMC experiment is schematically shown in Fig. 3.1. The light source ① is a red light ($\lambda = 660\,\mathrm{nm}$) laser (from Thor labs) with a power of $150\,\mathrm{mW}$. Two cylindrical lenses ② are used to change the laser spot from elliptical to circular. Note that this is not the polarization but only the shape of the spot, the polarization of the light is S-like (perpendicular to the plane of rotation of the magnetic dimers). The circular shape of the spot is required to focus all the light with a convex lens to a pinhole ④ with a diameter of $20\,\mu\mathrm{m}$. The pinhole is used to create a point source, which is needed to focus the laser light to an as small as possible focus volume inside the sample. Once it has passed the pinhole, the diverging light is collimated with a convex lens ③. A mirror ⑤ reflects the light over an angle of $90°$ in the direction of the sample. Some unintended light reflections are blocked with a diaphragm ⑥ with a diameter of $5\,\mathrm{mm}$. The resulting light beam has a power of $100\,\mathrm{mW}$. A convex lens focuses the light in a cuvette that contains the particle solution. The cuvette is made of borosilicate glass (Hilgenberg) with inner size dimensions of $(1 \times 1 \times 20)\,\mathrm{mm}^3$. A rotating magnetic field is realized at the position of the cuvette ⑧ using four electromagnets ⑦. The dimers that are present in the cuvette follow the rotation of the magnetic field and scatter the light in all directions. In this project, the scattered light is detected at a scatter angle of $90°$. A convex lens is used to focus the scattered light into the photodetector ⑨.

3.2 Measuring dimer concentrations

The OMC experiment is based on light scattering at superparamagnetic microparticles. In an external magnetic field, these particles become magnetized and interact with each other and with the field. Two particles that have encountered and formed a magnetic dimer will follow the rotation of a rotating magnetic field. The light scattering at the rotating dimers is used to determine the number of dimers in solution. The method for this measurement is explained in this section.

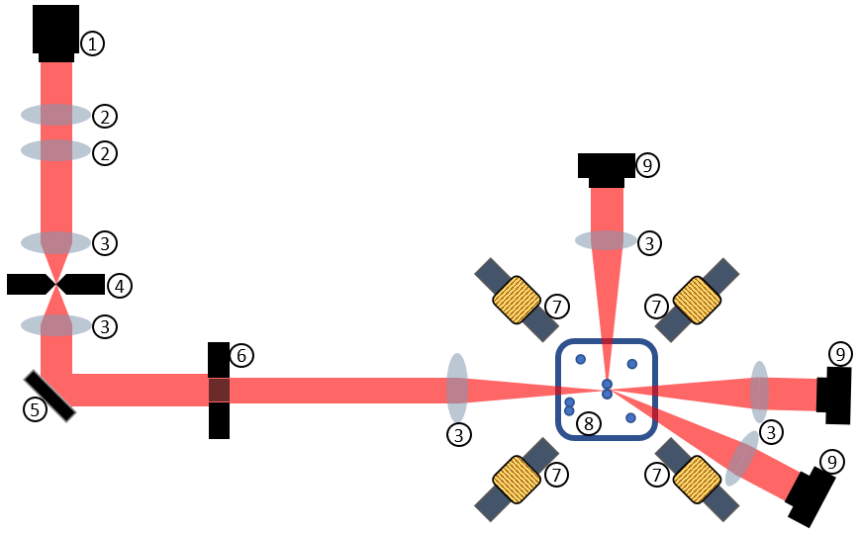

Fig. 3.1: **Setup of the OMC experiment.** A topview of the setup that is used in the OMC experiments. The main components are:

1. Laser, red light ($\lambda = 660\,\mathrm{nm}$)
2. Cylindrical lenses
3. Convex lenses
4. Pinhole ($d = 20\,\mu\mathrm{m}$)
5. Mirror
6. Diaphragm ($d = 5\,\mathrm{mm}$)
7. Electromagnets
8. Cuvette filled with particles
9. Photodetectors

3.2.1 Scattering signal

The rotating dimers in the solution are illuminated with a laser and scatter light in all directions. The photodetector measures the intensity of the scattered light at 90°. The intensity of the scattered light depends on the orientation of the dimers and fluctuates over time while the dimers are rotating, see Fig. 3.2a.

When the magnetic field is off, all the dimers have a random orientation, due to the Brownian motion and rotation. The signal of the scattering is then noisy due to particles and clusters that move in and outside the focus volume of the laser. When the (rotating) magnetic field is turned on, the particles and the dimers align with the magnetic field and start rotating. A particle rotates because it has a magnetic anisotropy axis, which aligns with the magnetic field. A dimer rotates due to its magnetic shape anisotropy, as explained in section 1.4. The intensity of the light scattering at a rotating particle does not oscillate in time, due to its spherical symmetry. So only the scattering at clusters contributes to the oscillation of the scattered light. The contribution of each dimer is assumed to be equal, because all dimers rotate in sync, parallel to the field. Thus, the magnitude of the oscillation increases linearly with the number of dimers that are present in the focus volume of the laser.

Fig. 3.2a shows the signal that is measured with the photo detector at a scattering angle of 90°, around the time when the magnetic field is turned on for 0.6 seconds. Initially the field is off, so the photo detector measures only random scatter events, resulting in a noisy baseline. After switching the field on, a clear oscillating signal appears, resulting from scattering at the rotating dimers. The rotating frequency of the magnetic field is 5 Hz, which corresponds to a period of 0.2 seconds. The oscillating signal repeats after each half period. When the magnetic field is turned off, the dimers are not forced to be aligned anymore. The dimers will become randomly oriented and the oscillation relaxes to the original noisy baseline.

3.2.2 Quantifying dimer concentration with Fourier amplitude

In order to get the amplitude of the oscillating signal, and thus to get a quantification for the dimer concentration, the Fourier transformation is taken from the scattering signal. Fig. 3.2b shows the Fourier transformation of Fig. 3.2a, of the period when the magnetic field is turned on. The x-axis of this graph shows the frequency

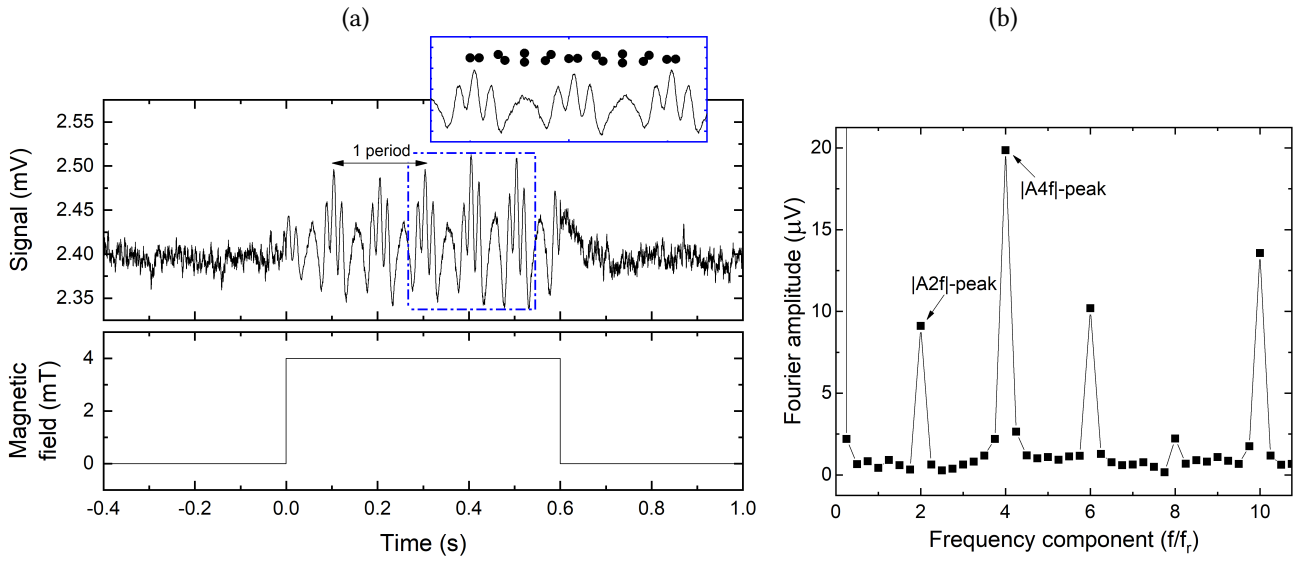

Fig. 3.2: **Example of a result from OMC experiments. (a)** A scattering signal and the magnetic field strength plotted against the time. The magnetic field is switched on for 0.6 seconds. When the field is switched on the scattering signal changes from noise to a clear oscillating signal. The magnetic field rotates with a frequency of 5 Hz, so 1 period correspond to 0.2 seconds, which is indicated by the arrow. When the magnetic field is turned of, the scattering signal relaxes back to the original noisy signal. The insert shows a zoom of the signal that is marked with the blue square. Above the signal the possible dimer orientation is depicted, which changes in time. One period corresponds to a full rotation of a dimer. The signal is repeated after half a rotation due to the symmetry of a dimer, so the scattering signal oscillates at two times the rotation frequency. **(b)** The Fourier transformation of the signal from figure **(a)**. The absolute Fourier amplitude is plotted as a function of the frequency component relative to the rotation frequency $f_r = 5\,\mathrm{Hz}$. The |A2f| peak and the |A4f| peak corresponds to an oscillation of 10 Hz and 20 Hz respectively. The Fourier spectrum only has peaks at the even frequencies, because the scattering signal oscillates at two times the rotation frequency.

components of the signal normalized on the rotation frequency of the field ($f_r = 5\,\mathrm{Hz}$). Due to the symmetry of the rotating dimers, the signal has only frequency components that are multiplications of 2 times the rotation frequency ($2f_r$, $4f_r$, $6f_r$...). Therefore the Fourier amplitude has only peaks at the even numbers. The height of these peaks corresponds to the main amplitude of the oscillating signal. In this project, the|A2f| and the|A4f| peak from the Fourier spectrum are used for the quantification of the dimer concentration.

Quantifying the dimer concentration with an OMC experiment is only accurate when the height of the |A2f|- or |A4f|-peak is linearly proportional to the number of dimers in solution. The relation between the height of the peak and the amount of dimers is tested by measuring the scattering signal at different dimer concentrations.

For this measurement, samples with different dimer concentrations are prepared by diluting the stock solution of magnetic particles. It is estimated that about $10\,\%$ of the particles in the stock solution is part of a dimer. By diluting the stock solution, the particle and also the dimer concentration is decreased. The scattering signal of these diluted samples is measured with the setup of the OMC experiments at a scatter angle of $90°$ using a rotating magnetic field of $4\,\mathrm{mT}$ at $5\,\mathrm{Hz}$.

Fig. 3.3 shows the height of the Fourier amplitude (|A4f|) against the particle concentration, the data is fitted linearly. Under the assumption that the dimer concentration is linear proportional to the particle concentration, it can be concluded that the |A4f| is linear with the dimer concentration.

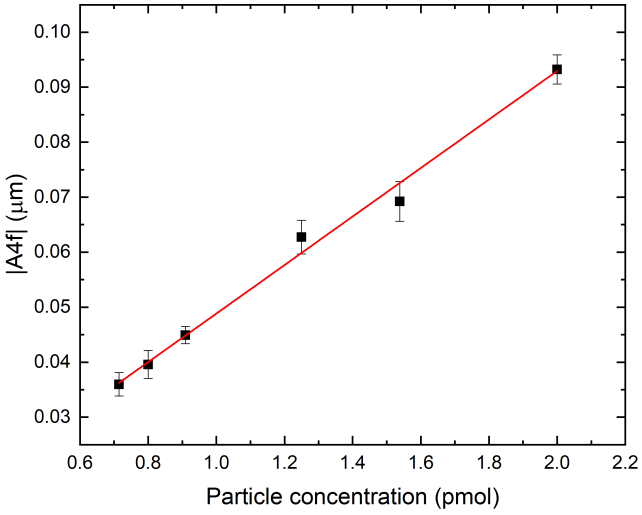

Fig. 3.3: **Calibration of the scattering signal of dimers.** The Fourier amplitude (|A4f|) of the scattering signal is plotted as a function of the particle concentration. A linear relation is fitted through the data points.

3.3 Measuring the chemical aggregation rate

Measuring the magnetically induced chemical aggregation rate κ_{agg}^{mag} involves a four-step-measurement protocol that has previously been developed by Romijn et al. [10]. These steps are depicted in Fig. 3.4 and explained below in detail.

First the initial amount of dimers should be measured, this is done in the first *Measurement phase*. In this phase 5 or 10 short magnetic pulses are applied for 0.4 seconds, a magnetic field strength of $4\,\mathrm{mT}$ is used. It is important that no new dimers (or larger clusters) are made during the measurement phase. Therefore the pulse should be short and the magnetic field strength low. To prevent cluster formation, the field is turned off for 10 seconds between two consecutive measurement pulses. In this time, the particles randomly redistribute in the solution, due to diffusion. During a pulse, the dimers rotate two rounds, resulting in a scattering signal that is similar to the signal from Fig. 3.2a. In the first part of the pulse ($t < 0.1\,\mathrm{s}$), the amplitude of the signal is smaller than the amplitude during the rest of the pulse. Not all dimers are immediately aligned with the field when the field is turned on, so not all dimers contribute to the oscillation of the signal. It is assumed that all dimers are aligned after one full rotation of the field. Therefore only the second rotation is used to quantify the dimer concentration. The signal of the last 0.2 seconds of the measurement phase is analysed with the Fourier transformation, of which the|A4f| peak is used for the quantification for the dimer concentration. Each pulse of the measurement phase results in one |A4f| value. The initial dimer concentration is quantified by the average of the |A4f|-values of the first 5 or 10 pules.

During the second phase of the measurement, the *Actuation phase*, the magnetic field is turned on for a longer time (typically 20 seconds). While the field is on, the particles encounter each other and magnetic dimers are formed. Note that also during the actuation phase the magnetic field is rotating to monitor the increase in number of dimers in the solution. Two particles that have formed a magnetic dimer will start following the rotation of the magnetic field and the scattering at this new dimer is added to the total scattering signal. So the increase in dimer concentration can be measured as a function of time. The|A4f| peak increases in time during the actuation phase as shown in Fig. 3.4. The total number of dimers that are formed during the actuation phases is ΔN_{mag}. Particles that have formed a cluster during the actuation phase stay together until the end of the actuation phase. Therefore the two particles in each dimer have an unique interaction time. Dimers that are formed at the beginning of the actuation phase have a longer interaction time than dimers that are formed at the end of the actuation phase. The particles of a magnetic dimer can form a chemical bond, when this happens the magnetic dimer becomes a chemical dimer.

After the actuation phase, the field is turned off for 80 seconds, to let the particles that have not formed a chemical bond redisperse in the solution. This is called the *diffusion phase*. The magnetic dimers that have become chemical dimers during the actuation phase stay intact. At least if the chemical bond is strong

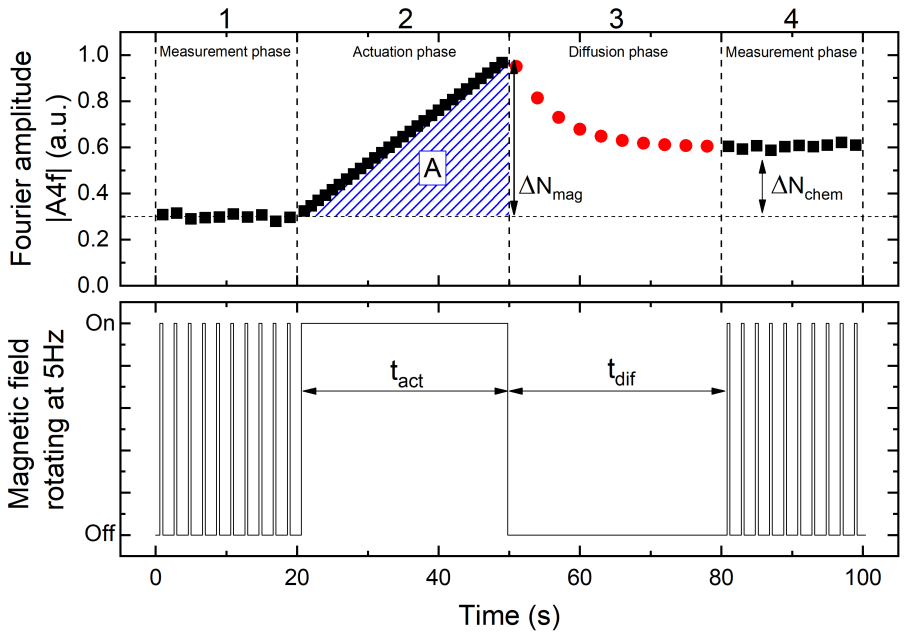

Fig. 3.4: **The 4 phases of a measurement in an OMC experiment.** The |A4f| peak of the scattering signal and the normalized magnetic field are plotted against the time. The first step is the measurement phase: short pulses are applied to measure the initial amount of dimers, the pulses are short to prevent cluster formation. The second step is the actuation phase, where the magnetic field is set on for a long time ($\sim$30 s). During the actuation, new magnetic dimers are formed, which causes the increase in the |A4f|. The third phase is the diffusion phase. The magnetic field is turned off for a while. The particles that have not formed a chemical bond diffuse and become dispersed randomly in the solution. The last phase is again a measurement phase to measure the final amount of (chemical) dimers.

enough, i.e. the typical dissociation time t_{dis} should be longer than the diffusion time t_{dif}. Note that during the diffusion phase the number of dimers cannot be measured, because the field is off so the dimers are not rotating.

Finally, the resulting amount of chemical dimers is measured during the second measurement phase. The same actuation protocol as in the first measurement phase is used. The difference in signal of both measurement phases (ΔN_{chem} of Fig. 3.4) corresponds to the number of chemical dimers that are made during the actuation phase.

The ratio between the number of chemical dimers ΔN_{chem} and the number of magnetic dimers ΔN_{mag} yields the fraction of chemical dimers that have formed during the actuation. To quantify the magnetically induced aggregation rate κ_{agg}^{mag}, this fraction is divided by the average interaction time $\langle t_{int} \rangle$ of a dimer.

$$\kappa_{agg}^{mag} = \frac{\Delta N_{chem}/\Delta N_{mag}}{\langle t_{int} \rangle} \tag{3.1}$$

Here the average interaction time is defined as

$$\langle t_{int} \rangle = \frac{1}{\Delta N_{mag}} \sum_{i=1}^{\Delta N_{mag}} t_{int,i}, \tag{3.2}$$

in which $t_{int,i}$ is the interaction time of dimer i. The sum of the interaction times of all dimers is equal to the marked area A in Fig. 3.4. In case of a linear dimer formation rate, the area A is equal to $\Delta N_{mag}\ t_{act}/2$. Now the aggregation rate can be written as

$$\kappa_{agg}^{mag} = \frac{\Delta N_{chem}}{A} = \frac{\Delta N_{chem}}{\Delta N_{mag}} \frac{1}{t_{act}/2}. \tag{3.3}$$

The maximum value of κ_{agg}^{mag} that can be measured with an OMC experiment depends on the actuation time. When the particle aggregation is such high that all magnetic dimers become chemical dimers, the ratio in equation 3.3 becomes one. In this case, the maximum rate that can be measured with an actuation time of 20 seconds is $\kappa_{agg}^{mag} = 0.1\,\mathrm{s}^{-1}$. The lowest rate that can be measured, due to the noise in the signal, is $\kappa_{agg}^{mag} = 0.005\,\mathrm{s}^{-1}$. This gives a dynamic range for measuring the rate of approximately a factor 20.

3.4 Ideal particles

In the actuation phase of Fig. 3.4, the Fourier amplitude increases linearly in time, which is interpreted as a linear increase of the number of dimers in the solution. This is based on several assumptions. For example, the scattering cross-section at every single dimer is equal, the dimer formation rate is constant, and only dimers contribute to the scattering signal.

The light scattering at a dimer depends on the size and the effective refractive index of the particles. For an equal scattering cross-section of dimers, all dimers should contain particles of the same size and effective refractive index. Clusters made of three particles (triplets) have a different scattering cross-section, compared to dimers. So ideally, the formation of triplets (or larger clusters) should be prevented during the actuation phase, this can be realized by using only short actuation phases ($\sim$ 20s)[16]. The last assumption, that is related to scattering, is that all the dimers in the solution have the same orientation. This can be realized when every dimer has the same magnetic and viscous torque. So the size and magnetic properties of each dimer should be the same and the magnetic field strength should be homogeneous. In summary, all particles in the solution should be monodisperse.

Not only the scattering at each dimer should be the same to get a linear increase of the Fourier amplitude with concentration, but also the dimer formation rate should be constant. The number of dimers that are formed per unit of time depends on the monomer concentration $[m]$ and the magnetically induced encounter rate κ_{enc}^{mag}, as described by equation 3.4. This equation only holds in the limit that the dimer concentration is low, ($[N_{mag}] \ll [m]$), where the formation rate of a triplet is negligible.

$$\frac{\partial[N_{mag}]}{\partial t} = \kappa_{enc}^{mag}[m]^2, \tag{3.4}$$

Note that there is no loss term in the equation, because magnetic dimers will not break up and it is assumed that no triplets are formed. The monomer concentration is decreasing in time and depends on the number of dimers as follows

$$[m] = [m_0] - 2[N_{mag}], \tag{3.5}$$

where $[m_0]$ is the initial monomer concentration.

Filling in equation 3.5 in equation 3.4 and solving the obtained differential equation results in

$$[N_{mag}] = \frac{\kappa_{enc}^{mag}[m_0]^2 t}{1 + 2\kappa_{enc}^{mag}[m_0]t}. \tag{3.6}$$

The number of magnetic dimers according to equation 3.6 is plotted versus time t in Fig. 3.5a with $m_0 = 1\,\mathrm{pM}$ and $\kappa_{enc}^{mag} = 6 \times 10^{-9}\,\mathrm{M}^{-1}\,\mathrm{s}^{-1}$. At low values for t (t <20 s) the number of dimers increases approximately linearly in time, the error with a linear increase is less than $10\,\%$ below the 20 seconds. At higher values the dimer formation rate decreases, due to depletion of the monomers. Fig. 3.5b shows the results of a real measurement of magnetic particles. The|A4f| peak is plotted against the actuation time. This curve shows the same depletion effect as predicted in Fig. 3.5a. In order to stay in the linear regime of the actuation (the marked area in the graphs), the actuation phase is limited to 20 seconds.

In summary, the OMCE is most accurate when the actuation phase is shorter than the typical time at which depletion occurs, and a linear signal can be realized when the particles are monodisperse in size, in refract-

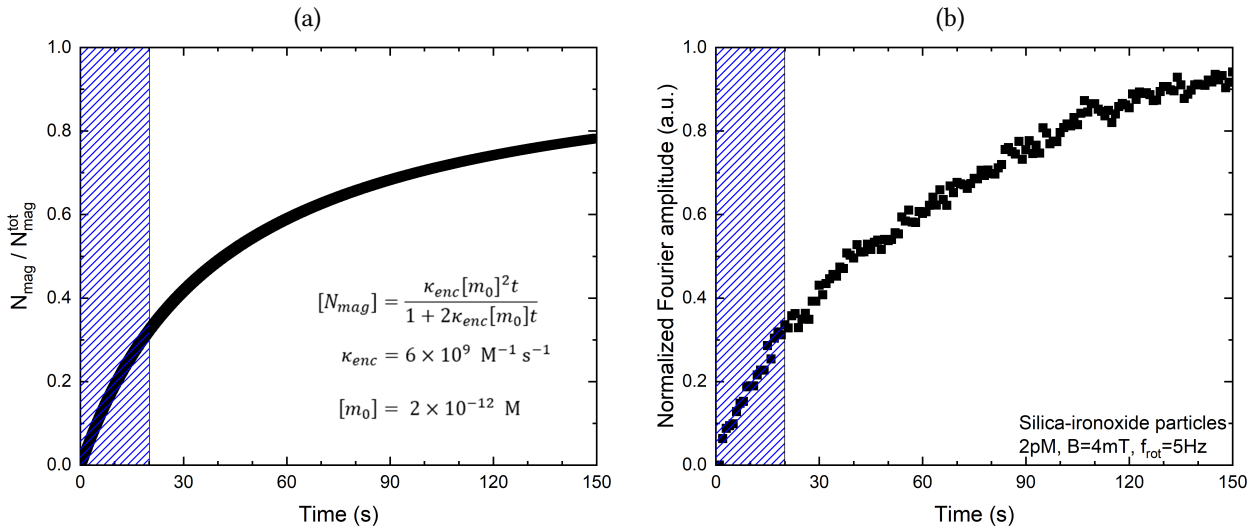

Fig. 3.5: **The depletion effect. (a)** Depletion effect as described by equation 3.15, with $\kappa_{enc} = 6 \times 10^9\,\mathrm{s}^{-1}$ and $p_0 = 2 \times 10^{-12}\,\mathrm{M}$. **(b)** Measured depletion effect of magnetic particles at an initial particle concentration of $2 \times 10^{-12}\,\mathrm{M}$, a magnetic field strength of $4\,\mathrm{mT}$ and a rotation frequency of $5\,\mathrm{Hz}$. The marked area is the linear regime of the actuation. The actuation should not be too long to stay in this regime.

ive index, and in magnetic properties. In the next chapter the most ideal particle is selected for the OMC experiments of this project.

Chapter 4

Particle selection for the OMC experiment

In this chapter, particles that can meet the requirements for OMC experiments are selected. In previous work from Ranzoni et al.[32], and Romijn et al.[10] the Ademtech Masterbeads were used. A disadvantage of the Ademtech particles is their large size dispersion (CV $= 25\,\%$). Two alternatives for the Ademtech particles are the polystyrene superparamagnetic microparticles and the silica superparamagnetic microparticles, from the manufacturer *MicroParticles GmbH*. The manufacturer of these particles claims a smaller size distribution (CV $< 5\,\%$). However, apart from the size dispersion also the magnetic and chemical properties determine how suited the particles are for the OMC experiment. In this chapter the Ademtech Masterbeads, the silica particle from microparticles GmbH, and the polystyrene particles from microparticle GmbH are shortly called the Ademtech, Silica, and Polystyrene particles respectively. At the end of this chapter, the most suited particle type, for use in the OMC experiment, is selected.

4.1 Non-magnetic properties

The three different particle types considered here have a mean diameter of about $500\,\mathrm{nm}$. A SEM image of the three different particle types is shown in Fig. 4.1. Also the diameter, the density, and the zeta potential of the particles are given in this figure. The three particle types are composed of iron-oxide (a mixture of magnetite: Fe_3O_4, and hematite: Fe_2O_3) grains that are randomly dispersed in a non-magnetic matrix. The

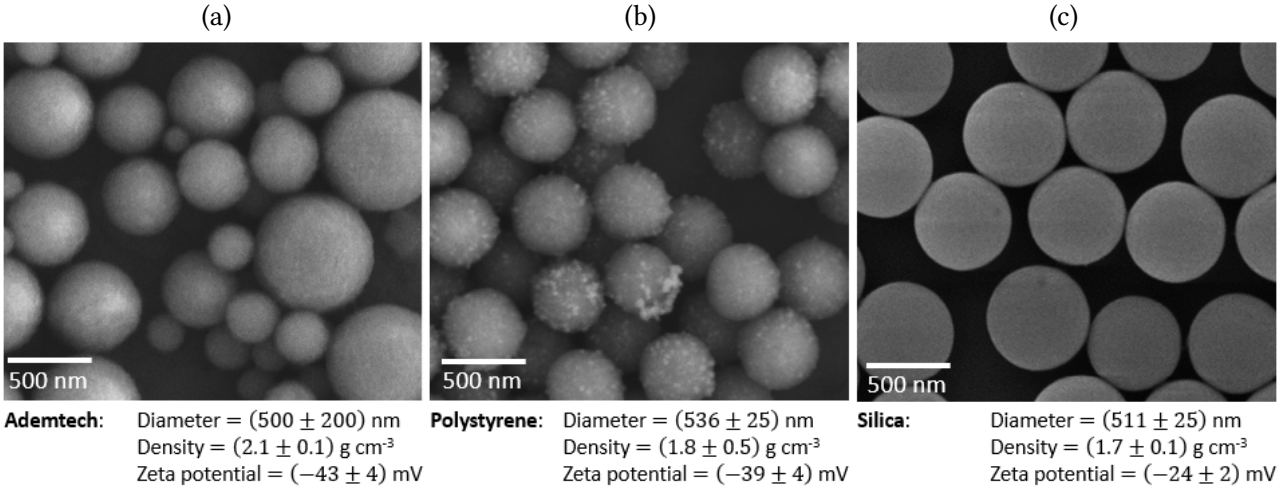

Fig. 4.1: **SEM images** of Ademtech particles **(a)**, polystyrene particles **(b)** and silica particles **(c)**. The white bar corresponds to $500\,\mathrm{nm}$ and the scale is the same on all three images.

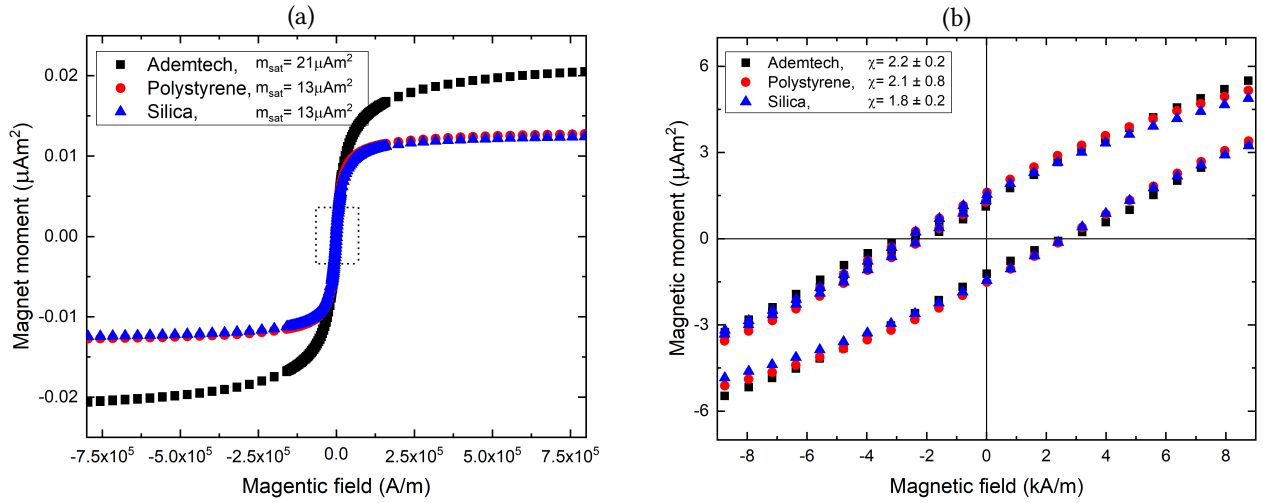

Fig. 4.2: **Results of the VSM measurement (a)** The magnetic moment versus the magnetic field, for the three different particles. The saturation magnetic moment (m_{sat}) of the three samples is given in the legend. **(b)** A zoom in at the place of the marked square in **(a)** around zero field. The magnetic volume susceptibility χ is determined by fitting a linear line through the data points from -3 to $3\,\mathrm{kA\,m^{-1}}$. The susceptibility of the three particles is given in the legend.

Ademtech- and Polystyrene-particles have a non-magnetic matrix of polystyrene. The Silica particles have of a matrix made of silica. The large size dispersion of the Ademtech beads is clearly visible in Fig. 4.1a. In the SEM image, the silica particles appear smoother than the other particles. Especially the polystyrene particle have a very rough surface. The three particle types have comparable mass densities of about $2\,\mathrm{g\,cm^{-3}}$. The surface charge of the three different particles is measured with the Zetasizer. All three types have a negative zeta potential in the order of tens of millivolts. The relative number of dimers per particle in the stock solution is estimated to be 1/13, 1/17, and 1/9 for respectively the Ademtech, polystyrene and silica particles. The high number of dimers in the silica stock solution might be related to the relative low absolute surface charge. A high surface charge prevents clusters formation due to electrostatic repulsion.

4.2 Magnetic properties

The magnetic volume susceptibility of the particles is determined with a vibrating-sample magnetometer (VSM), which measures the magnetic moment of a sample as a function of the magnetic field. For this measurement, samples of $50\,\mu\mathrm{L}$ of $10\,\mathrm{mg\,mL^{-1}}$ particles in an aqueous solutions are measured at a temperature of $-20\,^{\circ}\mathrm{C}$. At this temperature, the samples are frozen, so the particles cannot rotate and translate. During the measurement, the field is swept from $-8.0 \times 10^5\,\mathrm{A\,m^{-1}}$ to $8.0 \times 10^5\,\mathrm{A\,m^{-1}}$ and back again. The magnetic response of the samples of the three different particles is shown in Fig. 4.2a, also the saturation values for the magnetic moment (m_{sat}) is given in this figure. A zoom, around zero, is shown in Fig. 4.2b.

At low magnetic fields, the magnetic moment of an ideal superparamagnetic sample increases linearly according to equation 1.7. The graph in Fig. 4.2b shows a small remanence (a moment at zero field), which indicates that the particles are not perfectly superparamagnetic. In order to determine the volume susceptibility of the micro particles, a linear function ($y = ax + b$) is fitted through the data points around zero field (from -3 to $3\,\mathrm{kA\,m^{-1}}$). The slope a is divided by the total volume of the particles in the sample. The samples contain $0.5\,\mathrm{mg}$ particles. This weight divided by the mass density gives the total volume of the particles. The ratio of the slope a and the total volume gives the volume susceptibility. The values for the volume susceptibility of the three particle types are given in Fig. 4.2b. There is no significant difference between the volume susceptibilities of the three particles, all have a value around 2 , the error bars overlap. The large error bar of the susceptibility of the polystyrene particles is caused by the relative large uncertainty in the mass density that is given by the supplier.

The averaged magnetic content per particle can also be determined from the data from the VSM-measurement. The saturation value of the magnetic moment gives information about the amount of magnetic material in a sample. Iron-oxide has a mass saturation magnetization of $76\,\mathrm{A\,m^2\,kg^{-1}}$ for bulk material[33] and 61-$74\,\mathrm{A\,m^2\,kg^{-1}}$ for nanoparticles [34]. For the calculation of the amount of iron-oxide in a particle, a mass saturation magnetization of iron-oxide is assumed to be $(68 \pm 8)\,\mathrm{A\,m^2\,kg^{-1}}$. Dividing the measured saturation value for the magnetic moments (m_{sat}) of the three samples by the mass saturation magnetization of iron-oxide give the total amount of iron oxide in a sample. The Ademtech sample ($m_{sat} = (21.4 \pm 0.1)\,\mu\mathrm{A\,m^2}$) has in total $(0.31 \pm 0.04)\,\mathrm{mg}$ iron-oxide. The polystyrene and silica samples ($m_{sat} = (12.8 \pm 0.2)\,\mu\mathrm{A\,m^2}$) has both $(0.18 \pm 0.02)\,\mathrm{mg}$ iron-oxide. This values corresponds to an iron-oxide weight percentage of $(62 \pm 8)\,\%$ for the Ademtech particle, the manufacturer claims at least $70\,\%$. The polystyrene and silica particles contain $(36 \pm 4)\,\%$ iron-oxide, where the manufacturer claims at least $30\,\%$. These weight fractions are used later to estimate the effective refractive index of the particles, which will be used in scattering simulations.

The VSM measurement gives information about the average magnetic properties of the particles. From these measurements, it can be concluded that the average Ademtech, Polystyrene or Silica particles have similar magnetic volume susceptibilities, at low magnetic field strengths. The average magnetic moment at a typical magnetic field in experiments ($B = 4\,\mathrm{mT}$) is the same for the three particle types. But the VSM measurement does not give information about the particle to particle variation in a solution. It might be possible that some particles contain more magnetic material than others, which would results in variations in magnetic moments of individual particles. The consequence of is that both the magnetic encounter kinetics and the rotation kinetics may vary from dimer to dimer. In order to get information about the magnetic moment dispersion of the particles, the critical frequency of the three particle types is measured. This is discussed in the next section.

4.2.1 Critical frequency

The dimers in a solution of ideal spherical particles of $500\,\mathrm{nm}$ and a volume susceptibility of 2 has a well defined critical frequency, which is $48\,\mathrm{Hz}$ at a magnetic field of $4.0\,\mathrm{mT}$ according to equation 1.16. Deviating from this ideal case, for example due to size dispersion or a dispersion in the volume susceptibility, leads to variations in the critical frequency. Measuring the critical frequency of a particle solution, gives information about the dispersion of the particles, which will be explained later in this section.

In order to determine the critical frequency, the amplitude of the oscillating scattering signal is measured as a function of the field rotation frequency. For this measurement, 10 measurement pulses are performed at each field rotation frequency. During the measurement no new dimers are formed, only the dimers that are initially present are responsible for the signal. When the rotation frequency is increased, the viscous drag increases whereby less and less dimers are able to follow the rotation. This results in a decreasing amplitude of the oscillating scattering signal. The Fourier amplitude (|A2f| for Ademtech and polystyrene, |A4f| for silica) of the scattering signal is plotted against the filed rotation frequency in Fig. 4.3. The data points are scaled to the Fourier amplitude at $5\,\mathrm{Hz}$. The graph also shows the calculated critical frequency of monodisperse (ideal) particles. In case of monodisperse particles, all the dimers can follow the rotation of the magnetic field at frequencies up to the critical frequency. So the Fourier amplitude is constant at these frequencies.

For the Silica particles, the normalized Fourier amplitude starts decreasing at a higher frequency and shows a faster decrease than the other two particle types. The |A4f| does not decrease (significantly) below 1 up to a rotation frequency of about $20\,\mathrm{Hz}$, while the |A2f| of the Ademtech and Polystyrene particles decreases immediately, when the rotation frequency is increased. At $20\,\mathrm{Hz}$, only $\sim 50\,\%$ of the polystyrene dimers are able to follow the rotating field, compared to $\sim 100\,\%$ of the silica dimers. The critical frequency of the three particles is approximated by the frequency at the intersection of the horizontal line and the slanting line that is fitted through to the decreasing signal, as shown in Fig. 4.3 similar as in the work of Ranzoni et al.[9]. Using this approximation, the critical frequency of respectively the Ademtech, polystyrene, and silica particles is $(12 \pm 1)\,\mathrm{Hz}$, $(9 \pm 1)\,\mathrm{Hz}$, and $(31 \pm 3)\,\mathrm{Hz}$.

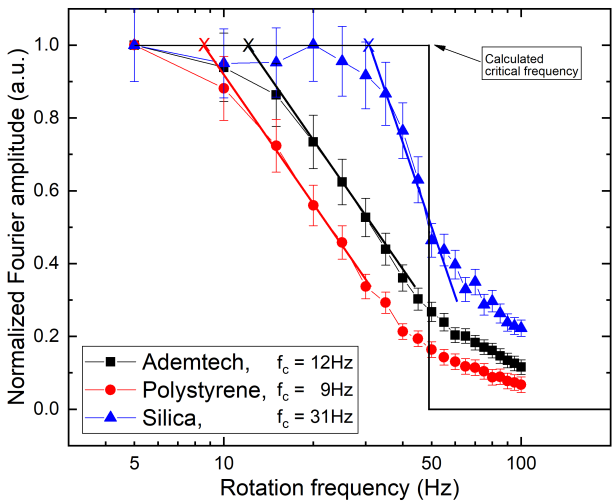

Fig. 4.3: **The critical frequency.** The Fourier amplitude of the scattering signal as a function of the rotation frequency of the magnetic field, for the three different particle types. The Fourier amplitude is normalized on the amplitude at 5 Hz. The critical frequency f_c is approximated by the intersection of the horizontal line and the slanting line obtained fitted the data points where the slope is the steepest. The same approximation is used as in the work of Ranzoni et al.[9]. The calculated critical frequency of a solution with monodisperse dimers is 48 Hz, with $\chi = 2$ and $B = 4\,\mathrm{mT}$, according to equation 1.16. The critical frequencies of the Ademtech, Polystyrene, and Silica particles are respectively (12 ± 1) Hz, (9 ± 1) Hz, and (31 ± 3) Hz.

The average volume susceptibility and size of the three different particle types are similar. So the differences in Fig. 4.3 might be caused by differences between individual particles in the solution. These difference are caused by, for example, size dispersion or a dispersion in magnetic content per particle. The effect of these two dispersions on the critical frequency is discussed below.

The critical frequency of a single dimer is calculated by equalizing the (maximum*) magnetic torque and the viscous torque. The magnetic torque of a dimer depends on the product of the magnetic moments (m_1 and m_2) and the radii (R_1 and R_2) of both particles and is given by

$$\tau_{mag} = \frac{3\mu_0 m_1 m_2}{4\pi(R_1 + R_2)^3}, \tag{4.1}$$

where the magnetic moments, in case of a homogeneous volume susceptibility, can be calculated with

$$m = \frac{4}{3}\pi R^3 \chi \frac{B}{\mu_0} \tag{4.2}$$

in which χ is the magnetic volume susceptibility and B the magnetic field strength in Tesla. Using equation 4.2 in 4.1 leads to a magnetic torque of

$$\tau_{mag} = \frac{4\pi\chi^2 B^2}{3\mu_0} \frac{(R_1\,R_2)^3}{(R1 + R2)^3}. \tag{4.3}$$

The maximum torque at constant magnetic field and a homogeneous susceptibility can be determined by solving the partial derivative to the radius of the particle and equalize it to zero:

$$\frac{\partial \tau_{mag}}{\partial R_1} \propto \frac{R_1^2 R_2^3}{(R_1 + R_2)^4} - \frac{R_1^3 R_2^2}{(R_1 + R_2)^4} = 0. \tag{4.4}$$

Which has the solution $R_1 = R_2$. So the magnetic torque of a dimer is the largest when the two particles are of equal size.

The derivation of the viscous torque of a dimer with particles of different sizes is more complex, the derivation is given in the appendix A3. The results are shown in 4.4a, where the viscous and also the magnetic torque of a dimer are plotted as a function of R_1/R_2. The torques are normalized at $R_1/R_2 = 1$. Both torques of a dimer are decreasing with an increasing size dispersion. But the magnetic torque decreases much faster than the viscous torque. The magnetic torque divided by the viscous torque is also plotted in the same figure. This ratio, which is proportional to the critical frequency, is decreasing for an increasing size dispersion.

*The torque depends on the angle between the major axis of the dimer and the field, maximum is at 45°, see section 1.4.

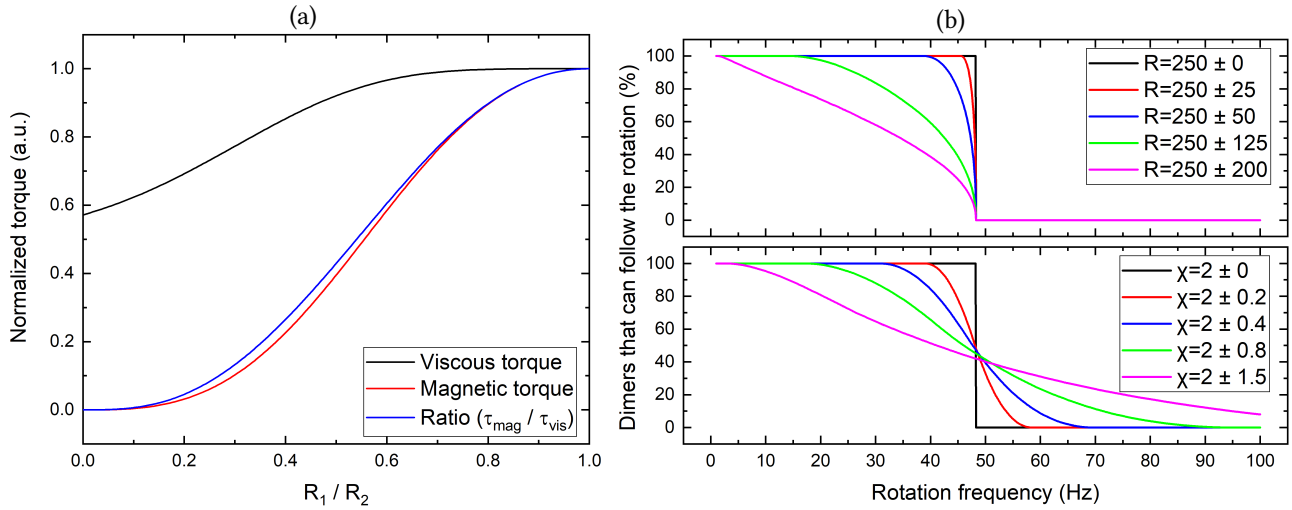

Fig. 4.4: **The torque and critical frequency. a** The normalized viscous torque and magnetic torque of a rotating dimer as a function of the ratio between the radii (R_1 and R_2) of both particles. The torques are normalized on the torque of a monodisperse dimer i.e. $R_1/R_2 = 1$. Also the ratio, the magnetic torque divided by the viscous torque, is plotted, which is proportional to the critical frequency of the dimer. The larger the size dispersion of a dimer the lower the critical frequency. **b** The percentage of dimers of a batch of disperse particles that can follow the rotation of the field versus the rotation frequency of the field. The top graph corresponds to a batch of particles with a size dispersion, according to an uniform distribution. The particles a susceptibility of 2 and have a mean radius of $250\,\mathrm{nm}$ with a dispersion up to $200\,\mathrm{nm}$. The bottom graph corresponds to a batch of particles with a dispersion in the magnetic volume susceptibility. The particles have a radius of $250\,\mathrm{nm}$ and have a susceptibility of 2 with a dispersion up to 1.5

So far only a single dimer is considered. The dimers of a batch of polydisperse particles have all a different critical frequency. A simulation is used to investigate the effect of polydispersity on the critical frequency of a batch of particles. In the simulation many dimers are formed of particles with random sizes or of particles with random magnetic volume susceptibilities. Fig. 4.4b shows the results of this simulation, where the percentage of dimers that can follow the rotation of the field is plotted against the rotation frequency. This is comparable to the critical frequency measurement of Fig. 4.3. The top graph shows the curves corresponding to an increasing size dispersion, the volume susceptibility of the particles is constant with a value of 2. The curve of the monodisperse batch ($R = 250 \pm 0$) is a step function. All dimers can follow the rotation of the magnetic field up to the critical frequency, above the critical frequency no dimers can follow the rotation anymore. The larger the size dispersion the larger the deviation from this step function. There are no dimers that have a larger critical frequency than the dimers of the monodisperse batch. A dimer with two equally sized particles have the largest critical frequency according to equation 4.4, the critical frequency of such a dimer is given by equation 1.16 and does not depends on the size but on the susceptibility. The susceptibility of all particles in the batch is the same. Thus no dimer can have a larger critical frequency than the critical frequency of a homogeneous dimer.

The bottom graph of Fig. 4.4b shows the curves corresponding to a batch of particles with a dispersion in the volume susceptibility, but with a monodisperse size. The monodisperse batch ($\chi = 2 \pm 0$) results again in a step function. A dispersion in the volume susceptibility causes a deviation from this step function. In this case it is possible to have dimers that have a higher critical frequency than dimers of the monodisperse batch. The viscous torque of all dimers is equal because the particles are of equal size, but the magnetic torque increases with the volume susceptibility. When two particles with a relative high susceptibility form a dimer, the critical frequency of this dimer is higher.

From this simulations it can be concluded that the deviation, of the critical frequency from an ideal batch, increases with the dispersion of the particles. The simulations are performed with uniform distributions, so the particles have an uniform probability to have any size within the range of sizes. Simulations that are

performed with normal distributions give similar results, the larger the size dispersion the large the deviation from the ideal line. The results of the simulations can explain the difference between the curves of the Ademtech and silica particles from Fig. 4.3. The silica particles seem to be the most monodisperse. The lower critical frequency of the Ademtech particle is most likely caused by the large size dispersion. The polystyrene particles also have a low critical frequency, but this is not related to a larger size dispersion. Also a dispersion in the susceptibility is unlikely because the curve as function of the frequency of the polystyrene particles of Fig. 4.3 is not similar to the curves from bottom graph of Fig. 4.4b. According to Fig. 4.4b about $50\,\%$ of the dimers can follow the rotation at the predicted critical frequency, which is not the case for the polystyrene particles. The reason for the low critical frequency of the polystyrene particles is unclear. It might be related to the surface roughness which leads to a larger viscous torque, but this is not investigated.

4.3 Effect of polydispersity on the actuation phase

The size dispersion might have a negative effect on the linear increase of the Fourier amplitude of the scattering signal in the actuation phase of an OMC experiment. A possible effect is that the magnetically induced encounter rate is different for each particle, because the encounter rate depends on the magnetic moment and thus on the size of the particles. The result is a bias for forming dimers of the larger particles of the distribution. In order to investigate the effect of the size dispersion on the actuation phase, a simulation is used which will be explained in detail.

4.3.1 Brownian dynamics simulation

A Brownian Dynamics (BD) simulation is performed, in order to investigate the magnetically induced encounter kinetics of particles with a large size distribution. In this simulation, magnetic particles are initially randomly distributed in a volume of $(0.14 \times 0.14 \times 0.14)\,\mathrm{mm}^3$, with an average particle to particle distance of $11\,\mu\mathrm{m}$, which corresponds to a particle concentration of $1.3\,\mathrm{pM}$ and 2000 particles. The position of each particle is given by vector $\vec{r_i} = (x_i, y_i, z_i)$. The size of the particles is an input parameter and is varied from 200 to $800\,\mathrm{nm}$. The particles have a Brownian motion depending on the size of the particles (R) and the thermal energy ($\mathrm{k_B T}$). The Brownian motion is quantified by the mean squared displacement (MSD) which is

$$\langle x^2 \rangle = 6Dt = \frac{k_B T}{\pi \eta R} t \tag{4.5}$$

where t is the time and D the diffusion constant and η the viscosity of the medium in which the particles move.

The particles move in the presence of an external magnetic field of $4\,\mathrm{mT}$, that rotates in the x-y-plane at $5\,\mathrm{Hz}$, see Fig. 4.5a. Due to this field the particles have an induced magnetic moment that is parallel to the field. The magnetic moment of a particle depends linearly on the particle volume. The magnetic force between two particles, which is the results of the dipole-dipole interaction can be computed with[35]

$$\vec{F}_{mag} = \frac{3\mu_0}{4\pi|\vec{r}|^4}\left[(\hat{\vec{r}} \times \vec{m_1}) \times \vec{m_2} + (\hat{\vec{r}} \times \vec{m_2}) \times \vec{m_1} - 2\hat{\vec{r}}(\vec{m_1} \cdot \vec{m_2}) + 5\hat{\vec{r}}\left((\hat{\vec{r}} \times \vec{m_1}) \cdot (\hat{\vec{r}} \times \vec{m_2})\right)\right] \tag{4.6}$$

in which $\vec{r}$ is the distance between two particles, $\hat{\vec{r}}$ is the unit vector in the same direction of $\vec{r}$, and $\vec{m_1}$ and $\vec{m_2}$ are the magnetic moments of the two particles, which are assumed to be point dipoles. In the simulation, the x-, y, and z-components of the distance vector and the magnetic moment are used to compute the three components of the magnetic force. The distance vector $\vec{r}$ splits in

$$r_x = x_2 - x_1, \quad r_y = y_2 - y_1, \quad r_z = z_2 - z_1 \tag{4.7}$$

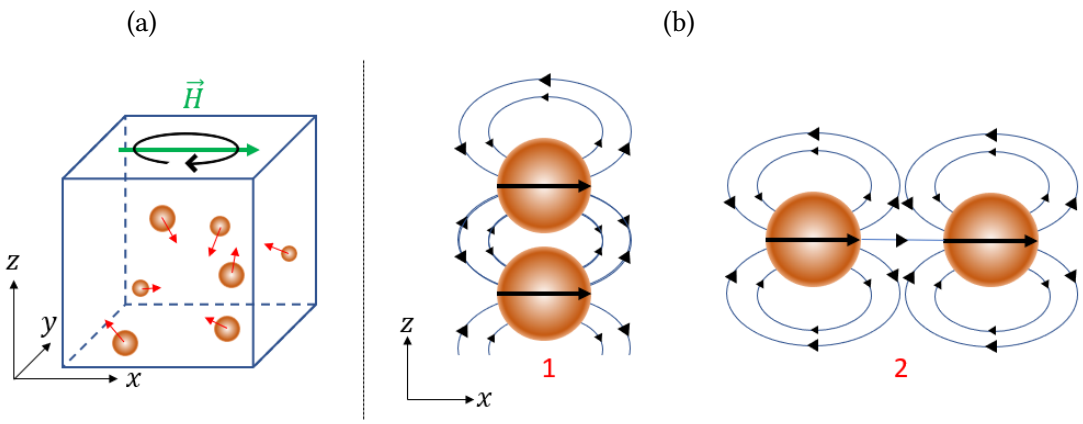

Fig. 4.5: **Setup of the simulation. (a)** The particles move in a volume (without boundaries) in the presence of a rotating external magnetic field ($B = 4\,\mathrm{mT}$, $f_r = 5\,\mathrm{Hz}$). **(b)** When two particles are aligned as in case 1, the particles repel each other in the z-direction. In case 2 the particles attract each other in the x-direction.

where x_i, y_i, and z_i are the coordinates of particle i. The components of the magnetic moment of particle i are

$$m_{i,x} = |m_i| \sin(\omega t), \qquad m_{i,y} = |m_i| \cos(\omega t), \qquad m_{i,z} = 0, \tag{4.8}$$

where ω is the angular frequency of the rotating magnetic field and t is the time. The moment in the z-direction is always zero because the magnetic field is parallel to the x-y plane. The force between two particles is repulsive when the moment of the particles are perpendicular to $\vec{r}$ (case 1 of Fig. 4.5b), and is attractive when the magnetic moments are parallel to $\vec{r}$ (case 2 of Fig. 4.5b).

The net force that a particle experiences is the sum of all the interactions with its neighbouring particles in a range of $10\,\mu\mathrm{m}$. Particles that are further away have a negligible contribution because the force has an $1/r^4$ dependency, at $10\,\mu\mathrm{m}$ the interaction energy is less than $1/20\,\mathrm{k_B T}$ according the equation 1.6. The net force is used to compute a movement which is in the same direction of the net force. The displacement of a particle depends on the magnetic force and the drag force. The velocity of each particle can be computed by equalizing the magnetic force to the drag force, which results in the following equation for the velocity in the x-, y-, and z-direction

$$v_{x,y,z} = \frac{\vec{F}_{mag,x,y,z}}{6\pi\eta R} \tag{4.9}$$

in which η is the viscosity of the medium and R the radius of the particle. It is assumed that the particles have no inertia, so they have immediately the velocity given by 4.9, a validation for this assumption is given in the appendix A4.

An actuation phase of 20 seconds is simulated by splitting the 20 seconds in small time steps Δt. Each time step involves the steps that are shown in the block diagram of Fig. 4.6. First the magnetic force on each particle and the corresponding velocity is computed, and the random Brownian motion of each particle is determined. The net velocity of the particles times Δt gives the displacement of the particles. Subsequently the new positions of all particles are computed. When the distance between two particles has become smaller than the sum of the radii of both particles, the particles form a dimer. In the same way larger clusters can be formed. Once a cluster is formed, it stays intact until the end of the simulated actuation phase. A formed cluster rotates around its center of mass with the major axis of the cluster parallel to the field. A cluster still has a magnetic interaction with other particles and a Brownian motion, which depends on the cluster size. The magnetic interaction between the particles that are part of the same cluster is ignored to prevent the particles to move through each other. Over time more and more cluster will be formed. The moment when a cluster is formed and the cluster number are saved. The result of the simulation is a plot of the number of clusters versus the time. In the supplementary information S3 results of the simulation are shown for different input parameters in order to validate the simulation.

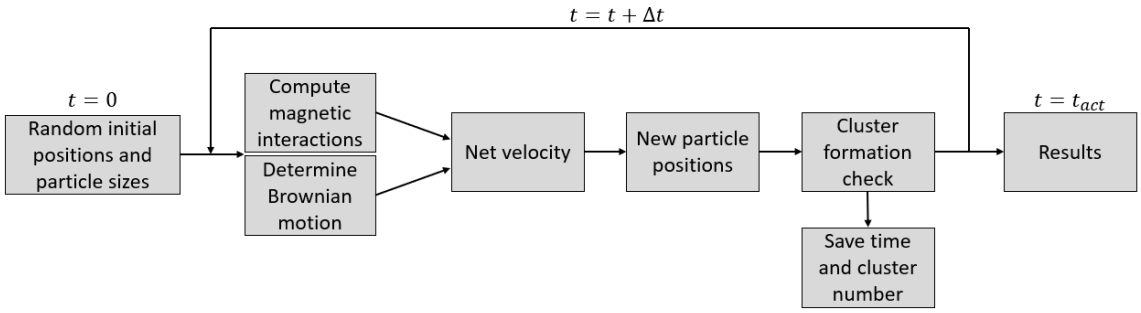

Fig. 4.6: **Block diagram of the simulation** First the positions and particle sizes are randomly determined. In each time step Δt: the movement due to Brownian motion and magnetic interaction of the particles is computed and the new positions are determined. If the distance between two particles becomes smaller than the sum of the radii of both particles, a cluster is formed. When a cluster is formed the time and the cluster number is saved. The steps are repeated until the actuation time t_{act} is reached.

In order to investigate how the cluster formation rate depends on the size of the particle, the simulation is run for different particle size distributions: Three times with a monodisperse distribution with particles of 200, 500, and $800\,\mathrm{nm}$ and with particles of a size that is randomly sampled from a normal distribution around $500\,\mathrm{nm}$ and a variance of $125\,\mathrm{nm}$, which is similar to the size dispersion (CV $= 25\,\%$) of the Ademtech particles. Fig. 4.7a shows the result of the simulations, the number of clusters in plotted versus the time for four different runs. As expected the larger particles cluster faster than the smaller particles, due to the stronger dipole-dipole interaction of larger particles. The simulation of a batch with disperse particles shows similar cluster kinetics as a batch of monodisperse particles with the same average size. The number of clusters for the disperse batch is larger, but the difference is less than $10\,\%$.

The scattering signal in an OMC experiment is the sum of the scattering of all clusters. In order to simulate the scattering signal, the BD simulation is combined with a Mie scattering simulation, that is developed by Mackowski et al.[36]. In this simulation the scattering at clusters is computed as a function of the cluster orientation and detector angle. In the supplementary information S4 more details about the simulation are given.

The scattering at rotating dimers is computed at a scattering angle of $90°$. The diameters of the particles are varied from $200\,\mathrm{nm}$ to $800\,\mathrm{nm}$. From the resulting scattering signals the Fourier transformation is taken. The heat map of Fig. 4.7b shows the |A2f| peak of the Fourier spectrum for the different diameters of the particles of a dimer.

Fig. 4.7b shows the normalized Fourier amplitude (|A2f| peak) of the signal of all possible Ademtech dimers that can be formed out of two particles with a size varying from $200\,\mathrm{nm}$ to $800\,\mathrm{nm}$. From this figure, the overall trend that a larger dimer scatters more light can be considered as false. The heat map shows a complex dependency on the diameter of the particles, and the |A2f| peak of the scattering signal is not always larger for larger dimers.

Fig. 4.7c shows the results of combining the two simulations, the Fourier amplitude of the Mie scattering at each dimer that is formed in the BD simulation results in the scatting signal, which is plotted as a function of time. The scattering at the small particles ($d = 200\,\mathrm{nm}$) is smaller than the larger particles and the encounter rate is lower. A combination of both effects causes the low signal, the opposite holds for the particles of $800\,\mathrm{nm}$. The curves of the monodisperse ($d = 500\,\mathrm{nm}$) particles and the disperse particles ($d = 500\,\mathrm{nm} \pm 25\%$) are similar. The effect of the large size dispersion is not visible in the signal. From this figure it can be concluded that using monodisperse particles for measuring dimer concentrations in an OMC experiment does not give a significant advantage relative to particles with a large size dispersion.

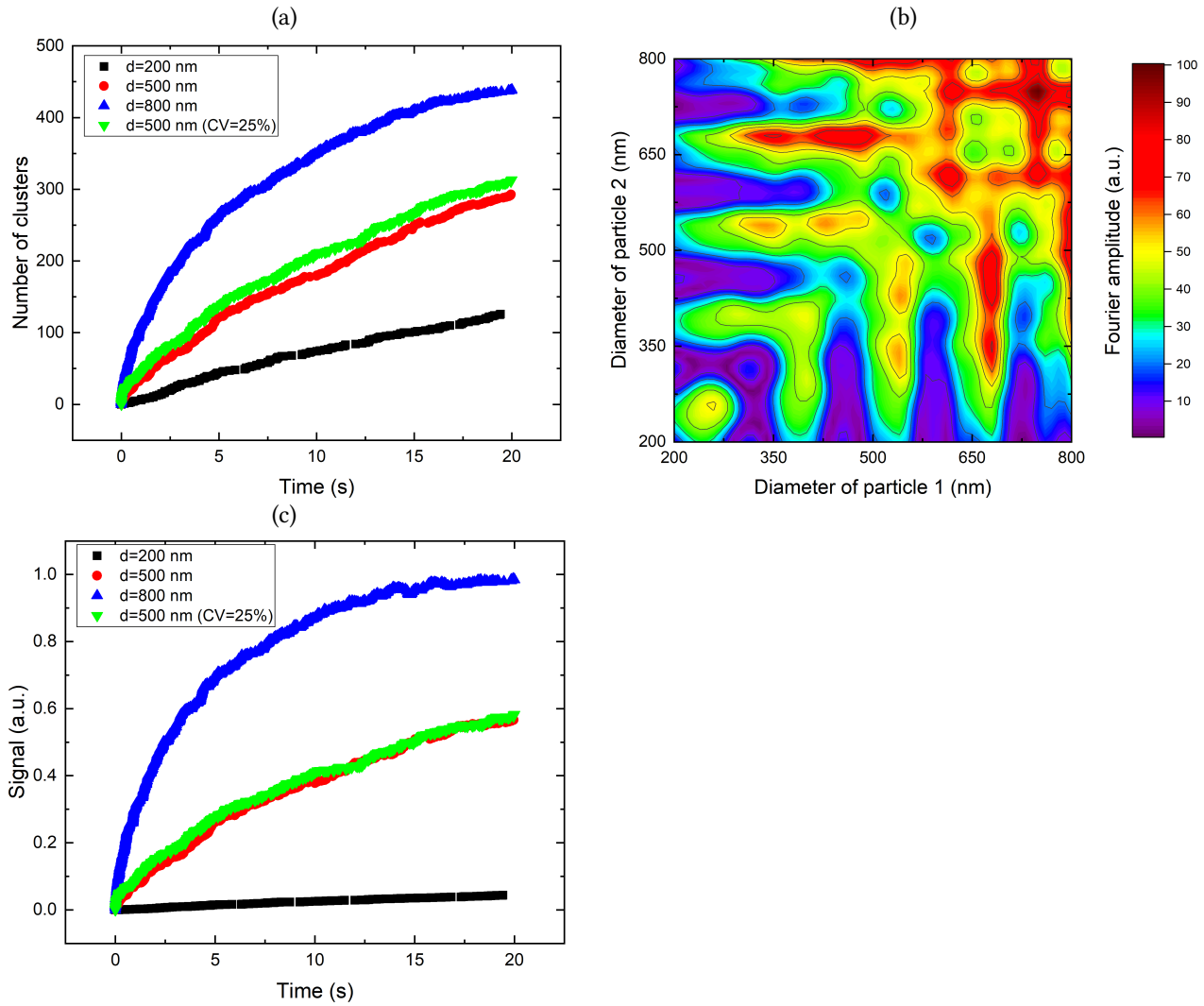

Fig. 4.7: **Results of the simulations. (a)** The number of clusters plotted versus the time for four runs: three times with monodisperse particles with a diameter of 200, 500, and 800 nm and one time with polydisperse particles of $500\,\mathrm{nm} \pm 25\%$. **(b)** Heatmap of the Fourier amplitude (|A2f|) of the simulated signal of each possible dimer consisting of particles the range from 200 to 800 nm. **(c)** Combination of the Mie scattering simulation and the BD simulation. The scattering signal is plotted versus the time for the four different runs of **(a)**.

4.4 Overview

The average magnetic volume susceptibility of the three particles does not differ significantly. The Ademtech particles have a large size dispersion, but this has no significant effect on signal during the actuation phase of an OMC experiment. However, in an OMC experiment the particle encounter step is not the only step of the chemical cluster formation, there is also the chemical aggregation. Scheepers et al.[16] demonstrated that the magnetic induced aggregation rate κ_{agg}^{mag} (from Fig. 1.2) depends on the magnetic interaction strength between the particles of a dimer. With polydisperse particles, this magnetic interaction varies from dimer to dimer, and thus the aggregation rate of every dimer is different. This project focuses on measuring these rates, so it is preferred that every magnetic dimer that is formed during the actuation phase has the same rate of transforming into a chemical dimer. This makes the Ademtech particles less suitable for the experiments of this project. The dispersion of the silica particles is less than the Ademtech particles. The size dispersion of the polystyrene particles is small, but the magnetic dispersion of the polystyrene particles is unclear. The large surface roughness of the polystyrene particles might give problems with the functionalization of the particles. Therefore the silica particles will be used for the coming experiments of this project.

Chapter 5

Measuring specific aggregation rates

This chapter describes the measurement of aggregation rates with the DNA-based model system as described in the introduction. The first section of this chapter gives more details about how this DNA system works. In the second section the DNA coating on the particles is quantified using a supernatant assay. Thereafter the chapter continues with an experiment to reduce the non-specific interaction between particles. The last two sections are about the main experiments of this project: Specific interaction is measured and distinguished from the non-specific interaction, and the possibility of tuning the aggregation rate is investigated.

5.1 DNA-sandwich assay

To measure a specific aggregation rate using the OMC experiment, a sandwich-DNA model system is used. The target molecule is a DNA strand (analyte strand) that is sandwiched between DNA strands that are attached to the particles (docking strand). Fig. 5.1a shows the docking strand (blue) and the analyte strand (green)*. The docking strand consists of two single stranded oligonucleotides (Docking-A and Docking-B). Docking-A is a strand with 20 nucleobases and has a biotin molecule that is attached to the 5' end. Docking-B is a longer oligonucleotide that contains 35 nucleobases, of which 20 nucleotides are complementary to the Docking-A and the other 15 bases are complementary to the analyte strand The two strands of the analyte DNA both have a length of 35 nucleobases, of which 20 complementary nucleobases. Both ends of the analyte strands have a length of 15 bases and are symmetric. i.e. both ends can bind to two the same docking strands. Details about the single stranded oligos of the docking and analyte strands are given in Table 5.1. One criterion of the DNA oligos is a low haipin melting temperature. The melting temperature of each oligo is given in

*These colours are used in every figure that shows an analyte or/and a docking strand.

Table 5.1: **DNA oligonucleotides:** Overview of the four single stranded oligos of which two of them form the docking strand and two the analyte strand. The sequence, the strongest hairpin melting temperature T_m, and the binding energy to a complementary strand of each oligo is given.

Strand	**Sequence**	**Hairpin T_m**	**Binding energy**
Docking-A	Biotin - 5' CCT CCC AGC CCA TCC TAA CC 3'	$10\,^{\circ}\mathrm{C}$	to Docking-B: $-72\,\mathrm{k_B T}$
Docking-B	5' AAA CAA GAC GAC GAA GGT.. ..TAG GAT GGG CTG GGA GG 3'	$18\,^{\circ}\mathrm{C}$	to Docking-A: $-72\,\mathrm{k_B T}$
Analyte-A	5' TTC GTC GTC TTG TTT CCA.. ..CCC TTC CCG CCC CTC CC 3'	$12\,^{\circ}\mathrm{C}$	to Analyte-B: $-84\,\mathrm{k_B T}$ to Docking-B: $-47\,\mathrm{k_B T}$
Analyte-B	5' TTC GTC GTC TTG TTT GGG.. ..AGG GGC GGG AAG GGT GG 3'	$25\,^{\circ}\mathrm{C}$	to Analyte-A: $-84\,\mathrm{k_B T}$ to Docking-B: $-47\,\mathrm{k_B T}$

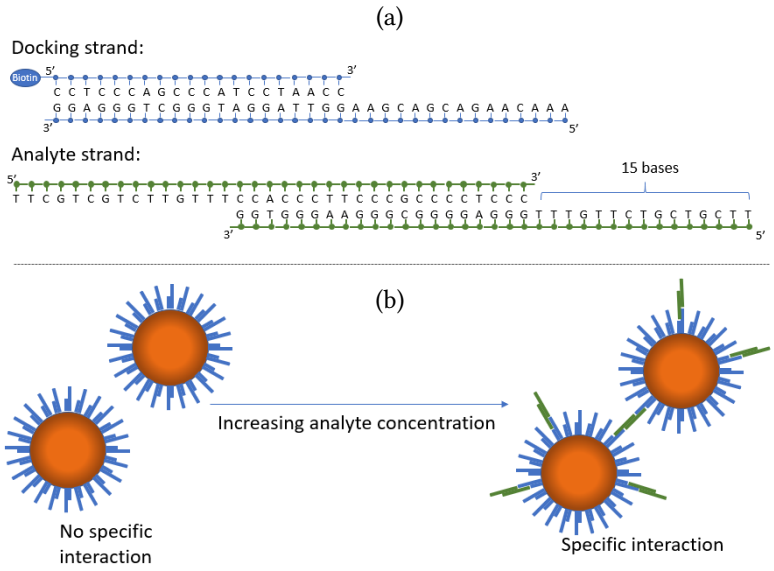

Fig. 5.1: **Schematic representation of the used DNA sandwich model system (a)** The design of the docking- and analyte strands. A biotin molecule is attached to the docking strand for the functionalization of the microparticles. The analyte strand has 15 complementary bases to the docking strand.
(b) Schematic picture of functionalized particles. The particles are functionalized with the docking strands. Without analyte, no specific interaction is possible between the particles. Increasing the analyte concentration results in more and more specific interaction between the particles, up to a certain maximum due to saturation of the docking strands.

the table. Other requirements of the design of the strands are given in the supplementary information S1. The biotin molecule that is bound to the docking strand is used to attach docking strands to the streptavidin coated particles. This streptavidin-biotin bond is one of the strongest non-covalent bonds in nature[37] and is assumed to not dissociate during an experiment.

In the presence of an analyte strand, two particles that are functionalized with docking strands can form a chemical dimer. This binding process is called specific binding, or specific interaction, see Fig. 5.1b. Without the analyte strands, two particles cannot have a specific interaction, only non-specific interactions. Some examples of non-specific interactions are hydrophobic or electrostatic interactions. These interactions should be suppressed as much as possible, which will be discussed later in this chapter. To measure the specific aggregation rate, the particles will be coated with a high docking strand density. By increasing the analyte concentration the aggregation rate should increase up to a certain maximum after which the rate decrease due to saturation of the docking strands. When all docking strands are bound to an analyte the specific binding between an analyte and a free docking strand is not possible anymore, and only non-specific particle aggregation can occur.

5.2 Binding capacity

The DNA docking strands are attached to the streptavidin coated particles via the biotin group on the 5' end of the docking strand as described in the functionalization protocol of section 2.3. To quantify the DNA (docking strand) coverage on the particles after the functionalization, a supernatant assay is performed, which has been explained in section 2.6.

First the fluorescent signal of biotin-atto655 (b-atto) molecules is calibrated as a function of the b-atto concentration. The calibration curve is shown in Fig. 5.2a. The fluorescent signal increases linearly with the b-atto

concentration. In order to determine the binding capacity of streptavidin coated particles, different amounts of b-atto are added to a particle solution. After incubation the particles are removed from the solution by a magnetic washing step and the fluorescence of the supernatant is measured. The result of this measurement is also shown in Fig. 5.2a.

At low concentration all the b-atto molecules in the solution can bind to the particles, so almost no molecules are left behind in the supernatant. Hence the measured fluorescence is equal to the background fluorescence F_0. At higher concentrations, the particles do not contain enough streptavidin molecules to bind all the b-atto molecules that are present in the solution. This results in a sharp increase of the fluorescence from the supernatant when the biotin capacity is reached. Above this concentration, the measured fluorescence starts approaching the calibration curve. The relative difference, between the amount of b-atto that is added and that is adsorbed decreases for higher b-atto concentrations. The relative adsorption of b-atto molecules by the particles, compared to the amount of b-atto that is added to the solution, can be calculated with equation 5.1 and is shown in Fig. 5.2b:

$$A(\%) = \left(1 - \frac{F_{sup} - F_0}{F_{cal} - F_0}\right) \cdot 100\%, \tag{5.1}$$

in which F_0 is the background fluorescence, F_{cal} and F_{sup} are the fluorescence intensities of the calibration and the supernatant assay respectively.

At low concentrations the relative adsorption of the b-atto molecules is $100\,\%$. The adsorption decreases for higher b-atto concentrations. From the relative adsorption, absolute values for the adsorption can be calculated. The absolute adsorption is plotted (blue) in the same figure. The adsorption saturates to a value of $(37 \pm 5)\,\mathrm{pmol}$, which corresponds to about $(2.8 \pm 0.4) \times 10^4$ b-atto molecules per particle. This amount can be compared to the maximum number of streptavidin molecules that can be physically present on a perfectly smooth sphere with a diameter of $511\,\mathrm{nm}$. The surface area of a sphere (with $d = 511\,\mathrm{nm}$) divided by area that is occupied by a streptavidin molecule ($\approx 25\,\mathrm{nm}^2$) gives a maximum of about 3.3×10^4 streptavidin molecules on one particle, which is in the same order of magnitude as the maximum binding capacity but just outside the error of the measured b-atto binding capacity. Note that this is the maximum surface coverage of

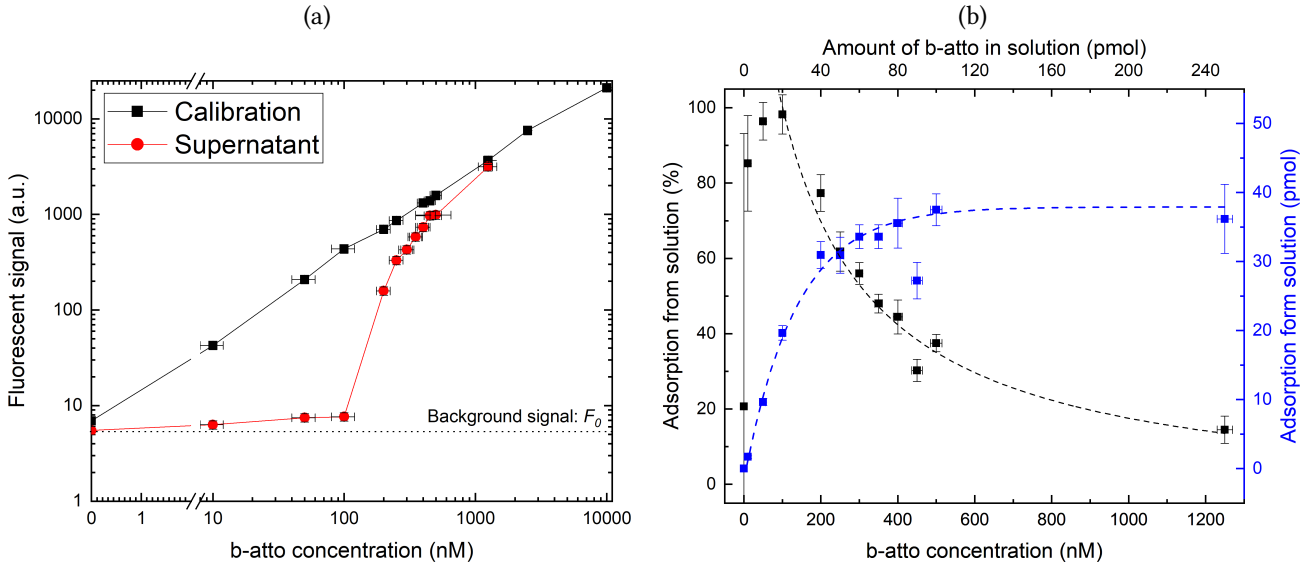

Fig. 5.2: **Results of the biotin-atto supernatant assay (a)** Fluorescent signal as a function of the biotin-atto concentration for the calibration measurement and the supernatant assay. **(b)** The absorption of biotin-atto molecules from the solution during the incubation against the biotin-atto concentration. The left axis shows the absorption in percentage of the total biotin-atto that was added to the solution, these values are calculated from Fig. 5.2a using equation 5.1. The right axis corresponds to the absolute values of the adsorbed b-atto. The adsorbed b-atto saturates to a value of $(37 \pm 5)\,\mathrm{pmol}$, which corresponds to the maximum binding capacity of about $(2.8 \pm 0.4) \times 10^4$ boitin-atto molecules per particle. The dashed blue and black lines are guides for the eyes.

streptavidin of a perfect smooth sphere, the actual coverage may deviate from this due to surface roughness or a not perfect homogeneous coverage of streptavidin molecules. One streptavidin molecule has four binding pockets for a biotin molecule, so a higher biotin binding capacity might be expected. But not all binding pockets are available when the streptavidin is coated on the surface of the particles. Also the biotin-atto molecule is larger than a free biotin molecule so maybe not all available binding pockets can be occupied by the biotin-atto molecule.

The binding capacity for the docking strands is expected to be lower because a docking strand is much larger than a b-atto molecule ($15\,\mathrm{kDa}$ versus $0.5\,\mathrm{kDa}$). Also the particles and the docking strands are negatively charged, they repel each other which hinders the functionalization. In order to determine the DNA binding capacity of the particles an indirect supernatant assay is performed and an adsorption model is used. First the particles are functionalized with the docking strands as described in section 2.3. Subsequently b-atto is added to the functionalized particles ([particle] $= 6.5\,\mathrm{pM}$, [b-atto] $= 1.5 \times 10^5\,\mathrm{pM}$). After incubation, the solution is washed magnetically and the fluorescence of the supernatant is measured. When the functionalization with docking strands is efficient, many of the streptavidin molecules are occupied by the docking strands and there are only few streptavidin molecules left that can bind to the b-atto. In this case, many b-atto molecules stay behind in the supernatant. Hence, with an efficient DNA-functionalization, the measured fluorescence is high, due to the relative high biotin-atto concentration in the supernatant. In this way the surface coverage with DNA can be quantified with the supernatant assay. The quantification is done with an adsorption model.

5.2.1 Adsorption model

An adsorption model is used to quantify the number of functionalized docking strands on the particles. The model is based on the adsorption of biotin-atto molecules. The number of b-atto molecules that are adsorbed by the particles (N_{bA}) as a function of time is given by the differential equation

$$\frac{\partial N_{bA}}{\partial t} = N_b(t)\, N_f(t)\, \kappa_{bs}, \tag{5.2}$$

where N_b is the number of b-atto molecules that are present in the solution, N_f the number of available (free) binding spots on the surface of the particles and κ_{bs} is the reaction rate constant of the b-atto - streptavidin reaction. It is assumed that the biotin-streptavidin binding is strong and irreversible.

N_b and N_f are decreasing in time when b-atto molecules bind to the binding spots. The number of available binding spots and the number of unbound b-atto molecules are given by

$$N_b = N_{b0} - N_{bA}, \qquad N_f = N_{f0} - N_{bA} \tag{5.3}$$

in which N_{b0} is the initial amount of b-atto molecules, and N_{f0} is the binding capacity per particle times the number of particles in solution. Filling in equation 5.3 in equation 5.2 results in the following differential equation

$$\frac{\partial N_{bA}}{\partial t} = \big(N_{b0} - N_{bA}(t)\big)\,\big(N_{f0} - N_{bA}(t)\big)\,\kappa_{bs}. \tag{5.4}$$

This equation is solved numerically using:

$$N_{bA}(t + \Delta t) = N_{bA}(t) + \big(N_{b0} - N_{bA}(t)\big)\,\big(N_{f0} - N_{bA}(t)\big)\,\kappa_{bs}\Delta t \tag{5.5}$$

This equation is solved in MATLAB where t is increased with steps of $\Delta t = 0.5\,\mathrm{ms}$, from 0 to $3600\,\mathrm{s}$, which corresponds to the incubation time during an experiment. The binding capacity, which is equal to the number of available binding spots N_{f0}, depends on the particle concentration and the binding spots per particle. The value for N_{b0} is the amount of b-atto that is added to the particle solution which is in the supernatant experiment varied from 0 to $250\,\mathrm{pmol}$. The reaction rate κ_{bs} has been determined with the supernatant experiment.

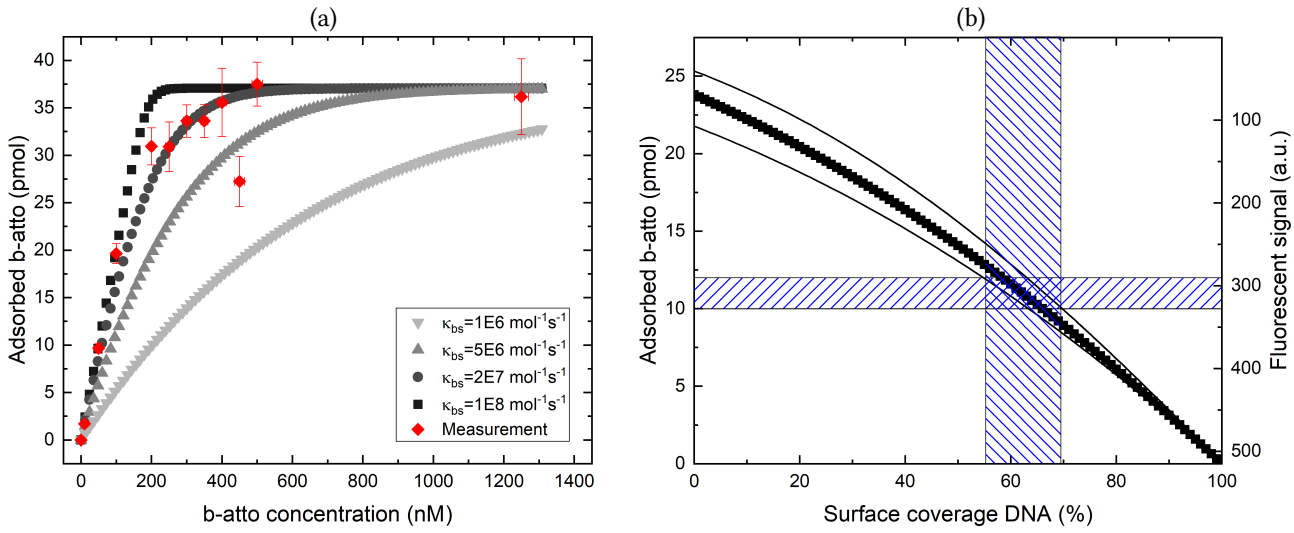

Fig. 5.3: **The results of the adsorption model (a)** The amount of adsorbed b-atto as a function of the b-atto concentration according to equation 5.5, for different values of the adsorption rate κ_{bs} and an incubation time of 3600 seconds. Also the measurements results of Fig. 5.2b are plotted in this figure. With the rate $\kappa_{bs} = (2.0 \pm 0.5) \times 10^{-7}\,\mathrm{s}^{-1}$ the model and the measurement have similar results. **(b)** The adsorbed b-atto and the fluorescent signal as a function of the DNA surface coverage according to the model using an adsorption rate $\kappa_{bs} = (2.0 \pm 0.5) \times 10^{-7}\,\mathrm{s}^{-1}$, the black lines around the curve corresponds to the lower and upper value of κ_{bs}. With a surface coverage of $100\,\%$ no b-atto can be adsorbed, so all the b-atto remains in the supernatant which leads to a high fluorescent signal. The measured fluorescent signal has a value of 308 ± 15, which corresponds to an adsorption of b-atto of $(11 \pm 1)\,\mathrm{pmol}$ as shown by the blue marked bar. The corresponding surface capacity is $(62 \pm 7)\,\%$.

Fig. 5.3 shows the number of bound b-atto molecules N_{bs} as a function of the concentration of b-atto N_{b0} that is added, for different values of κ_{bs}. Also the measurement data is plotted in this figure. The model corresponds to the measurement when the rate $\kappa_{bs} = (2.0 \pm 0.5) \times 10^{7}\,\mathrm{s}^{-1}$. With the obtained value for κ_{bs}, the surface coverage of DNA can be determined.

The DNA surface coverage is related to the number free streptavidin molecules on the surface and thus on N_{s0}. With equation 5.5 the number of adsorbed b-atto molecules N_{bA} is computed as a function of N_{s0} using $\kappa_{bs} = (2.0 \pm 0.5) \times 10^{7}\,\mathrm{s}^{-1}$ and $N_{b0} = 30\,\mathrm{pmol}$, which is the same amount b-atto that is added in the experiment. The result is shown in Fig. 5.3b, where the adsorbed b-atto is plotted against the relative surface coverage of DNA. Fig. 5.3b shows on the right y-axis the inversely related fluorescent signal of the supernatant. When the adsorbed b-atto is zero, all the b-atto molecules that are added remain in the supernatant, hence the fluorescent is the highest at zero adsorption.

Fig. 5.3b is used for the quantification of the DNA surface coverage. With the indirect supernatant assay, a fluorescent signal of 308 ± 15 is measured, this is the horizontal marked bar in the graph. This corresponds to $(11 \pm 1)\,\mathrm{pmol}$ of adsorbed b-atto. This adsorption has a corresponding DNA surface coverage of $(62 \pm 7)\,\%$, which corresponds to about $17\,000 \pm 2000$ docking strands per particle.

This maximum surface coverage can be realized with an excess of DNA during the functionalization. In some experiments particles with a lower surface coverage are used. These particles are functionalized in a docking strand solution of $3.0 \times 10^{-8}\,\mathrm{M}$, while the particle solution is unchanged ($6.5\,\mathrm{pM}$). With the indirect supernatant experiment, the surface coverage is determined to be $(20 \pm 5)\,\%$. Considering the amount of DNA molecules that are added to the particles a surface coverage of $17\,\%$ can be reached. So the surface coverage is expected to be between the 15-17 %. This corresponds to about 4400 ± 300 docking strands.

5.3 Decreasing non-specific interactions

The specific aggregation rate of particles can only be measured when it is significantly larger than the non-specific aggregation rate. The maximum rate that can be measured with an OMC experiment with an actuation time of 20 seconds, according to equation 3.3, is $\kappa_{agg}^{mag} = 0.1\,\mathrm{s}^{-1}$. The non-specific aggregation rate should be suppressed as much as possible to have an as large as possible dynamic range for measuring the specific aggregation rate. This section describes how the non-specific aggregation is reduced.

Experiments to measure the non-specific aggregation rate have been done with the OMC experiment using the protocol that is shown in Fig. 5.4a. In the experiment three phases can be distinguished: 1) the measurement phase in which magnetic pulses are applied to measure the initial dimer concentration. 2) the actuation phase in which the field in turned on. 3) the diffusion phase where the field in off. The scattering signal for different particle functionalizations is measured with two cycles of this protocol. In Fig. 5.4a the |A4f| peaks of the different measurements are shown, the corresponding non-specific aggregation rate are shown in Fig 5.4b.

The high non-specific aggregation rate of the non-functionalized or partially functionalized (16 % DNA) streptavidin coated silica particles is characterized by an increase of the |A4f| at the first measurement phase, normally the |A4f| stays the same during a measurement phase. Also most of the dimers that are formed during the first actuation phase have become chemical dimers, which is demonstrated by the high |A4f| peaks at the second measurement phase, the higher this level the more chemical cluster are formed and thus the higher the aggregation rate.

Particles with a higher DNA functionalization (62 % DNA) have a lower non-specific aggregation rate. The |A4f| peak is not increasing at the first measurement phase and the level of the |A4f| peak at the second measurement phase are lower than the non-functionalized and partially functionalized (16 % DNA) particles. This reduction in non-specific aggregation rate might be related to the repulsive force between the negatively

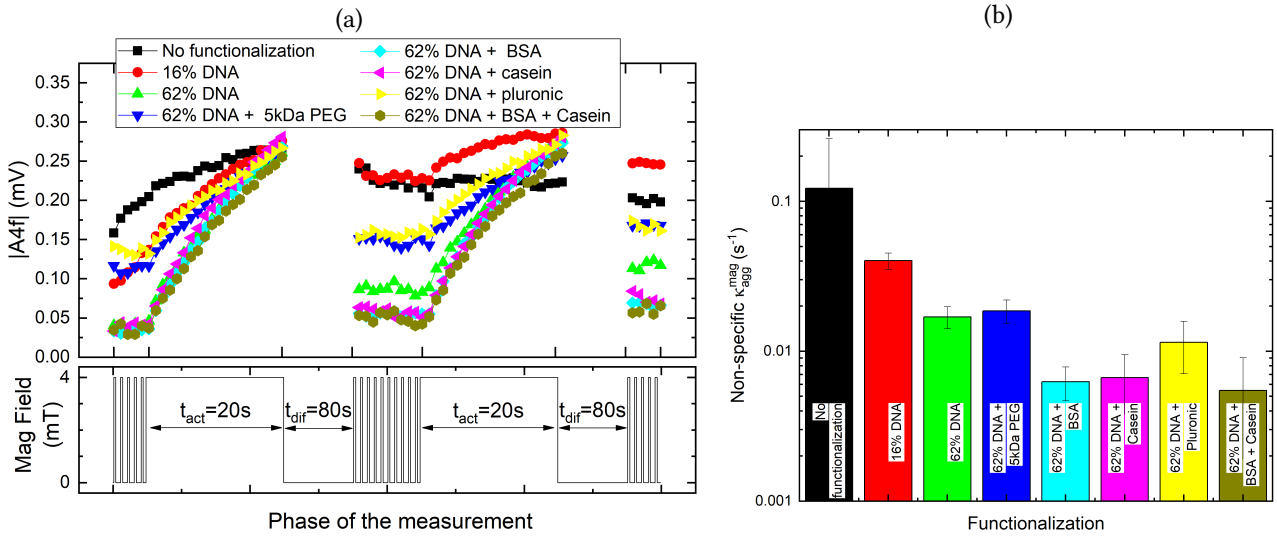

Fig. 5.4: **Measurement of the non-specific interaction for different functionalizations. (a)** The |A4f| peak is plotted throughout the phases of one measurement. The measurement protocol is presented as the magnetic field against the time, showing the measurement phase, the actuation phase (20 seconds) and the diffusion phase (80 seconds). The measurement phase consists of short pulses where the field is turned on for 0.4 s and breaks where the field is off for 10 s. The phases corresponds to the phases as explained in Fig. 3.4. When the field is on it is rotating at 5 Hz. No data is available in the diffusion phase because in this phase the dimer in the solution are not rotating. The |A4f| peaks for 8 different measurement of samples with different functionalizations is plotted. **(b)** The non-specific magnetically induced aggregation rate of particles with the same functionalizations as in graph **(a)**.

charged DNA-molecules, a higher surface coverage with DNA results in a larger repulsive force.

A DNA surface coverage of $62\,\%$ is the maximum coverage. So in order to reduce the non-specific rate further the functionalized particles are coated with blocking molecules. Three common used blocking molecules are tested: Bovine serum albumin (BSA), pluronic F-127, and casein. Also a functionalization with DNA and PEG molecules ($5\,\mathrm{kDa}$) is tested.

The non-specific κ_{agg}^{mag} of functionalized particles with a coating of BSA or casein is reduced to below $0.01\,\mathrm{s}^{-1}$. Pluronic F-127 does not have the desired effect on the non-specific aggregation. Also functionalization with PEG molecules results in a higher non-specific aggregation.

The lowest non-specific aggregation rate is measured with the sample of particles with a DNA functionalization and a coating of BSA and casein. The corresponding rate is $(6 \pm 3) \times 10^{-3}\,\mathrm{s}^{-1}$. This gives a dynamic range for specific interaction of over one order of magnitude. The coating with BSA and casein is used for the further experiments.

5.4 Measuring specific aggregation rates

The first main goal of this project is to measure the specific particle aggregation rate of the DNA model system and distinguish this rate from the non-specific aggregation rate. In this section the results of the measurement of the magnetically induced aggregation rate κ_{agg}^{mag} as a function of the analyte concentration will be discussed.

The samples are prepared by mixing the DNA functionalized particles with an analyte solution and incubating for 5 minutes, as described in section 2.7. Measuring the specific aggregation rate is done with functionalized silica microparticles with a $16\,\%$ and $62\,\%$ surface coverage of docking strands. The particles are mixed with different analyte concentrations, varying from 0 to $500\,000$ analyte strands per particle. Note that this is the amount of analyte that is present in the solution per particle, this is not necessarily the same as the numbers of analytes that are bound to a particle, because not all the analyte strands may have bound to a particle within the incubation time of 5 minutes.

Fig. 5.5a shows the 4f Fourier amplitude of four measurements with the $62\,\%$ docking strand coverage, for four different analyte concentrations. The black curve in this figure corresponds to the non-specific interaction, because no analyte is added to the corresponding sample. The other curves corresponds to analyte concentrations of 50, 400, and 700, relative to the particle concentration. The specific interaction can be clearly distinguished from non-specific interaction. The number of formed chemical dimers increases with the analyte concentration as shown by the Fourier amplitude of the 4f component during the second and third measurement phase. This indicates that the magnetically induced aggregation rate increases with the analyte concentration. The curve that corresponds to the relative analyte concentration of 700 shows the effect of depletion in the second actuation phase. Due to the large number of dimers formed during the first actuation the number of single particles is decreased significantly which results in a lower dimer formation rate. Normally, both actuation cycles are used to calculate the magnetically induced aggregation rate κ_{agg}^{mag} using equation 3.3, but in case of depletion, this equation is not accurate anymore. Therefore, in case of high cluster formation rates, only the first actuation cycle is used to calculate κ_{agg}^{mag}.

The κ_{agg}^{mag} as a function of the analyte concentrations is shown in Fig. 5.5b, for the two docking strand functionalizations ($16\,\%$ and $62\,\%$ DNA). The results of the measurement can be qualitatively interpreted with Fig. 5.5c. At zero analyte, the aggregation rate is low because only non-specific aggregation happens. At low analyte concentrations ($[a]/[p] < 1000$) both curves increase with the analyte concentration. In this regime the orientation of the particles is important for the aggregation. During the actuation phase aligned and mis-aligned clusters are formed, so not all magnetic dimers can become a chemical dimer. By increasing the analyte concentration, the chance to form an aligned dimer increases. At low analyte concentrations, the

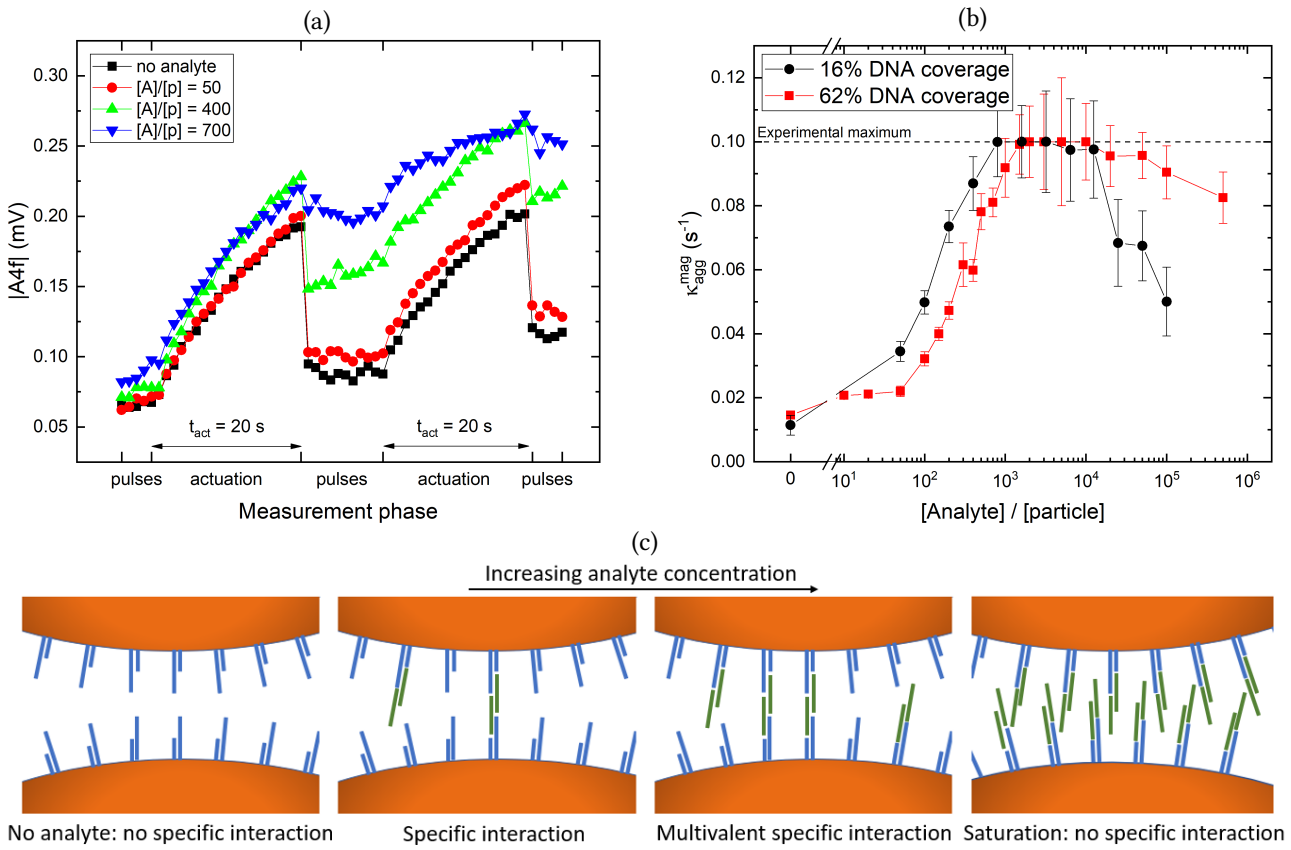

Fig. 5.5: **Measurement of the specific aggregation as a function of the analyte concentration. (a)** The |A4f| peak of the pulses of the measurement and actuation phases of an OMC experiment are plotted for four different analyte concentrations.
(b) The specific magnetically induced aggregation rate as a function of the analyte concentration, for the two different DNA coverage percentages (16 and 62 %). The analyte concentration is relative to the particle concentration. The experimental maximum value for the magnetically induced aggregation rate of $0.1\,\mathrm{s}^{-1}$ is indicated by the dashed line.
(c) The effect of increasing the analyte concentration on the specific interaction. The specific interaction increases with the analyte concentration up to a maximum due to saturation. When all docking strands are saturated. i.e. occupied by an analyte strand, there is no specific interaction anymore, because two analyte strands cannot make a chemical bond.

curve of the 16 % DNA coverage increases faster than the 62 %. This might be related to the electrostatic repulsion between the particles, which is lower for the 16 % DNA coverage because in this case there are less negatively charged molecules on the surface of the particles. The differences in the aggregation rate are discussed in more detail in chapter 7.

At concentrations of $1000 < [a]/[p] < 10000$ the upper limit for κ_{agg}^{mag} is reached, which means that all magnetic dimers have become chemical dimers during the actuation phase. In this regime the chance that a magnetic dimer is aligned correctly is (almost) one. Also multivalent bonds can be formed, so the probability that an aligned dimer become a chemical dimer is larger than in the low analyte concentration regime. At higher analyte concentrations, above a relative concentration of 10 000, the κ_{agg}^{mag} decreases, due to saturation of the docking strands. When all docking strands are occupied with an analyte strand, the specific interaction is zero. The curve of the 16 % DNA shows the saturation effect at lower analyte concentration, which can be explained because the number of docking strands is lower.

5.5 Tuning the aggregation rate

The second goal of this project is to investigate if it is possible to tune the aggregation rate κ_{agg}^{mag}. For this purpose the particles have not only been coated with docking strands but also with PEG molecules of different molecular weights. These PEG molecules may act as an entropic barrier, so the reaction rate between the docking strands and analyte strands might be reduced.

The particles are first functionalized with DNA to get a $16\,\%$ docking strands surface coverage. This low coverage is used because also the PEG molecules should be able to bind to the particles. The rest of the particle is functionalized with biotinylated PEG molecules. An excess of biotin-PEG (5×10^6 pM) is added to the particles solution (6.5 pM) and is incubated for 1 hour, as described in section 2.3.

Four different PEG sizes are used for the functionalization. The molecular weights of these PEG molecules are 5, 10, 20, and 30 kDa. Fig. 5.6 shows the Flory diameters of the PEG molecules compared to the length of a docking and an analyte strand. The Flory diameter of the 20 and 30 kDa PEG molecules (28 and 35 nm) are larger than the docking-analyte strand complex which has a length of 22 nm.

The magnetically induced aggregation rate of the particles with different PEG functionalizations are measured as a function of the analyte concentration using the same measurement protocol as in section 5.4. The results of these measurements are shown in Fig. 5.7. First the aggregation rate increases with the analyte concentration, at higher concentration it decreases, which is characteristic for specific interactions. The specific interaction can be distinguished from the non-specific interaction for every used PEG functionalization.

Particles with the 5, 10, or 20 kDa PEG functionalization have comparable aggregation rates as particles without PEG. The particle aggregation rate at zero analyte for the particles with a 5, 10, or 20 kDa PEG functionalization is higher compared to the particles without PEG. Also the rate at the relative analyte concentration of 100 000 is the higher. This indicates that the non-specific aggregation rate increases for a 5, 10,

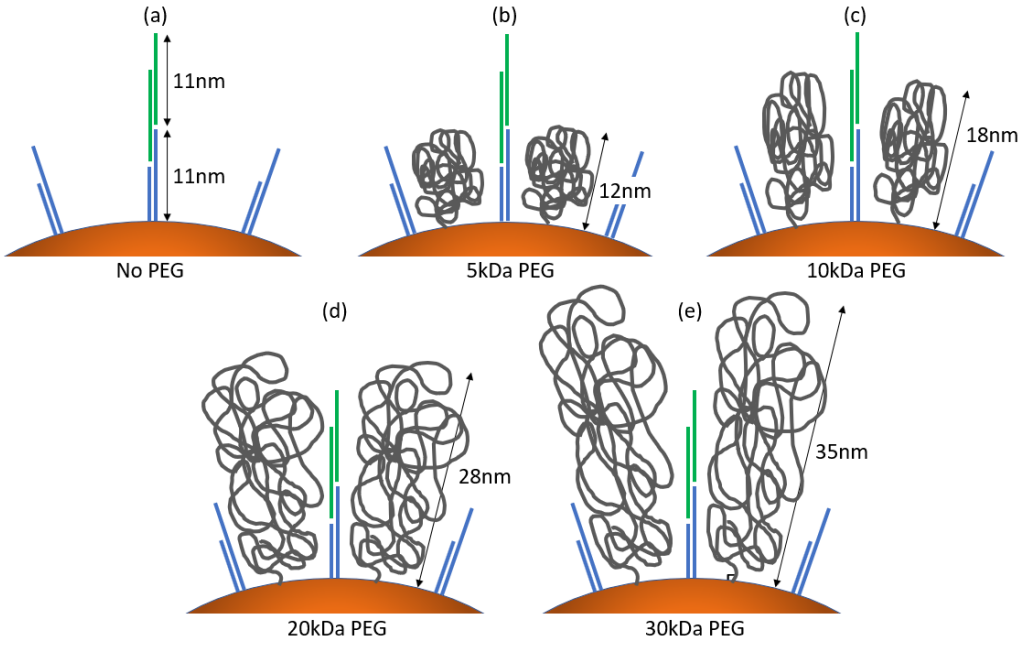

Fig. 5.6: **Sizes of the PEG molecules compared to the DNA strands: (a)** Functionalized particles with DNA, showing the length of the docking strand (blue) and the analyte strand (green).
(b-e) Functionalized particles with DNA and PEG molecules of 5, 10, 20, and 30 kDa. The lengths are on the same scale as in image **(a)**. The sizes of the PEG-molecules are based on the Flory radius calculated with equation 1.21.

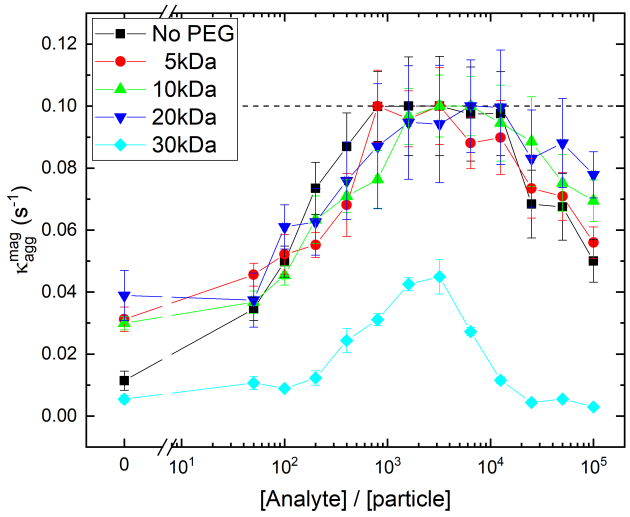

Fig. 5.7: **Influence of PEG on the aggregation rate. (a)** The magnetically induced aggregation rate as a function of the analyte concentration relative to the particle concentration, for different PEG functionalizations. The experimental maximum value of $\kappa_{agg}^{mag} = 0.1\,\mathrm{s}^{-1}$ is indicated by the dashed line.

or 20 kDa PEG functionalization. Only the 30 kDa functionalization results in a significantly different κ_{agg}^{mag}. The curve of the 30 kDa functionalization does not reach the experimental maximum value, the maximum of the curve is at a rate of about $0.05\,\mathrm{s}^{-1}$. Both the non-specific and the specific interactions of the 30 kDa PEG functionalized particles are reduced, compared to the particles without PEG.

The measured curves are further discussed with the help of a simulation, which is explained in the next chapter.

Chapter 6

Simulation of specific particle aggregation

In order to interpret the results of the OMC experiments on the aggregation rate in the DNA sandwich system, simulations have been performed. A parameter scan has been carried out to investigate how the model parameters influence the resulting κ_{agg}^{mag}.

6.1 Basics of the simulation

The actuation phase of the OMC experiments is simulated by forming (magnetic) dimers of the DNA functionalized particles. Dimers are formed at a constant rate for a period that is equal to the actuation time. Each dimer has a certain interaction time, in which a magnetic dimer can transform into a chemical dimer. This interaction time depends on the moment when the dimer is formed. The first dimer that is formed in the simulation has an interaction time that is equal to the actuation time, the second dimer, which is formed a few milliseconds later, has a slightly shorter interaction time. This continues up to the last dimer which has only an interaction time of a few milliseconds.

A dimer has an interaction volume, which is the volume around the contact area of the two particles, see Fig. 6.1a. The number of free docking strands and analyte strands in this interaction volume determines the reactivity of a dimer. When no analyte strands or no free docking strands are present in this volume the dimer is mis-aligned and no specific bond can be made between the particles. The probability of forming a chemical dimer increases with the number of free docking strands and analyte strands in the interaction volume.

The interaction area A_{int} of both particles in the interaction volume is a spherical cap on the particle surface that has a size of

$$A_{int} = 2\pi Rh, \tag{6.1}$$

where R is the particle radius, and h the height of the cap (see Fig. 6.1). The average number of docking strands per particle N_D in the interaction volume is the product of the total number of docking strands per particle $N_{D,tot}$ and the interaction area divided by the total surface of the particle

$$N_D = \frac{A_{int}}{4\pi R^2} N_{D,tot} \tag{6.2}$$

In the same way the average number of analytes N_A per particle in the interaction volume is given by

$$N_A = \frac{A_{int}}{4\pi R^2} N_{A,tot} \tag{6.3}$$

in which $N_{A,tot}$ is the total number of analytes on the particle. The number of free docking strands N_F in the interaction volume per particle decreases when analyte strands bind to the free docking strands, the number

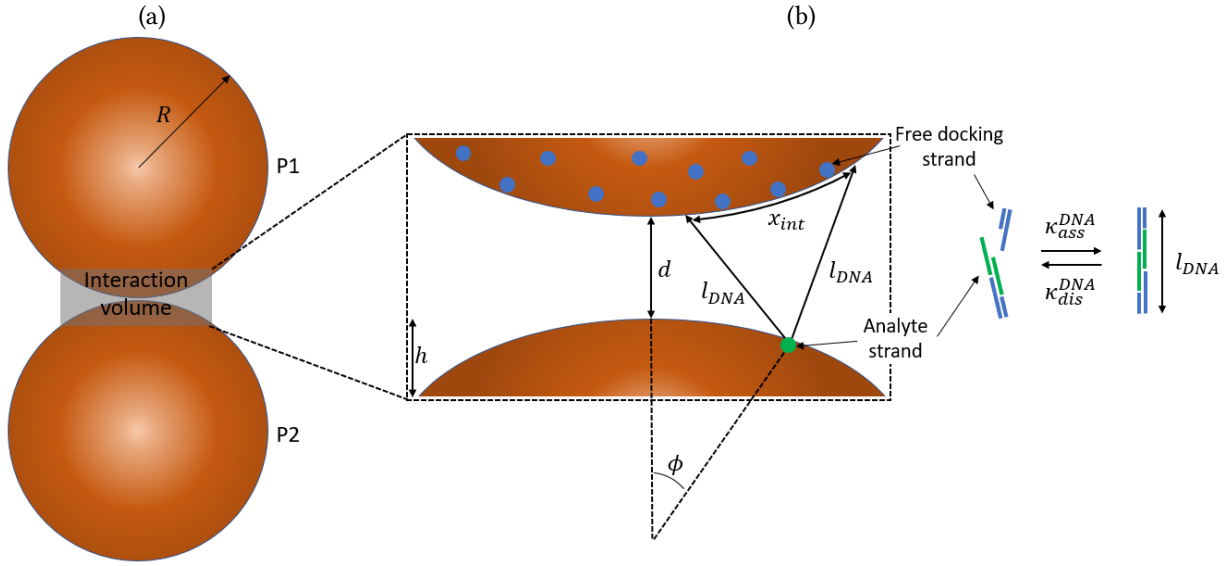

Fig. 6.1: **The simulation concept. (a)** A dimer of particles $P1$ and $P2$ with radius R have an interaction volume (grey marked area) in which the docking and analyte strands can form a bond to make a chemical dimer. **(b)** A zoom of the interaction volume of two particles with an inter particle distance d that shows the geometry that is used in equation 6.6. The position of the analyte on $P2$ is determined by angle ϕ. The analyte can only bind the docking strands that are closer than the length of the DNA complex l_{DNA}. The docking strands on $P1$ that are in range of the analyte strands are positioned in a circle with diameter x_{int}. The reaction between an analyte and free docking strand is quantified by the association and dissociation rate κ_{ass}^{DNA} and κ_{dis}^{DNA}.

of free strands is given by

$$N_F = N_D - N_A. \tag{6.4}$$

In the simulation the docking and analyte strands are assumed to be points on the particle surface. It is assumed that the number of free docking strands are homogeneously distributed in the interaction volume. The surface density of the free docking strands is given by

$$\sigma_F = \frac{N_F}{A_{int}} \tag{6.5}$$

The analyte strands that are present in the interaction volume are randomly distributed on the interaction area. For each analyte strand in the interaction volume that is attached to a particle, the number of free docking strands to which the analyte strand can bind on the other particle of the dimer is determined. The analyte strand can only bind to docking strands that are close enough, i.e. the maximum distance between the analyte and docking strand is the total length of the docking-analyte-docking complex (l_{DNA}). The geometry is explained in Fig. 6.1. Each analyte strand on one particle has a *binding area* (A_{bind}) on the other particle which contains all the free docking strands to which the analyte can bind. The binding area is a circular area with a diameter x_{int} which is defined in Fig. 6.1. The distance d, the position of the analyte strand (quantified with ϕ) and the length of the complex l_{DNA} determine the size of the binding area. The derivation for x_{int} is given in appendix A5.

The number of free docking strands that are in the range of analyte strand i is given by

$$N_{F,i} = \sigma_F \pi (x_{int}/2)^2. \tag{6.6}$$

This number is computed for each analyte strand on both particles.

The probability that at least one chemical bond will be made in the interaction volume of a dimer depends on the number of possible bonds, the interaction time t_{int} of the dimer and the chemical association rate κ_{ass}^{DNA} of the DNA system. In order to determine if a chemical bond is made the interaction time of a dimer is split

in small time steps Δt. The probability that a bond is made in a time step is given by

$$P = \left(\sum_i N_{F,i} \right) \Delta t \, \kappa_{ass}^{DNA} \tag{6.7}$$

In every time step a random number between 0 and 1 is generated. When the random number is smaller than the probability computed in equation 6.7, the dimer is transformed into a chemical dimer. This is repeated $t_{int}/\Delta t$ times.

Another way to form a chemical dimer is via non-specific interaction. The probability of forming a chemical dimer non-specifically depends on the interaction time and the non-specific aggregation rate κ_{agg}^{NS} and is given by

$$P_{NS} = \Delta t \, \kappa_{agg}^{NS} \tag{6.8}$$

In the same way as specific aggregation, a random number is generated for each dimer and each time step to determine if it becomes a chemical dimer.

The output of the simulation is the number of chemical dimers N_{chem} that are formed. The particle aggregation rate is computed using a rewritten form of equation 3.3

$$\kappa_{agg}^{mag} = \frac{N_{chem}}{N_{mag}} \frac{1}{t_{act}/2} = \frac{N_{chem}}{\kappa_{dim} \, t_{act}^2/2} \tag{6.9}$$

in which κ_{dim} is the dimer formation rate and t_{act} is the actuation time.

Particles are simulated as perfect spheres with a radius of $256\,\mathrm{nm}$. The particles are functionalized with docking strands, the average number of docking strands per particles varies between the 4000 and $17\,000$. Some of the docking strands are bound to an analyte strand, the number of analyte strands per particle is varied between the 0 and $17\,000$.

6.2 Parameter scan

The magnetically induced aggregation rate depends on a set of parameters, which are given in Table 6.1. Some of these parameters are unknown in a real OMC experiment. In the simulation, these parameters are estimated and varied systematically in order to investigate how they influence the results. The parameters that are known in an experiment, like the actuation time (20 seconds) and the size of the particles ($R = 256\,\mathrm{nm}$) are not changed in the simulation.

In the simulations the following parameters are varied: the association rate of the DNA strands (which is shown in Fig. 6.1), the number of docking strands per particle, the inter particle distance, and the number of analyte strands per particle. The results of the simulations are plots of the magnetically induced aggregation rate κ_{agg}^{mag} versus the number of analyte strands per particle. The effect on the particle aggregation rate of changing the parameters is discussed in detail.

Changing the specific interaction between particles can be done in two ways: 1) by changing the association rate between a single docking and analyte strand, i.e. changing κ_{ass}^{DNA}. 2) by changing the number of docking and analyte strands that can make a bond. In order to investigate the influence of changing the first parameter, the simulation is run several times for different association rates κ_{ass}^{DNA}, in the range of 5×10^{-5} to $2 \times 10^{-2}\,\mathrm{s}^{-1}$. The other parameters are kept constant: $d = 10\,\mathrm{nm}$ and $N_D = 4000$.

Fig. 6.2a shows the results of these simulations. The magnetically induced particle aggregation rate increases with the rate κ_{ass}^{DNA}. The specific interaction is characterized by first an increase with the amount of analyte and subsequently a decrease due to saturation of the docking strands. With the lowest rate $\kappa_{ass}^{DNA} =$

Table 6.1: An overview of the parameters used in the simulations to calculate the magnetically induced aggregation rate. The parameters that are unknown in the real experiments are estimated and varied in the simulations.

Parameters	**Measurement**	**Simulation**
Dimer formation rate	unknown, depends on magnetic field	$50\,\mathrm{s}^{-1}$
Actuation time	20 seconds	20 seconds
Particle size	511 nm	511 nm
Non specific aggregation rate		$1 \times 10^{-2}\,\mathrm{s}^{-1}$
Number of docking strands	4400 ± 400 or $17\,000 \pm 2000$ per particle	Varied from 2000 to 17 000 per particle
Number of analytes added	varied from 0 to 100.000 per particle	varied from 0 to 100.000 per particle
Number of analytes on a particle	Unknown, depends on κ_{on}	Is computed with κ_{on}
Analyte adsorption rate κ_{on}	Unknown	Varied from 1-10 $\times 10^{-5}\,\mathrm{s}^{-1}$
Particle to particle distance	Unknown	Varied from 0 to 30 nm.
Association rate of DNA strands	Unknown	Varied from 1×10^{-5} to $1 \times 10^{-2}\,\mathrm{s}^{-1}$

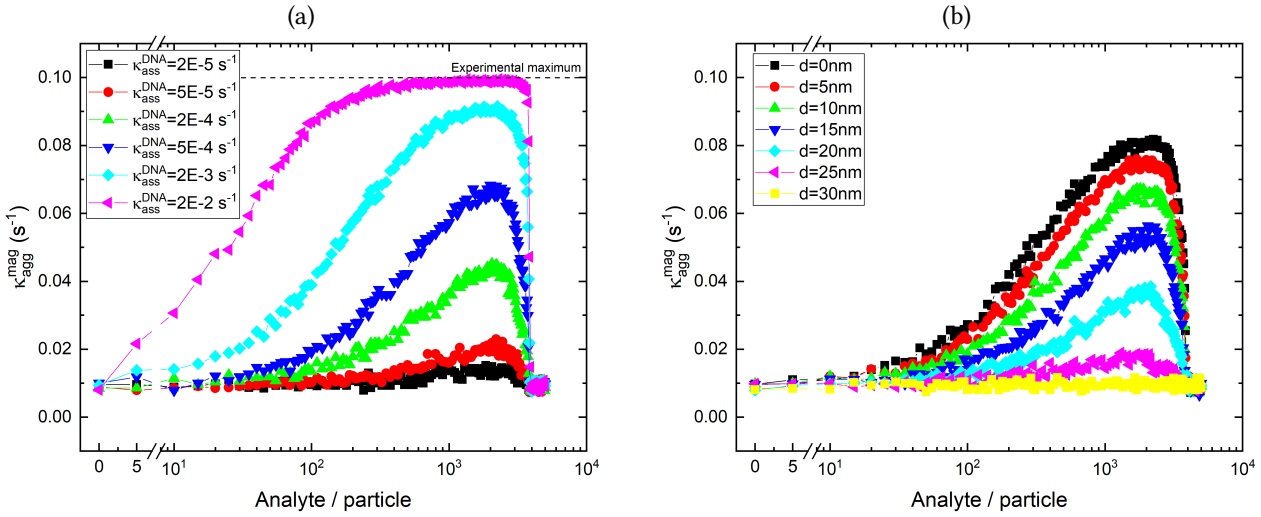

Fig. 6.2: **Simulation results. (a)** The particle aggregation rate κ_{agg}^{mag} is plotted as a function of the analyte concentration for different association rates κ_{ass}^{DNA} and a constant particle to particle distance $d = 10\,\mathrm{nm}$ and number of docking strands per particle $N_D = 4000$ are used. **(b)** The particle aggregation rate κ_{agg}^{mag} is plotted as a function of the analyte concentration for different inter particle distances with $\kappa_{ass}^{DNA} = 5 \times 10^{-4}\,\mathrm{s}^{-1}$ and $N_D = 4000$.

$5 \times 10^{-5}\,\mathrm{s}^{-1}$ this behaviour is almost not visible. The specific interaction is not significant with respect to the non-specific interactions. By increasing the specific aggregation rate κ_{ass}^{DNA} the difference between the specific and non-specific interaction becomes larger, i.e. the peak at around 2000 analyte/particle increases. The maxima of the simulated curves differ only in the vertical direction when the aggregation rate is varied.

The magnetic induced (particle) aggregation rate κ_{agg}^{mag} is not the same as the association rate of the DNA molecules κ_{ass}^{DNA}, because on a particle multiple reactions may happen (multivalent interaction), this results in a higher κ_{agg}^{mag} than the aggregation rate of the DNA. The computed κ_{agg}^{mag} can only be the same as the association rate of the DNA when exactly one analyte and one free docking strand can react with each other in the interaction volume. At a DNA association rate of $0.02\,\mathrm{s}^{-1}$, the experimental maximum value ($\kappa_{agg}^{mag} = 0.1\,\mathrm{s}^{-1}$) for the particle aggregation rate κ_{agg}^{mag} is reached. With this high DNA association rate κ_{ass}^{DNA} (almost) all magnetic dimers transform into chemical dimers during the actuation phase.

The specific interaction can also be changed by varying the number of DNA strands that can make a bond with strands on the other particle. This can be done by changing the inter particle distance or by changing the total number of docking strands on a particle (vary N_D). The effect of changing the inter particle distance on the κ_{agg}^{mag} is shown in Fig. 6.2b. The inter particle distance d is increased from 0 to 30 nm, while the other

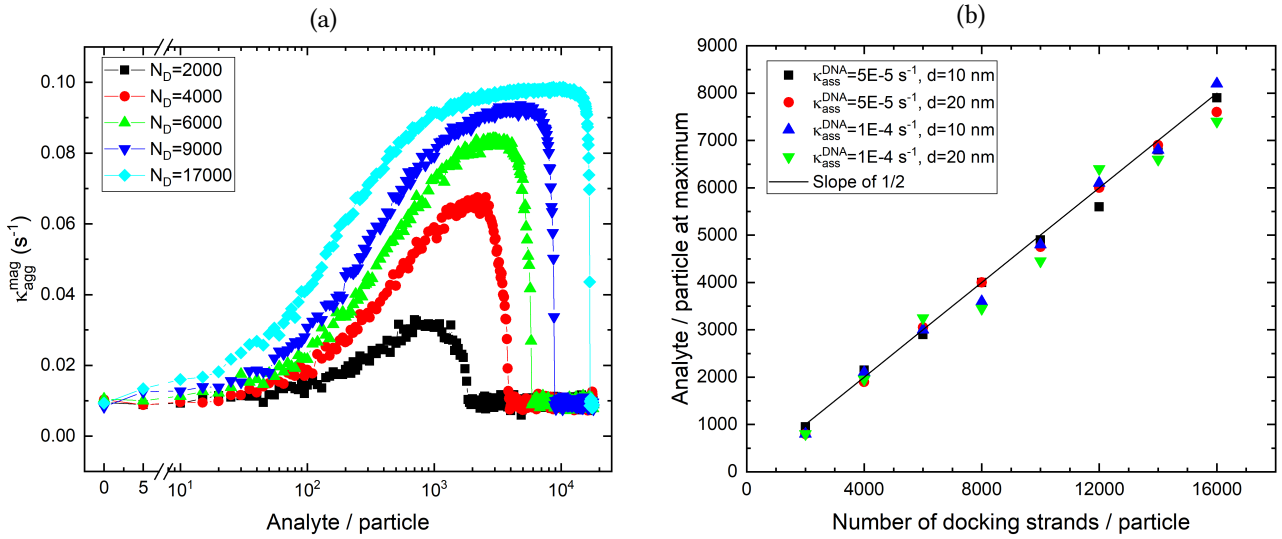

Fig. 6.3: **Simulation results. (a)** The κ_{agg}^{mag} as a function of the analyte concentration. The interaction depth is varied from 1-6 nm at a constant $\kappa_{ass}^{DNA} = 2 \times 10^{-4}\,\mathrm{s}^{-1}$, $N_D = 4400$. **(b)** The number of docking strands is varied from 4000-17 000, at a constant $\kappa_{ass}^{DNA} = 2 \times 10^{-4}\,\mathrm{s}^{-1}$ and $d_{int} = 3\,\mathrm{nm}$. The x-positions of the curves of different simulations, plotted against the number of docking strands on a particle. The datapoint are fitted with a line with a slope of 1/2, which indicates that the maximums of the curves are at the analyte concentration that is equal to half the number of docking strands.

parameters are kept constant: $\kappa_{ass}^{DNA} = 5 \times 10^{-4}\,\mathrm{s}^{-1}$, $N_D = 4000$. Increasing the distance results in a less reactive system. At a distance of 30 nm (or larger) the specific interaction cannot occur, because the particles are at a larger distance than the length of the DNA complex, and only non-specific aggregation happens.

Another way to change the number of docking strands in the interaction area is by varying the total number of docking strands on a particle. Experimentally, the number of docking strands is estimated to be 4400 for the 16 % DNA surface coverage and 17 000 for the 62 % DNA coverage. The effect on the κ_{agg}^{mag} of the different surface coverage is investigated with the simulation.

In the following set of simulations, the number of docking strands is increased from 2000 per particle to 17 000, while the inter particles distance d is kept constant at 10 nm and $\kappa_{ass}^{DNA} = 5 \times 10^{-4}\,\mathrm{s}^{-1}$. Fig. 6.3a shows the results of changing the total number of docking strands. The plots show that the system is more reactive when the number of docking strands is higher. This could be expected since equation 6.7 depends on the number of (free) docking strands. The maximum of the curves in the graph vary in height but also in horizontal position. Particles with a higher number of docking strands can adsorb more analyte strands, therefore the saturation point and the maximum is reached at higher analyte concentrations.

In order to investigate if the number of docking strands is the only parameter that determines the horizontal position of the top* of the curve, the simulation has been carried out several times, where the inter particle distance d, the DNA association rate k_{ass}^{DNA}, and the number of docking strands N_D are changed systematically. The horizontal position of the maximum of the generated curves of all these simulations is plotted against the number of docking strands in Fig. 6.3(b). Also a linear line is plotted with a slope of 1/2. The line fits the data points quite well. This indicates that the horizontal position of the maximum of the curves is at the analyte concentration where half of the docking strands has adsorbed an analyte strand. The slope of 1/2 can be explained with equation 6.7. The binding probability depends on the number of free docking strands and on the number of analyte strands, $N_{F,i}$ increases with the number of free docking strands, and the number of summation elements increases with the number of analyte strands. The maximum binding probability is at the number of analyte strands where the product of the number of the free docking and analyte strands is

*The horizontal position of the top is defined as the number of analyte per particle at the maximum of the curve.

the largest. Taking the derivative of the product $N_A N_F = N_A(N_D - N_A)$ with respect to N_A and solving the result to zero gives the number of analyte strand at the maximum, see equation 6.10, which has the result $N_A = N_D/2$.

$$\frac{\mathrm{d}N_A(N_D - N_A)}{\mathrm{d}N_A} = 2N_A - N_D = 0, \tag{6.10}$$

6.2.1 Changing κ_{on}

So far the simulation is based on the assumption that the number of analyte strands per particle is the same as the number of analyte that is added per particle. In reality this is not the case. The number of analyte strands per particle depends on the reaction rate κ_{on} which quantifies the reaction that is depicted in Fig. 6.4. Also the number of bound analytes depends on the concentration free docking strands $[F]$, and on the concentration analyte $[A]$. The concentration free docking strands corresponds to the number of free docking strands per particle multiplied with the particle concentration. The concentration of bound analyte $[N_A]$ can be calculated with

$$\frac{\mathrm{d}[N_A]}{\mathrm{d}t} = [F](t)\,[A](t)\,\kappa_{on}, \qquad [F](t) = [N_{D,tot}] - [N_A](t), \qquad [A](t) = [A_0] - [N_A](t) \tag{6.11}$$

where the free docking strand concentration $[F]$ is the difference between the total concentration of docking strands $[N_{D,tot}]$, which is the total number of docking strands per particle times the particle concentration, and the concentration of bound analyte $[N_A]$. In the same way $[A]$ is dependent on the initial analyte concentration $[A_0]$ and number of bound analyte $[N_A]$. Due to the decreasing numbers $[A]$ and $[F]$ the rate is not constant. Solving the differential equation 6.11 gives $[N_A]$ as a function of time t. This function saturates to $[N_{D,tot}]$ (if $[N_{D,tot}] < [A_0]$) or to $[A_0]$ (if $[A_0] < [N_{D,tot}]$). Fig. 6.4 shows the concentration of bound analyte $[N_A]$ against the time for different values for κ_{on} and a constant $[N_{D,tot}] = 17\,000\,\mathrm{pM}$ and $[A_0] = 5000\,\mathrm{pM}$. The values for the rate are around the measured rate of $4 \times 10^5\,\mathrm{s^{-1}\,M^{-1}}$ in the work from Zhang et al. [38]. It is debatable if this rate is correct because the docking strands are not free in solution but attached to the particles, therefor rates of ten times lower and higher are not excluded. The saturation value is reached faster when the rate κ_{on} is higher. After a certain incubation time, for example 300 seconds (which is also used in the experiments), the concentration bound analyte depends on the κ_{on}.

Fig. 6.5a shows the number of bound analyte versus the time for different values of $[A_0]$ at a constant $\kappa_{on} = 5 \times 10^5\,\mathrm{s^{-1}\,M^{-1}}$ and $N_{D,tot} = 17\,000\,\mathrm{pM}$. The graph shows that the concentration of bound analyte increases

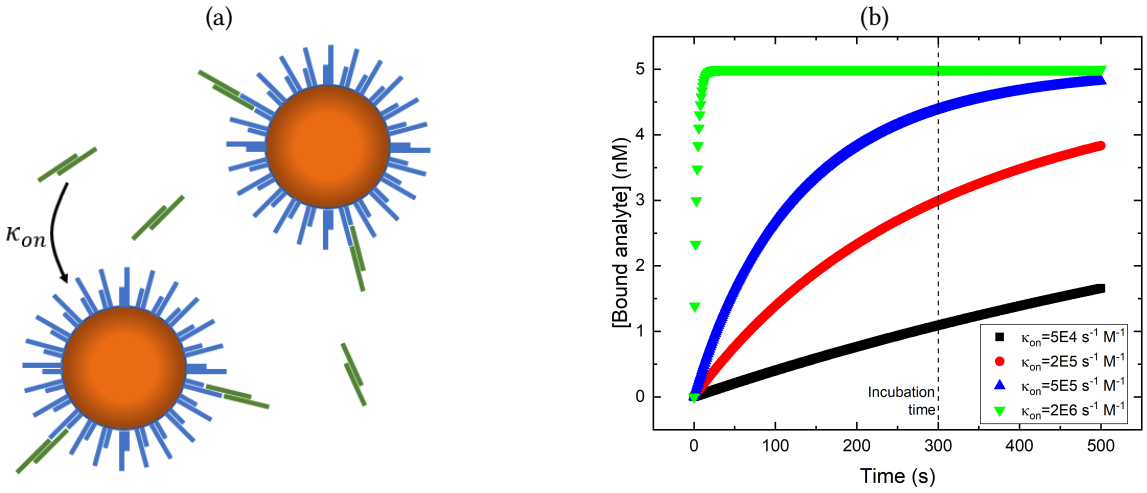

Fig. 6.4: **The analyte adsorption rate. (a)** Picture of the reaction to bind analyte strands on the particles, the reaction is quantified by the rate κ_{on}. **(b)** The number of bound analytes as a function of time for different value for κ_{on}, calculated with equation 6.11 where $[N_{D,tot}] = 17\,\mathrm{nM}$ and $[N_A] = 5\,\mathrm{nM}$.

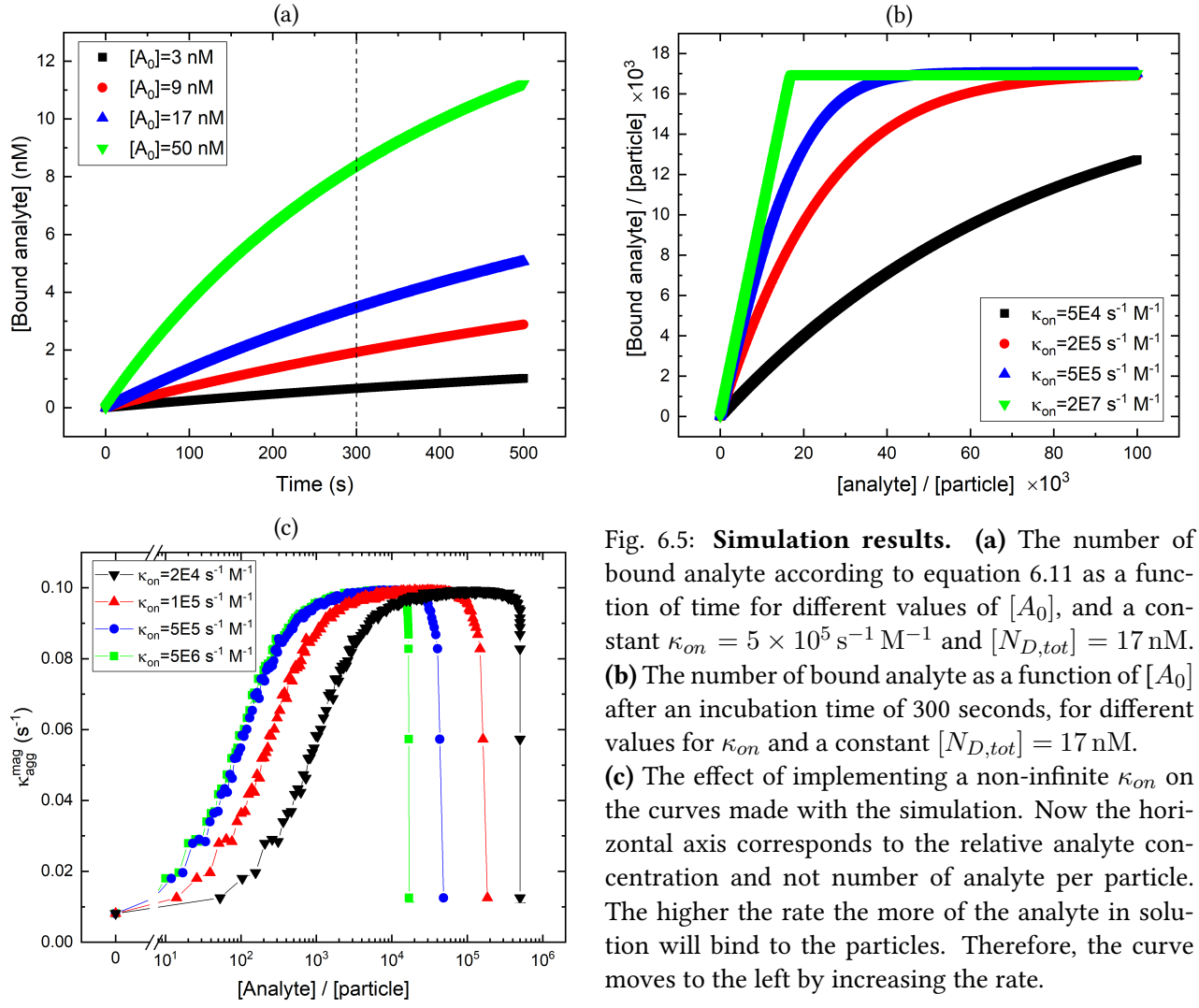

Fig. 6.5: **Simulation results.** **(a)** The number of bound analyte according to equation 6.11 as a function of time for different values of $[A_0]$, and a constant $\kappa_{on} = 5 \times 10^5\,\mathrm{s}^{-1}\,\mathrm{M}^{-1}$ and $[N_{D,tot}] = 17\,\mathrm{nM}$. **(b)** The number of bound analyte as a function of $[A_0]$ after an incubation time of 300 seconds, for different values for κ_{on} and a constant $[N_{D,tot}] = 17\,\mathrm{nM}$. **(c)** The effect of implementing a non-infinite κ_{on} on the curves made with the simulation. Now the horizontal axis corresponds to the relative analyte concentration and not number of analyte per particle. The higher the rate the more of the analyte in solution will bind to the particles. Therefore, the curve moves to the left by increasing the rate.

in time and is higher for higher initial analyte concentrations. Combining this graph with Fig. 6.4b and using an incubation time of 300 seconds result in Fig. 6.5b, which shows the concentration of bound analyte as a function of the analyte concentration for different values for κ_{on}. In case of $\kappa_{on} \to \infty$ all the analytes will bind to the docking strands up to the saturation point, where all docking strands are occupied. In case of a very low rate, almost no analyte is adsorbed by the docking strands. By changing the rate, the ratio between adsorbed and added analyte strands can be varied. So the simulated adsorption can be tuned to a realistic value.

6.2.2 Implementing k_{on} in the simulation

Initially, the simulation computes the particle aggregation rate for a specific number of analytes on the particles. Subsequently, the required analyte concentration is computed in order to get this number of analytes on a particle. Note that this deviates from the experiments, in an experiments first the analyte is incubated to the particles and subsequently the particle aggregation rate is measured.

The required analyte concentration to get a specific number of analytes on the particles depends on the adsorption rate k_{on}. The result of implementing the adsorption in the simulation is shown in Fig. 6.5c, where the κ_{agg}^{mag} is computed as a function of the analyte concentration for different adsorption rates κ_{on}. The lower the adsorption rate, the more analyte is needed to get the same number of analytes on a particle, so the curves are moved and stretched to the right (to higher concentrations) when the rate is decreased. With a rate $\kappa_{on} =$

$5 \times 10^6\,\mathrm{s}^{-1}\,\mathrm{M}^{-1}$ (or higher) all analyte that is added binds to the docking strands within the incubation time of 300 seconds (up to the saturation point, where all docking strands are occupied). So the curve corresponding to $\kappa_{on} = 5 \times 10^6\,\mathrm{s}^{-1}\,\mathrm{M}^{-1}$ is equal to the earlier simulated curve in Fig. 6.3a ($N_D = 17\,000$).

Chapter 7

Interpreting results with simulations

The simulation of specific particle aggregation that is discussed in the previous chapter is used to interpret the results of the OMC experiments of chapter 5 and is used to investigate the effect of a PEG functionalization in the DNA model system. In the first section it is explained how the measured or simulated aggregation rate should be interpreted. Thereafter the input parameters of the simulation are chosen such that the simulated magnetically induced aggregation rate κ_{agg}^{mag} is similar to the measurement results of Fig. 5.5. Subsequently, the parameters of the simulation are changed to fit the measurement results of Fig. 5.7, where the κ_{agg}^{mag} is decreased with a PEG functionalization of $30\,\mathrm{kDa}$.

7.1 Interpreting measured and simulated aggregation rate

The measured aggregation rate gives information about the amount of chemical dimers that have been formed during the actuation phase. This rate is not the same as the association rate between a single docking and a single analyte strand (the κ_{ass}^{DNA}), but the particle aggregation rate does depend on this association rate. A higher association rate results in more chemical dimers, and thus in a higher particle aggregation rate. In order to compare the association rate of the DNA molecules with the measured or simulated particle aggregation rate, the number of possible molecular bonds should be taken into account. In the simulation the total number of possible bonds of a dimer is known. This number is linearly related to the particle aggregation rate, as shown in Fig. 7.1a, where the rate and the total number of possible bonds is plotted versus the number of analyte strands per particle. The input parameters of the simulation of this figure are: a zero non-specific aggregation rate, $N_D = 4400$, $d = 12\,\mathrm{nm}$, and $\kappa_{ass}^{DNA} = 2 \times 10^{-4}\,\mathrm{s}^{-1}$.

The simulated aggregation rate divided by the number of possible bonds is approximately the same over the whole range of analyte concentration. The average value for this ratio is $1.7 \times 10^{-4}\,\mathrm{s}^{-1}$, which is close to the input parameter $\kappa_{ass}^{DNA} = 2 \times 10^{-4}\,\mathrm{s}^{-1}$. The difference can be explained with Fig. 7.1b. The obtained aggregation rate from a simulation or an experiment has a limit, which depends on the actuation time according to equation 3.3. The limit for the aggregation rate is $0.1\,\mathrm{s}^{-1}$, for the used actuation time of 20 seconds according to equation 3.3. When the particle aggregation rate approaches or exceed this limit, the obtained value for the aggregation rate deviates from the actual aggregation rate. So the computed rate deviates from the real rate, and the error becomes larger with an increasing rate. In appendix A6 an equation is derived that can be used to correct for the difference between the real and measure aggregation rate.

Fig. 7.1b shows the computed aggregation rate as a function of the real aggregation rate, also the limit at $0.1\,\mathrm{s}^{-1}$ and the linear relation are plotted. The computed rate saturated to the limit, the effect of this saturation becomes significant (error$>10\,\%$) at a real aggregation rate of about $0.025\,\mathrm{s}^{-1}$. The aggregation rate that is plotted in Fig. 7.1a is sufficiently high that the computed rate is significant lower than the real rate, which

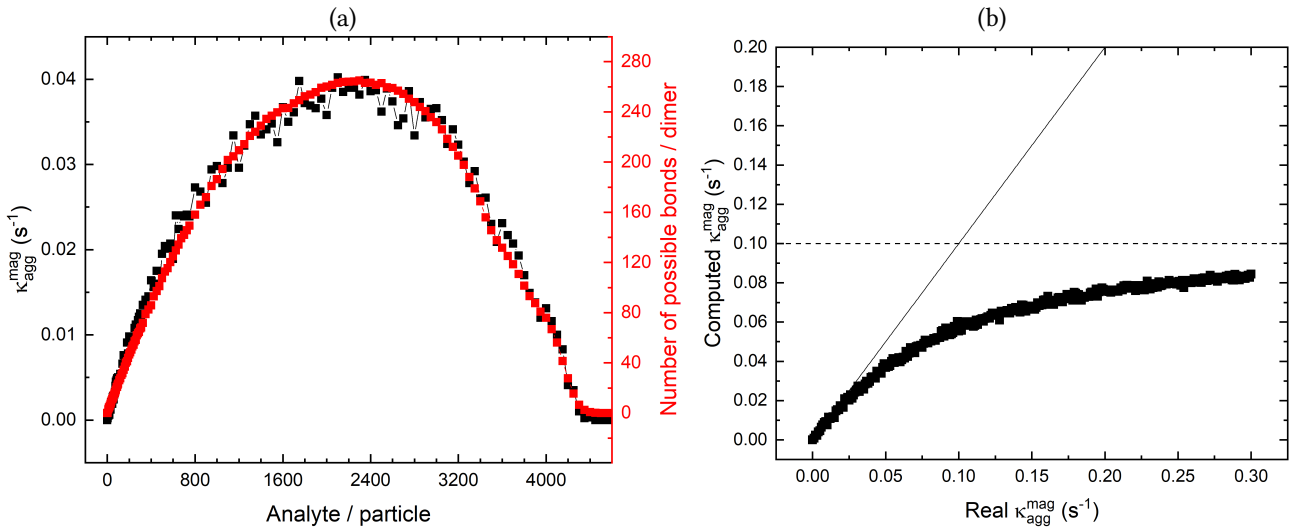

Fig. 7.1: **Interpreting simulation results (a)** The simulated particle aggregation rate versus the number of analyte per particle, simulated with the input parameters: $\kappa_{ass}^{DNA} = 2 \times 10^{-4}\,\mathrm{s}^{-1}$, $d = 12\,\mathrm{nm}$. Also the number of possible bonds per dimer between the analyte and docking strands is plotted as a function of the number analyte per particle. **(b)** The computed aggregation rate is plotted versus the real aggregation rate, which can also be used as input parameter of the simulation. In addition the limit of the aggregation rate according to equation 3.3 is plotted. The computed rate saturates to this limit. The deviation from the linear relation increases with the real aggregation rate.

explains the difference between the association rate of a single docking-analyte pair ($\kappa_{ass}^{DNA} = 2 \times 10^{-4}\,\mathrm{s}^{-1}$) and the particle aggregation rate divided by the number of possible bonds ($1.7 \times 10^{-4}\,\mathrm{s}^{-1}$).

7.2 Matching simulation to measurement

With the experiments of chapter 5 the magnetically induced aggregation rate is determined as a function of the analyte concentration for the two different functionalization densities: $(16 \pm 1)\,\%$ DNA coverage and $(62 \pm 5)\,\%$ DNA coverage. These coverages corresponds to an estimated number of dock strands of respectively $N_{D,tot} = 4400 \pm 300$ and $N_{D,tot} = 17\,000 \pm 2000$. The parameters that are changed to match the simulation to the measurement results are: the association rate of DNA molecules κ_{ass}^{DNA} (from Fig. 6.1), the inter particle distance d, and the ratio between the added analyte and the number of analyte on a particle which depends on the rate κ_{on} (from Fig. 6.4). Determining the parameters is done by varying these parameters systematically and comparing the simulation results with the measurement results.

The measurement results of the $16\,\%$ and $62\,\%$ DNA coverage samples are both shown in Fig. 7.2a. Both sets of data points reach the experimental maximum at $\kappa_{agg}^{mag} = 0.1\,\mathrm{s}^{-1}$, which indicates a large κ_{ass}^{DNA}, in the order of $10^{-3}\,\mathrm{s}^{-1}$ or lager, which can be concluded from Fig 6.2. A difference between the two curves is the analyte concentration at which the κ_{agg}^{mag} starts decreasing due to saturation of the docking strands with analyte. The $62\,\%$ DNA sample requires a higher analyte concentration to show the decrease, due to a higher number of docking strands on the particles, so more analyte is needed for saturation. Another difference between the two measurements is that the curve of the $16\,\%$ seems to be shifted to the left with respect to the curve of $62\,\%$ DNA, the κ_{agg}^{mag} increases at lower analyte concentrations. This might be the results of a higher adsorption rate κ_{on} for the $16\,\%$ DNA particles. These particles have a lower surface charge, compared to the $62\,\%$ DNA particles, so the repulsive force between the analyte strands in solution and the particles is lower.

The simulation results that match with both measurements the best are obtained with a DNA association rate $\kappa_{ass}^{DNA} = 9 \times 10^{-3}\,\mathrm{s}^{-1}$. The adsorption rate κ_{on} is different for both samples, the $16\,\%$ and $62\,\%$ DNA curves

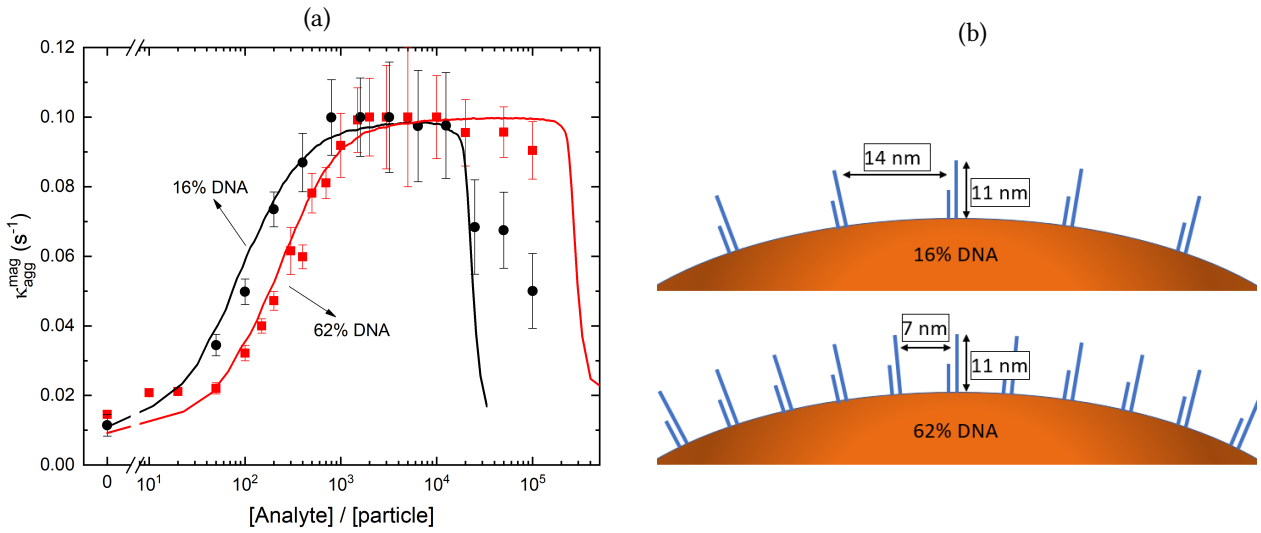

Fig. 7.2: **Difference between** 16 % **DNA coverage and** 62 % **DNA coverage: (a)** The magnetically induced aggregation rate κ_{agg}^{mag} is plotted as a function of the analyte concentration relative to particle concentration for the 16 % DNA coverage and 62 % DNA coverage. The measurement data is plotted as points, the curves are the simulation results. The input parameters for the simulation are for 16 % DNA: $\kappa_{ass}^{DNA} = 9 \times 10^{-3}\,\mathrm{s}^{-1}$, $N_D = 4400$, $\kappa_{on} = 6 \times 10^5\,\mathrm{s}^{-1}\,\mathrm{M}^{-1}$, and $d = 12\,\mathrm{nm}$. For 62 % DNA: $\kappa_{ass}^{DNA} = 9 \times 10^{-3}\,\mathrm{s}^{-1}$, $N_D = 17\,000$, $\kappa_{on} = 5 \times 10^4\,\mathrm{s}^{-1}\,\mathrm{M}^{-1}$, and $d = 20\,\mathrm{nm}$. **(b)** Schematic representation of the density of the docking strands on a particle with a 16 % and 62 % DNA coverage, showing the distance between the docking strands and the length of the docking strands.

have respectively an adsorption rate $\kappa_{on} = 6 \times 10^5\,\mathrm{s}^{-1}$ and $\kappa_{on} = 5 \times 10^4\,\mathrm{s}^{-1}$. The inter particle distance in both simulations should be different in order to match with the measurement data. The inter particle distances are respectively 12 nm and 20 nm for the 16 % and 62 % DNA samples. This larger distance might be caused by the surface charge. The sample with particles of a 62 % DNA coverage have a larger surface charge and thus a larger repulsive force. Another reason could be that the DNA strands may form a brush, a physical barrier that is between the two particle surfaces which causes a larger inter particle distance. Brush formation might happen when the distance between the DNA docking strands becomes smaller than the size of the DNA strands, which is the case for the 62 %DNA coverage, see Fig. 7.2b.

7.3 Decreasing reactivity with PEG

The last section of chapter 5 showed that the particle aggregation rate can be decreased with a functionalization of 30 kDa PEG molecules. In Fig. 7.3 the aggregation rate of particles with this functionalization is plotted versus the relative analyte concentration and compared with the aggregation rate of particles without PEG. The data corresponding to the particles with no PEG is identical in the three plots and is the same as the data in Fig. 7.2a (16 % DNA). The measurement data (the points) of the 30 kDa PEG particles in the three plots of Fig. 7.3 is identical, but the curves are different in the three plots. The different curves are the results of different input parameters in the simulation, which are discussed below. In every graph the 30 kDa PEG curve is compared to the no PEG curve, which has the input parameters: $\kappa_{ass}^{DNA} = 9 \times 10^{-3}\,\mathrm{s}^{-1}$, $\kappa_{on} = 6 \times 10^5\,\mathrm{s}^{-1}\,\mathrm{M}^{-1}$, $d = 12\,\mathrm{nm}$, and $N_D = 4400$, of which only the κ_{ass}^{DNA} and d are changed to match the 30 kDa PEG data.

First it is tested what will happen when solely the DNA association rate κ_{ass}^{DNA} is changed, while the inter particle distance d is kept constant at 12 nm. A decrease in association might be caused by the steric effect of the PEG molecules on the DNA strands. In order to match the simulation result to the measurement data of the 30 kDa PEG particles a DNA association rate κ_{ass}^{DNA} of $2 \times 10^{-4}\,\mathrm{s}^{-1}$ is used, resulting in the curve that

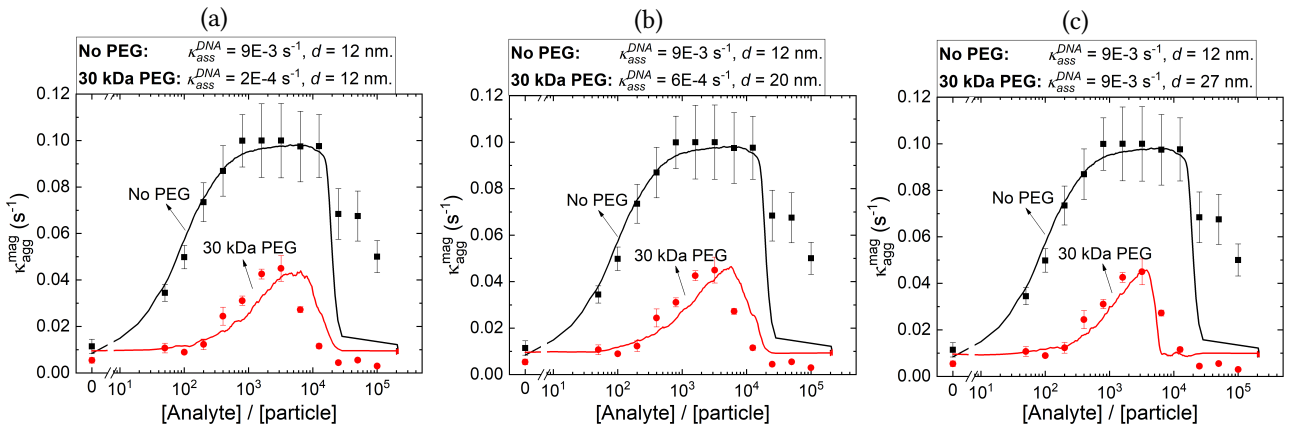

Fig. 7.3: **Comparison of the aggregation rate of particles with and without PEG:** The magnetically induced aggregation rate κ_{agg}^{mag} is plotted as a function of the analyte concentration relative to particle concentration. The measurement data, plotted as points, is identical in the three graphs. The simulation results are shown as curves. The simulation result of the No PEG samples is the same in the three plots, with input parameters: $\kappa_{ass}^{DNA} = 9 \times 10^{-3}\,\mathrm{s}^{-1}$, $N_D = 4400$, $\kappa_{on} = 6 \times 10^{5}\,\mathrm{s}^{-1}\,\mathrm{M}^{-1}$, and $d = 12\,\mathrm{nm}$. The simulated curves of the 30 kDa PEG samples are different for each graph. Only the distance d and the DNA association rate κ_{ass}^{DNA} are changed with respect to the No PEG simulation. The used input parameters for the three plots are:
(a) $\kappa_{ass}^{DNA} = 2 \times 10^{-4}\,\mathrm{s}^{-1}$ (factor 45 lower) and $d = 12\,\mathrm{nm}$ (unchanged).
(b) $\kappa_{ass}^{DNA} = 6 \times 10^{-4}\,\mathrm{s}^{-1}$ (factor 15 lower) and $d = 20\,\mathrm{nm}$ (increase of 8 nm).
(c) $\kappa_{ass}^{DNA} = 9 \times 10^{-3}\,\mathrm{s}^{-1}$ (unchanged) and $d = 27\,\mathrm{nm}$ (increase of 15 nm).

is shown in Fig. 7.3a. The association rate is a factor 45 lower than the rate that is used is the simulation for particles without PEG. It is unknown of such a large difference is realistic. The used distance of 12 nm is small compared to the Flory radius of the 30 kDa PEG molecules, which is about 17 nm. It is more likely that the PEG molecules causes a larger distance between the particles.

Fig. 7.3b shows the simulated curve of the 30 kDa PEG particles where the distance and the association rate are both changed. The used association rate $\kappa_{ass}^{DNA} = 6 \times 10^{-4}\,\mathrm{s}^{-1}$, which is a factor 15 lower than the rate that is used in the simulation for the particles without PEG. The used distance is $d = 20\,\mathrm{nm}$. The simulated curve (30 kDa PEG) is similar to the curve in Fig. 7.3a. Decreasing the association rate has a similar effect on the aggregation as increasing the distance. The used combination of distance and association rate is an example of the many possible combinations, for (almost) every distance between the 12 and 30 nm, which is the length of the docking-analyte-docking complex, a rate can be chosen such that the simulation result matches the data points.

It is also possible to match the simulation results to the measurement data by solely changing the distance d in the simulation and using the same association rate ($\kappa_{ass}^{DNA} = 9 \times 10^{-3}\,\mathrm{s}^{-1}$) for the 30 kDa PEG as for the No PEG sample. In this case a distance $d = 27\,\mathrm{nm}$ should be used in the simulation in order to match the measurement data. This distance seems plausible considering the Flory diameter of the PEG molecules which is about 35 nm and taking into account that the PEG molecule can be squeezed a bit. The result of this simulation is plotted in Fig. 7.3c.

Changing the inter particle distance d and the DNA association rate κ_{ass}^{DNA} gives similar results in the simulations. The effect of both changes could not be distinguished with the simulation. Further research is required to find out if the decrease in particle aggregation is caused by a larger distance or a decrease in the association.

Chapter 8

Conclusion and outlook

In this project specific particle aggregation rates are measured with a DNA sandwich model system using the optomagnetic cluster (OMC) experiment. Three different kind of particles were tested on magnetic and non-magnetic properties to select the most suitable particle for the OMC experiments. The Ademtech Masterbeads, Polystyrene microparticle (GmbH) and Silica microparticle (GmbH) all have similar magnetic properties, but the Silica microparticles are selected due to the small size dispersion (CV$<5\,\%$) and the smooth particle surface.

It is demonstrated that it is possible to distinguish the non-specific from the specific aggregation rate. The non-specific interaction between the particles was reduced with a DNA functionalization, and a BSA-casein coating. The non-specific magnetically induced aggregation rate was reduced to $(6 \pm 3) \times 10^{-3}\,\mathrm{s}^{-1}$. The maximum aggregation rate that could be measured is $1 \times 10^{-1}\,\mathrm{s}^{-1}$, which gives a dynamic range of over one order of magnitude for measuring the specific aggregation rate. The specific interaction is induced by analyte strands that can bind to the docking strands which are functionalized on the particles. A chemical dimer is formed when the analyte is sandwiched between two docking strands of two particles. The particle aggregation rate was measured as a function of the analyte concentration as shown in Fig. 5.5. The specific interaction is characterized by first an increase in the aggregation rate with the analyte concentration, and subsequently a decreases at higher concentrations due to saturation of the docking strands on the particles by analyte strands.

The magnetically induced specific aggregation rate has been decreased with a $30\,\mathrm{kDa}$ PEG functionalization. Using a simulation, it was demonstrated that this reduction is most likely caused by a combination of a decrease in chemical association rate between the analyte and docking strands and an increases of the inter particle distance.

The used DNA sandwich assay is a relative easy system that gives reproducible results when it is used to measure specific particle aggregation rates. It was demonstrated that the particle aggregation rate can be reduced using a PEG functionalization for particles that interact via a DNA sandwich assay. Tuning the aggregation rate with a PEG functionalization should also be tested for other specific interactions, for example an Ab-Ab interaction.

In order to use the PEG functionalization as a way to tune the affinity in a BPM system several things should be investigated. In further research it should be investigated if the decrease in aggregation rate that is measured here for particle-particle interactions also hold for particle-surface geometry. It should also be investigated if a lower aggregation rate also result in a higher dissociation rate, possibly due to a smaller probability of forming multivalent bonds, or due to a lower probability for rebinding. Only when the dissociation rate is affected by the PEG molecules it would be possible to tune the actual affinity of the specific interaction for use in a BPM system.

Bibliography

[1] P. Yager, G. J. Domingo, and J. Gerdes, "Point-of-care diagnostics for global health," *Annual Review of Biomedical Engineering*, vol. 10, no. 1, pp. 107–144, 2008.

[2] A. Kaushik and M. A. Mujawar, "Point of care sensing devices: Better care for everyone," *Sensors*, vol. 18, no. 12, p. 4303, 2018.

[3] V. Gubala, L. F. Harris, A. J. Ricco, M. X. Tan, , and D. E. Williams, "Point of care diagnostics: Status and future," *Anal. Chem.*, vol. 84, no. 2, pp. 487–515, 2012.

[4] imageS. Vigneshvar, C. C. Sudhakumari, B. Senthilkumaran, and H. Prakash, "Recent advances in biosensor technology for potential applications - an overview," *Front. Bioeng. Biotechnol*, vol. 4, no. 11, 2016.

[5] K. Rogers, "Principles of affinity-based biosensors," *Molecular Biotechnology*, vol. 14, no. 2, pp. 109–129, 2000.

[6] G. Dhawan, G. Sumana, and B. Malhotra, "Recent developments in urea biosensors," *Biochemical Engineering Journal*, vol. 44, no. 1, pp. 42–52, 2009.

[7] K. van Ommering, P. A. Somers, M. Koets, J. J. H. B. Schleipen, L. J. van IJzendoorn, and M. W. J. Prins, "Mobility and height detection of particle labels in an optical evanescent wave biosensor with singlelabel resolution," *J. Phys. D: Appl. Phys*, vol. 43, no. 155501, 2010.

[8] N. K. A. G. E. Fryxell, , and M. Zhang, "A bifunctional poly(ethylene glycol) silane immobilized on metallic oxide-based nanoparticles for conjugation with cell targeting agents," *J. Am. Chem. Soc.*, vol. 126, pp. 7206–7211, 2004.

[9] A. Ranzoni, J. J. H. B. Schleipen, L. J. van IJzendoorn, and M. W. J. Prins, "Frequency-selective rotation of two-particle nanoactuators for rapid and sensitive detection of biomolecules," *Nano Letters*, vol. 11, no. 2, pp. 2017–2022, 2011.

[10] A. Romijn, "Quantification of particle aggregation rates for non-specific interactions," *Master Thesis TU/e*, 2018.

[11] V. M. Nekrasov, A. A. Polshchitsin, M. A. Yurkin, G. E. Yakovleva, V. P. Maltsev, and A. V. Chernyshev, "Brownian aggregation rate of colloid particles with several active sites," *J. Chem. Phys.*, vol. 141, no. 064309, 2014.

[12] P. Biancaniello and J. Crocker, "Line optical tweezers instrument for measuring nanoscale interactions and kinetics," *Rev. Sci. Instrum*, vol. 77, no. 113702, 2006.

[13] Z. Wang, C. He, X. Gong, J. Wang, and T. Ngai, "Measuring the surface-surface interactions induced by serum proteins in a physiological environment," *Langmuir*, vol. 32, no. 46, pp. 12129–12136, 2016.

[14] M. I. Shliomis, "Magnetic fluids," *Sov. Phys. Usp.*, vol. 17, no. 153, 1974.

[15] K. W. YUNG, pETER B. LANDECKER, and D. D. VILLANI, "An analytic solution for the force between two magnetic dipoles," *Magnetic and Electrical Separation*, vol. 9, pp. 39–52, 1998.

[16] M. Scheepers, A. Romijn, L. van IJzendoorn, and M. Prins, "Rate of dimer formation in a stable colloidal solution quantified using an attractive interparticle force," *TU/e*, 2019.

[17] M. Marolt, "Superparamagnetic materials," *University of Ljubljana Faculty of Mathematics and Physics*, 2014.

[18] J.-C. BACRI, R. PERZYNSKI, D. S. V. CABUIL, and R. MASSART, "Magnetic colloidal properties of ionic ferrofluids," *J. Magnetism and Magnetic Materials*, vol. 62, pp. 36–46, 1986.

[19] A. Ranzoni, X. J. A. Janssen, M. Ovsyanko, L. J. van IJzendoorn, and M. W. J. Prins, "Magnetically controlled rotation and torque of uniaxial microactuators for lab-on-a-chip applications," *Lab on a chip*, vol. 10, no. 2, pp. 179–188, 2010.

[20] K. J. Laidler and J. H. Meiser, *Physical chemistry.* Menlo Park, Calif. Benjamin/Cummings Pub. Co., 1982.

[21] B. Alberts, A. Johnson, J. Lewis, M. Raff, K. Roberts, and P. Walter, *Molecular Biology of the Cell (6th ed.).* Garland Science, 2014.

[22] M. P. Ball, "Chemical structure of dna." `https://en.wikipedia.org/wiki/Directionality_(molecular_biology)#/media/File:DNA_chemical_structure.svg`. 2018.

[23] E. Visser, *Biosensing based on tethered particle motion.* 2017.

[24] S. Ikuta, K. Takagi, R. B. Wallace, and K. Itakura, "Dissociation kinetics of 19 base paired oligonucleotide-dna duplexes containing different single mismatched base pairs," *Nucleic Acids Research*, vol. 15, no. 2, pp. 797–811, 1987.

[25] M. Murphy, I. Rasnik, W. Cheng, T. M. Lohman, and T. Ha, "Probing single-stranded dna conformational flexibility using fluorescence spectroscopy," *Elsevier*, vol. 86, no. 4, pp. 2530–2537, 2004.

[26] G. S. Manning, "The persistence length of dna is reached from the persistence length of its null isomer through an internal electrostatic stretching force," *Elesevier*, vol. 91, no. 10, pp. 3607–3616., 2006.

[27] T. Drobek, N. D. Spencer, and M. Heuberger, "Compressing peg brushes," *Macromolecules*, vol. 38, pp. 5254–5259, 2005.

[28] B. Hua, K. Y. Han, R. Zhou, H. Kim, X. Shi, S. C. Abeysirigunawardena, A. Jain, D. Singh, V. Aggarwal, S. A. Woodson, and T. Ha, "An improved surface passivation method for single-molecule studies," *Nature Methods*, vol. 11, pp. 1233–1236, 2014.

[29] "Integrated dna technologies." `https://eu.idtdna.com/pages`.

[30] "Thermo fisher scientific." `https://www.thermofisher.com/order/catalog/product/S11494`. product num. S11494.

[31] S. P. Lina, C. Y. Panc, K. C. Tseng, M. C. Lind, C. D. Chend, C. C. Tsai, S. H. Yua, Y. C. Sung, T. W. Lina, and Y. T. Chena, "A reversible surface functionalized nanowire transistor to study protein-protein interactions," *Nature today*, vol. 4, no. 3, pp. 235–243, 2009.

[32] A. Ranzoni, G. Sabatte, L. J. van IJzendoorn, and M. W. J. Prins, "Frequency-selective rotation of two-particle nanoactuators for rapid and sensitive detection of biomolecules," *Nano Letters*, vol. 6, no. 4, pp. 3134–3141, 2012.

[33] B. D. Cullity, *Introduction to Magnetic Materials.* Addison-Wesley: Cambridge, 1972.

[34] C. Derang, L. Hao, P. Lining, L. Jianan, W. Xicheng, J. Panpan, C. Xiaohong, W. Wenjie, W. Jianbo, and L. Qingfang, "High saturation magnetization of y-fe2o3 nano-particles by a facile one-step synthesis approach," *Nature, Scientific Reports*, vol. 6, no. 32360, 2016.

[35] A. Abragam, *The Principles of Nuclear Magnetism.* Oxford University Press, 2016.

[36] D. Mackowski, "A general superposition solution for electromagnetic scattering by multiple spherical domains of optically active media," *J. Quant. Spectrosc. Ra*, vol. 133, pp. 264–270, 2014.

[37] N. M. Green, "Advances in protein chemistry," *ScienceDirect*, vol. 29, no. 1975, pp. 85–133, 1975.

[38] D. Y. Zhang, A. J. Turberfield, B. Yurke, and E. Winfree1, "Engineering entropy-driven reactions and networks catalyzed by dna," *Science*, vol. 318, no. 5853, pp. 1121–1125, 2007.

[39] R. I. Ovseenko and Y. G. Ovseenko, "Drag of a rotating sphere," *Izv. AN SSSR. Mekhanika Zhidkosti i Gaza*, vol. 3, no. 1, pp. 110–118, 1968.

[40] R. Vliembergen, *Optical scattering of rotating dimers for biosensing applications.* 2018.

[41] "Sds of iron(iii) oxide," KJLC. England: Kurt J Lesker Company Ltd. 2012-01-05. Retrieved 2014-07-12.

[42] M. R. Querry, *Optical constants.* University of Missouri, 1985. `http://www.dtic.mil/docs/citations/ADA158623`.

[43] Dr. Harald Fiedler, Product Manager microParticles GmbH.

[44] X. Ma, J. Q. Lu, R. S. Brock, K. M. Jacobs, P. Yang, , and X.-H. Hu, "Determination of complex refractive index of polystyrene microspheres from 370 to 1610 nm," *Phys. Med. Biol.*, vol. 48, no. 24, pp. 4165–4172, 2003.

[45] B. N. Khlebtsov, V. A. Khanadeev, and N. G. Khlebtsov, "Spectroturbidimetric determination of the size, concentration, and refractive index of silica nanoparticles," *Optics and Spectroscopy*, vol. 105, no. 5, pp. 732–738, 2008.

Appendix

A1 Derivation of rotational torque

In order to determine the torque on a rotating sphere in a fluid, the Stokes equations need to be solved, which are

$$\begin{aligned} \nabla \cdot \vec{v} &= 0 \\ \nabla p &= \eta \Delta \vec{v}, \end{aligned} \tag{1}$$

in which $\vec{v}$ is the flow velocity of the fluid, p is the pressure and η is the viscosity. The flow is around the rotation axis, this direction is defined as the ϕ-direction ($\hat{\boldsymbol{\phi}}$), the flow is rotational symmetric and does not depends on ϕ. At the surface of the sphere the flow has the same velocity as the surface, due to the no-shear condition. The surface velocity depends on the angular frequency ω and the distance perpendicular to the rotation axis, which is defined as $\rho = R\sin(\theta)$, with R the radius of the sphere and θ is the azimuthal angle. At an infinite distance from the sphere the flow should be zero, as well as the pressure in the fluid due to the flow. So the boundary conditions are

$$\vec{v}|_{r=R} = \omega R \sin(\theta)\hat{\phi}, \quad \vec{v}|_{r\to\infty} = 0, \quad p|_{r\to\infty} = 0. \tag{2}$$

The flow is in the ϕ-direction and depends on the coordinates r and θ. With the help of the first boundary condition, $\vec{v}$ can be redefined as the product of $\omega r\sin(\theta)$ and a function that depends solely on r, with r the distance to the center of the sphere:

$$\vec{v} \equiv \omega r \sin(\theta) Y(r) \hat{\boldsymbol{\phi}}. \tag{3}$$

With this definition, the first Stokes equation is automatically met. For the second Stokes equation, the Laplacian of $\vec{v}$ should be calculated, which is defined as

$$\Delta \vec{v} = \nabla(\nabla \cdot \vec{v}) - \nabla \times (\nabla \times \vec{v}). \tag{4}$$

Here, the first term is zero, because this term contains the first Stokes equation. For the calculation of second part, it is useful to determine the term in brackets firstly. The curl of the flow velocity is given by

$$\begin{aligned} \nabla \times \vec{v} = \frac{1}{r\sin(\theta)} \frac{\partial(\sin(\theta)v_\phi)}{\partial\theta}\hat{r} - \frac{1}{r}\frac{\partial(rv_\phi)}{\partial r}\hat{\theta} = \frac{\omega}{r\sin(\theta)}\left[2r\cos(\theta)\sin(\theta)Y(r)\right]\hat{r} \\ -\frac{\omega\sin(\theta)}{r}\left[2rY(r) + r^2Y'(r)\right]\hat{\theta} \end{aligned} \tag{5}$$

where the prime corresponds to the derivative. Taking the curl of equation (5) results in

$$\begin{aligned} \nabla \times (\nabla \times \vec{v}) &= -\frac{\omega\sin(\theta)}{r}\frac{\partial}{\partial r}\left[2rY(r) + r^2Y'(r)\right]\hat{\phi} - \frac{\omega}{r}\frac{\partial}{\partial\theta}\left[2\cos(\theta)Y(r)\right]\hat{\phi}, \\ &= -\frac{\omega\sin(\theta)}{r}\left[2Y(r) + 2rY'(r) + 2rY'(r) + r^2Y''(r)\right]\hat{\phi} + \frac{\omega}{r}2\sin(\theta)Y(r)\hat{\phi}, \\ &= -\omega\sin(\theta)\left[4Y'(r) + rY''(r)\right]\hat{\phi}. \end{aligned} \tag{6}$$

Multiplying this equation by $-\eta$ should results in a function that is equal to the gradient of the gradient of the pressure, which is given by

$$\nabla p = \frac{\partial p}{\partial r}\hat{r} + \frac{1}{r}\frac{\partial p}{\partial \theta}\hat{\theta} + \frac{1}{\sin(\theta)}\frac{\partial p}{\partial \phi}\hat{\phi}. \tag{7}$$

$\Delta\vec{v}$ has only a component in the ϕ-direction and thus, according to equation 1, the gradient of the pressure should have as well only a ϕ-component. Therefore the first two terms of the right hand side of equation 7 are zero. Due to the rotational symmetry of the flow, the flow and also the pressure does not depend on ϕ. Thus the derivative of the pressure to ϕ is zero. All the terms in equation 7 are zero, as well as the Laplacian of $\vec{v}$. This conclusion can be used to get an expression for function $Y(r)$, by equalizing equation 6 to zero.

$$4Y'(r) = -rY''(r) \tag{8}$$

In order to solve this equation, $Y(r)$ is defined as r^λ, which gives

$$\begin{aligned} 4\lambda r^{\lambda-1} &= -r\lambda(\lambda-1)r^{\lambda-2}, \\ 4\lambda r^{\lambda-1} &= -\lambda(\lambda-1)r^{\lambda-1}, \\ 4\lambda &= -\lambda(\lambda-1). \end{aligned} \tag{9}$$

This equation has the solutions $\lambda = -3$ and $\lambda = 0$, which results in a function of the flow

$$\vec{v} = \omega r\sin(\theta)\frac{A}{r^3} + B, \tag{10}$$

where A and B are constants. With the boundary condition of equation(2), it can be concluded that $B = 0$ and $A = R^3$, which leads to the final equation for the flow velocity

$$\vec{v} = \omega r\sin(\theta)\frac{R^3}{r^3}\hat{\phi} \tag{11}$$

From this velocity distribution, the stress and finally the torque can be calculated. The stress tensor is given by

$$\sigma = -pI + \eta(\nabla\vec{v} + \nabla\vec{v}^T), \tag{12}$$

in which p is the pressure, I is the unity matrix and superscript T means the transposed matrix. It is concluded above that the pressure is zero, which simplifies the stress tensor. The force, that is the dot-product of the stress tensor with the normal of the surface, is given by

$$\mathrm{d}F = \begin{pmatrix} \sigma_{rr} & \sigma_{r\theta} & \sigma_{r\phi} \\ \sigma_{\theta r} & \sigma_{\theta\theta} & \sigma_{\theta\phi} \\ \sigma_{\phi r} & \sigma_{\phi\theta} & \sigma_{\phi\phi} \end{pmatrix} \cdot \begin{pmatrix} \mathrm{d}A \\ 0 \\ 0 \end{pmatrix} \tag{13}$$

The stress tensor components that are not multiplied with zero are $\sigma_{rr}, \sigma_{r\theta}$ and $\sigma_{r\phi}$. The first two are zero because the velocity has no components in the r- and θ-direction. $\sigma_{r\phi}$ can be determined with the gradient of the velocity and is given by [39]

$$\sigma_{r\phi} = r\frac{\partial}{\partial r}\left(\frac{v}{r}\right) = -3\omega\eta\sin(\theta)\frac{R^3}{r^3} \tag{14}$$

Filling in equation (13) in equation (12) results in a force

$$\mathrm{d}F = -3\omega\eta\sin(\theta)\frac{R^3}{r^3}\mathrm{d}A\hat{\phi} \tag{15}$$

Taking the cross product with the force and integrating over the surface of the sphere results in the total torque

$$\tau_{rot} = \int_S r\hat{r}\times\mathrm{d}F\hat{\phi} = \int_S -r3\omega\eta\sin(\theta)\frac{R^3}{r^3}(\hat{r}\times\hat{\phi})\mathrm{d}A\Big|_{r=R} \tag{16}$$

$$\tau_{rot} = 2\pi R^2\int_0^\pi -R\sin(\theta)3\omega\eta\sin(\theta)\sin(\theta)\hat{z}\mathrm{d}\theta = -8\pi\omega\eta R^3\hat{z} \tag{17}$$

A2 Derivation of the volume fraction iron-oxide

The weight fraction iron-oxide in a magnetic particle is determined in chapter 3. For the calculation of the refractive index, not the weight but the volume fraction is used. Here the equation for the volume fraction iron-oxide is derived. Lets start with the definition of the volume fraction, which is

$$f_{FeO} = \frac{V_{FeO}}{V}, \tag{18}$$

Where V is the volume and the subscript *FeO* stands for iron-oxide. The following equation holds for the volume iron-oxide

$$V_{FeO}\rho_{FeO} = f_{FeO}^{weight} m, \tag{19}$$

in which ρ_{FeO} is the mass density, f_{FeO}^{weight} is the weight fraction, and m is the total mass of a particle. The total mass can be written as the product of the volume and the density. In the case that a particle consists of iron-oxide and a surrounding medium, the mass is given by

$$m = V_{FeO}\rho_{FeO} + V_{med}\rho_{med} \tag{20}$$

where the subscript *med* stands for the medium. Combining equation 19 and 20, and writing the volume of the medium as the total volume minus the volume iron-oxide results in

$$\begin{aligned} V_{FeO}\rho_{FeO} =& f_{FeO}^{weight}\left[V_{FeO}\rho_{FeO} + (V - V_{FeO})\rho_{med}\right] \\ =& f_{FeO}^{weight} V_{FeO}\rho_{FeO} + f_{FeO}^{weight} V\rho_{med} - f_{FeO}^{weight} V_{FeO}\rho_{FeO}. \end{aligned} \tag{21}$$

This can be rewritten to

$$\begin{aligned} V_{FeO}\rho_{FeO} - f_{FeO}^{weight} V_{FeO}\rho_{FeO} + f_{FeO}^{weight} V_{FeO}\rho_{med} &= f_{FeO}^{weight} V\rho_{med} \\ V_{FeO}\left(\rho_{FeO} - f_{FeO}^{weight}\rho_{FeO} + f_{FeO}^{weight}\rho_{med}\right) &= f_{FeO}^{weight} V\rho_{med} \end{aligned} \tag{22}$$

which is the same as

$$\begin{aligned} V_{FeO} =& \frac{f_{FeO}^{weight} V\rho_{med}}{\rho_{FeO} - f_{FeO}^{weight}\rho_{FeO} + f_{FeO}^{weight}\rho_{med}} \\ =& \frac{f_{FeO}^{weight} V\rho_{med}}{\rho_{FeO} + f_{FeO}^{weight}(\rho_{med} - \rho_{FeO})} \end{aligned} \tag{23}$$

Dividing this by the total volume gives the final equation for the volume fraction iron-oxide

$$f_{FeO} = \frac{f_{FeO}^{weight}\rho_{med}}{\rho_{FeO} + f_{FeO}^{weight}(\rho_{med} - \rho_{FeO})} \tag{24}$$

A3 Viscous torque of inhomogeneous dimer

A rotating dimer of a large particle with radius R_1 and a small one with radius R_2 rotates around its center of mass. The distance between the center of mass and the middle point of both particles (x_1 and x_2) is given by

$$x_1 = M_2\frac{R_1 + R_2}{M_1 + M_2}, \qquad x_2 = M_1\frac{R_1 + R_2}{M_1 + M_2} \tag{25}$$

in which M_1 and M_2 are the masses of both particles that are given by

$$M_i = 4/3\pi R_i^3\rho, \tag{26}$$

where ρ is the mass density. Filling in this equation in equation 25 gives

$$x_1 = \frac{R_2^3}{R_1^2 - R_1R_2 + R_2^2}, \qquad x_2 = \frac{R_1^3}{R_1^2 - R_1R_2 + R_2^2} \tag{27}$$

x_1 and x_2 corresponds to the radii of the circular movement of the two particles. The torque due to the drag force that is induced by this movement is equal to the drag force (Stokes law) times the radius of the movement which is given by

$$\tau_{d,i} = x_i v 6\pi\eta R_i = 6\pi\omega\eta x_i^2 R_i \tag{28}$$

for particle $i = 1, 2$. The torque τ_r that is induced by the rotation around the central axis of the particle is not changed and given by

$$\tau_{r,i} = 8\pi\omega\eta R_i^3. \tag{29}$$

The total torque is the summation of $\tau_{d,i}$ and $\tau_{r,i}$ for both particles which is

$$\tau_v = 6\pi\omega\eta x_1^2 R_1 + 6\pi\omega\eta x_2^2 R_2 + 8\pi\omega\eta R_1^3 + 8\pi\omega\eta R_2^3 \tag{30}$$

This derivation is done for dimers of an equal volume V_{tot} so R_1 can be expressed as a function of R_2 which is

$$R_1 = \left(\frac{V_{tot}}{4/3\pi} - R_2^3\right)^{1/3} \tag{31}$$

Using this equation to calculate the total viscous torque τ_v gives

$$\tau_v = 6\pi\omega\eta x_1^2 \left(\frac{V_{tot}}{4/3\pi} - R_2^3\right)^{1/3} + 6\pi\omega\eta x_2^2 R_2 + 8\pi\omega\eta \frac{V_{tot}}{4/3\pi} \tag{32}$$

The torque has the constant term: $8\pi\omega\eta\frac{V_{tot}}{4/3\pi}$, so the viscous torque does not go to zero. The viscous torque is plotted in Fig. 4.4 as a function of the ratio between the two radii of both particles.

A4 Validation for no inertia in simulation

The movement of the particles can be determined with a differential equation that is given by

$$\frac{\partial v}{\partial t} = \frac{F_{mag} - F_{drag}}{M}, \tag{33}$$

where a is the acceleration, F_{mag} and F_{drag} are respectively the magnetic and drag force and M is the mass of the particle. An one dimensional model is made in MATLAB to solve this equation numerically. Two particles of $500\,\mathrm{nm}$ in diameter, a mass of $1.3 \times 10^{-16}\,\mathrm{kg}$, and with a magnetic moment of $0.5\,\mathrm{fA\,m^2}$ are initially on a distance of 3 micron from each other. The attractive magnetic force is given by

$$F_{mag} = 3m^2 \frac{\mu_0}{2\pi} \frac{1}{d^4} = \frac{\xi}{d^4} M \tag{34}$$

where m is the moment and d the distance between the particles, $\xi = \frac{3m^2\mu_0}{2\pi M}$ is a constant and implemented to simplify the derivation. Because of the symmetricity, the force on both particles is equal. The drag force is given by

$$F_{drag} = 6\pi\eta R v = \gamma v M \tag{35}$$

in which R is the radius of the particle, η is the viscosity and v is the velocity, $\gamma = \frac{6\pi\eta R}{M}$ is a constant and also implemented to simplify the derivation. Filling in equation 33 with the two above expressions gives

$$\frac{\partial v}{\partial t} = \frac{\xi}{d^4} - \gamma v \tag{36}$$

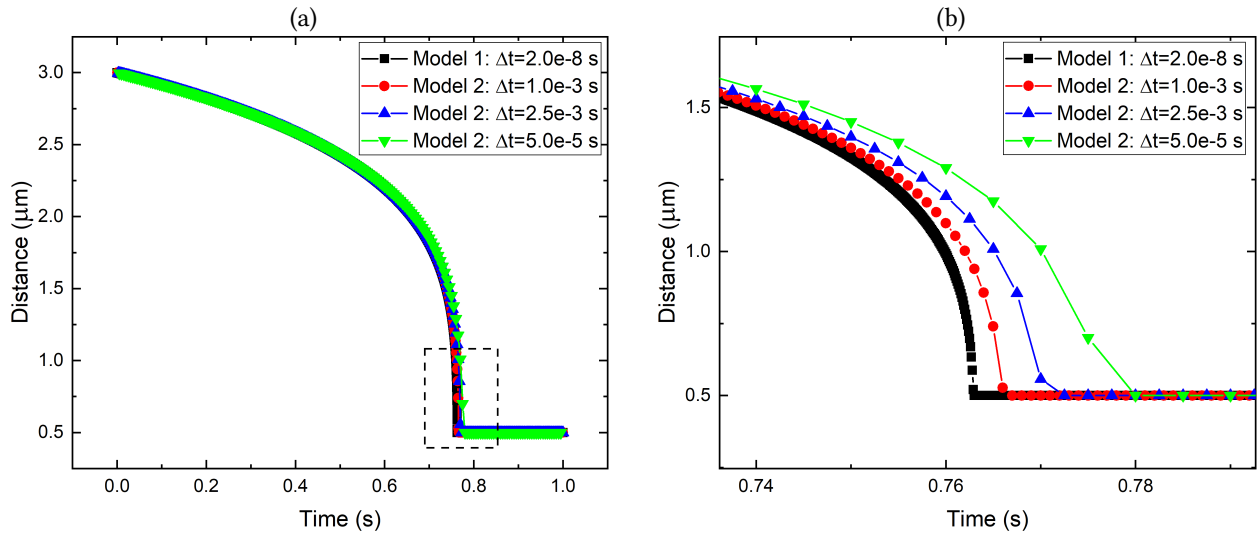

Fig. A.1: **(a)** The distance between two magnetic particles as a function of time according to Model 1 and 2. Model 1 with time steps of $\Delta t = 2 \times 10^{-8}\,\mathrm{s}$ is the most accurate model. Model 2 which uses larger time steps gives small error compared to Model 1. **(b)** A zoom in at the time where the two particles hit each other, to visualize the error better.

which can be rewritten to the numerical form:

$$\begin{aligned} v_{i+1} &= v_i + \left(\frac{\xi}{d_i^4} - \gamma v_i \right) \Delta t \\ d_{i+1} &= d_i + v_i \Delta t \end{aligned} \tag{37}$$

This set of equation is called *Model 1*. Model 1 solves equation 33 correctly when $\Delta t < 2 \times 10^{-8}\,\mathrm{s}$. The result is shown in Fig. A.1, where the distance between the particles is plotted against the time. A time step of $2 \times 10^{-8}\,\mathrm{s}$ is too small to simulate an experiments that takes 20 seconds. Therefore another model, with a larger time step, should be used to compute the dynamics of the particles.

The velocity of a particle that experience a constant magnetic force is given by

$$v = \frac{F_{mag}}{\gamma M} \left[1 - \exp\left(\gamma t\right) \right] \tag{38}$$

γ has a value of $3.6 \times 10^{7}\,\mathrm{s}^{-1}$. This means that the velocity of the particle saturates after about $1 \times 10^{-7}\,\mathrm{s}$. This happens so fast that it can be assumed that the velocity is immediately at his saturation value, which is $F_{mag}/(6\pi\eta R)$. With this assumption the following set of equations are used in for Model 2.

$$\begin{aligned} v_{i+1} &= \frac{\xi}{d_i^4} \frac{1}{6\pi\eta R} \\ d_{i+1} &= d_i + v_i \Delta t \end{aligned} \tag{39}$$

The results of Model 2 are also shown in Fig. A.1, for different time steps. According to Model 2, the computed time it takes for the particles to hit each other increases with the time step, so the error become larger with larger time steps. But the error is only less than $1\,\%$ at time steps of $2.5 \times 10^{-3}\,\mathrm{s}$. With Model 2 time steps can be used that are 1×10^{4} times larger than in Model 1, which makes a simulation based on Model 2 much faster. The simulation of chapter 4 uses time steps of $5 \times 10^{-4}\,\mathrm{s}$ which leads to an error that is smaller than $0.2\,\%$ compared to Model 1.

A5 Derivation of x_{int} of the simulation from chapter 6

The geometry of an analyte on a dimer is showed in Fig. A.2a. The dimer consists of two particle P_1 and P_2. An analyte is attached to particle P_2 and can bind to docking strands on P_1 that are within the range of the docking-analyte-docking complex, which is for the used DNA system $l_{DNA} = 30\,\mathrm{nm}$. The size of the binding area, that contains all the available free docking strands for the analyte strand, is assumed to be a circle with a diameter $x_{int} = x_1 + x_2$. x_1 can be calculated using the cosine rule with the triangle (x_1, l_{DNA}, r) and angle α_1, in the same way x_2 can be calculated with triangle (x_2, l_{DNA}, r) and angle α_2. x_1 and x_2 are given by

$$\begin{aligned} x_1 &= \sqrt{l_{DNA}^2 - r^2 + 2\,l_{DNA}\,r\cos(\alpha_1)} \\ x_2 &= \sqrt{l_{DNA}^2 - r^2 + 2\,l_{DNA}\,r\cos(\alpha_2)} \end{aligned} \tag{40}$$

r is the distance between the surfaces of the particle in the y-direction at the location of the analyte and is given by

$$r = d + 2a = d + 2\left(R - R\cos(\phi)\right), \tag{41}$$

in which R is the radius of the particles and angle ϕ corresponds to the position of the analyte. The angels α_1 and α_2 depends on the angle ϕ and are given by

$$\begin{aligned} \alpha_1 &= \frac{\pi}{2} - \phi \\ \alpha_2 &= \frac{\pi}{2} + \phi \end{aligned} \tag{42}$$

The binding area can be calculated with

$$A = \pi\left(\frac{x_1 + x_2}{2}\right)^2 \tag{43}$$

The area size is plotted in Fig. A.2b as a function of the angle ϕ and the inter particle distance d. When the distance is larger than the length of the DNA complex (30 nm) the binding area is zero because the distance is too large.

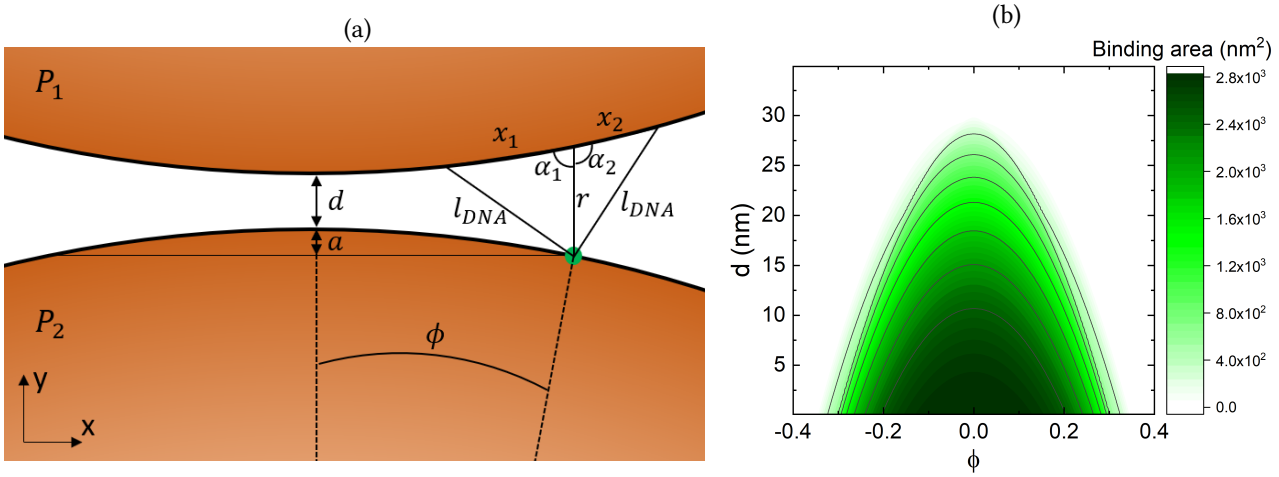

Fig. A.2: **Geometry of the simulation (a)** Two particles of a dimer have a particle to particle distance d. The location of the analyte is defined by the angle ϕ. The distance between the y-position of the analyte and the top of particle P_1 is given by a. The analyte can bind to docking strands that are within a range of l_{DNA}, which is the length of the docking-analyte-docking strand complex. The size of the area with all the available docking strands is assumed to be a circle with diameter $x_1 + x_2$. x_1 and x_2 can be calculated with the cosine rule using l_{DNA}, distance $r = d + 2a$ and angles α_1 or α_2. **(b)** The binding area as a function of the angle ϕ and the inter particle distance d.

A6 Derivation of the real rate from the measured rate

The aggregation rate that is determined with a measurement is computed with

$$\kappa_{agg}^{meas} = \frac{\Delta N_{chem}}{\Delta N_{mag}} \frac{1}{t_{act}/2}. \tag{44}$$

This deviates from the real aggregation rate if the inverse of the aggregation rate and the actuation time are in the same order of magnitude, as explained in section 7.1. Below an equation is derived that can be used for the correction of the measured aggregation rate.

The probability that magnetic dimer i becomes a chemical dimer is given by

$$P_i = 1 - (1 - \kappa_{agg}^{real} \Delta t)^{(t_{act} - t_{form,i})/\Delta t} \tag{45}$$

where $\kappa_{agg}^{real} \Delta t$ is the probability that the dimer becomes a chemical dimer in a small time step Δt, κ_{agg}^{real} is the real aggregation rate in s^{-1}, the time step Δt is required for this calculation to make equation 45 dimensionless and is chosen such that $\kappa_{agg}^{real} \Delta t \ll 1$, in this limit the probability P_i does not depend on the time step Δt. In equation 45, t_{act} is the actuation time and $t_{form,i}$ is the time at which the magnetic dimer i is formed. The probability to form a chemical dimer depends on $t_{form,i}$, the larger the time of formation the lower the probability. Each magnetic dimer that is formed during the actuation phase has its own time of formation. Under the assumption of a constant dimer formation rate κ_{form}, the number of magnetic dimers that are form increases with time. The total number of dimers at the end of the actuation is given by

$$\Delta N_{mag} = \kappa_{form} t_{act} \tag{46}$$

The time of formation of dimer i is given by

$$t_{form,i} = i/\kappa_{form} \tag{47}$$

The number of chemical dimers that are formed during the actuation phase, in the limit $\Delta N_{mag} \gg 1$, can be calculated with

$$\Delta N_{chem} = \sum_{i=1}^{\Delta N_{mag}} P_i \tag{48}$$

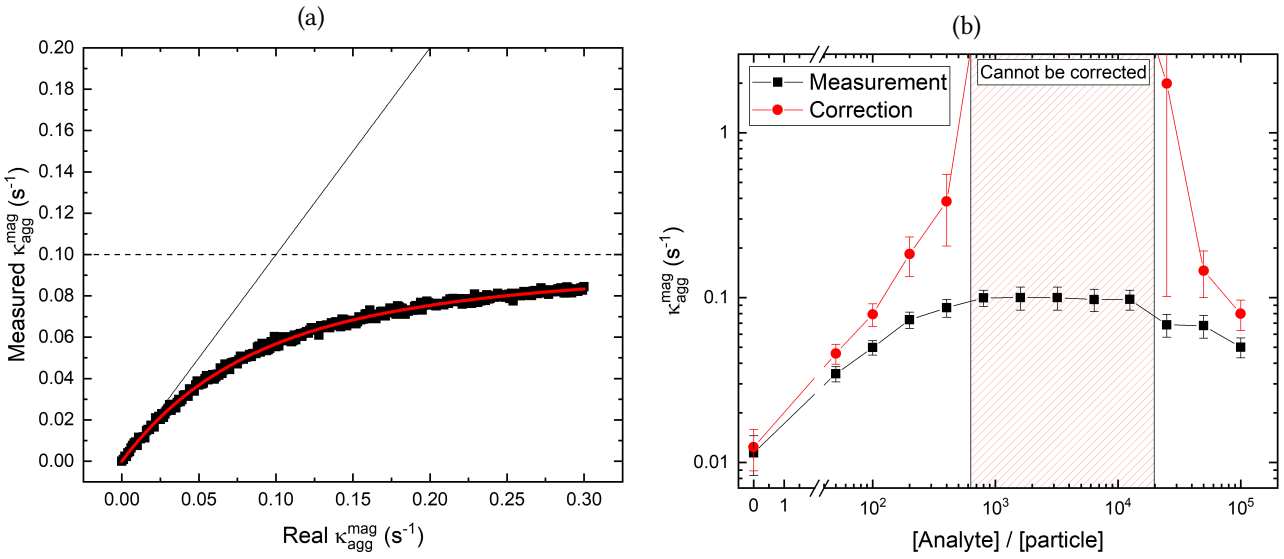

Fig. A.3: **Measured aggregation rate versus the real aggregation rate. (a)** This is the same graph as showed in Fig. 7.1b, but the plot of equation 50 is added (red line) with the values: $\Delta t = 1 \times 10^{-4}\,\mathrm{s}$, $t_{act} = 20\,\mathrm{s}$. **(b)** Measurement data and corrected data, the aggregation rate is plotted against the analyte concentration. The data in the middle could not be corrected because the measured rate is at the experimental limit, which would lead to a corrected rate that is infinite.

Under the assumption of a high formation rate κ_{form}, this sum can be approximated with an integral. Equation 44 can now be rewritten to

$$\kappa_{agg}^{meas} = \frac{\int_0^{t_{act}} dx \left[1 - (1 - \kappa_{agg}^{real}\Delta t)^{(t_{act}-x)/\Delta t)}\right]}{t_{act}} \frac{1}{t_{act}/2} \tag{49}$$

By solving the integral, the measured aggregation rate can be written as a function of the real aggregation rate:

$$\kappa_{agg}^{meas} = \frac{t_{act} + \frac{\Delta t - \Delta t(1-\kappa_{agg}^{real}\Delta t)^{(t_{act}/\Delta t)}}{\log(1-\kappa_{agg}^{real}\Delta t)}}{t_{act}^2/2} \tag{50}$$

This equation is plotted (red line) as a function of the real aggregation rate in Fig. A.3(a). This figure shows the same (simulated) data as Fig. 7.1b. The plot overlaps the simulated data perfectly. The inverse of equation 50 can be used to compute the real aggregation rate from the measured aggregation rate. Fig. A.3(b) shows measurement data (from Fig. 5.5) that is corrected with equation 50. Some data point could not be corrected because these points reach the experiments maximum, which would lead to an infinite aggregation rate.

Supplementary information

S1 Testing the annealing efficiency

The annealed docking strands are measured with a PAGE experiment as described is chapter 2. The results of this experiments are shown in Fig. S.1. This image shows the 11 wells that are used: the two outer wells contains the DNA ladder, the nine wells in between contains the three different samples at 3 different concentrations. The specific sample description are given in the figure. The numbers at the left and right of the image corresponds to the number of bases pairs of the DNA molecules in the DNA ladder. Most of the annealed DNA strands of the first three samples are after the PAGE experiment at the same place as the 35-basespared DNA molecule of the ladder. This indicates that the annealed strands are of the same size. From this result it can be concluded that the annealing succeed. However there are some DNA strands at the place of the 20-basespared DNA molecule, this position corresponds to the single stranded DNA molecules, thus some DNA strands are not hybridized.

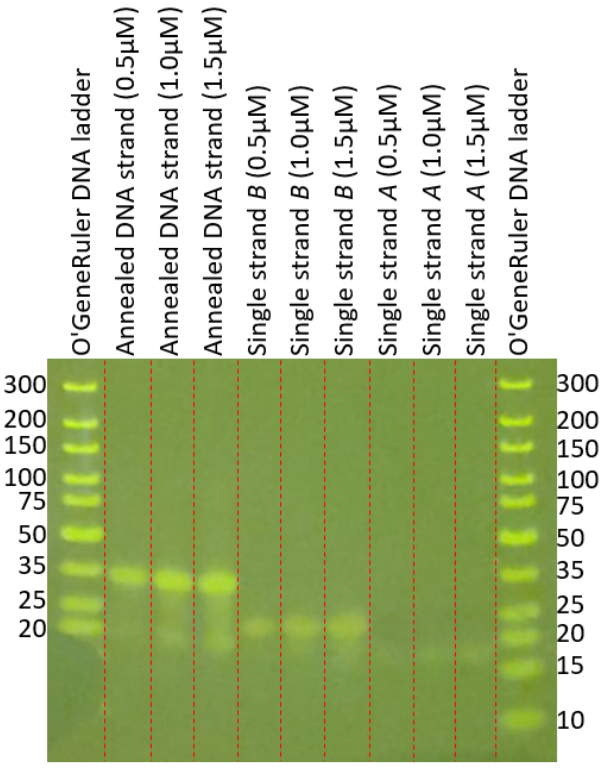

Fig. S.1: Image of the gel that shows the position of the DNA strands after the PAGE experiment. The numbers at the left and the right corresponds to the number of basepairs of the different DNA fragments in the ladder.

S2 Design of the DNA strands

In order to get an efficient annealing process and a reliable DNA sandwich assay the DNA strands should have the following requirements:

- Docking strand A and B should have a strong binding that should not break during a measurement: 20 nucleobases complementary
- Docking strand A can only bind in one way to docking strand B, or the other binding possibilities should be very weak bonds. The same holds for analyte strand A and B. This makes the annealing of the strand more efficient.
- The docking strand should have a strong binding to the analyte strand: 15 nucleobases
- Analyte strand A and B can only bind in one way to docking strand B to ensure that the only bond between the analyte strand and the docking strand is the strong one that survives the whole measurement.
- The hairpin melting temperature should be as low as possible for all four single stranded oligos, which makes the annealing process more efficient. The melting temperature of Analyte-B is a bit high, but a lower temperature could not be realized .

S3 Validation of BD simulation

The BD simulation is run several times to validate the results. By changing the magnetic field strength in an OMC experiments, the encounter process is accelerated. This should also be the result of the simulation. Also the initial particle concentration is changed. A higher concentration should also result in a larger encounter rate.

Fig S2 shows the simulation results of changing the field and the concentration. As expected, the number of clusters versus the time is higher for increasing field strengths and increasing concentrations. Increasing

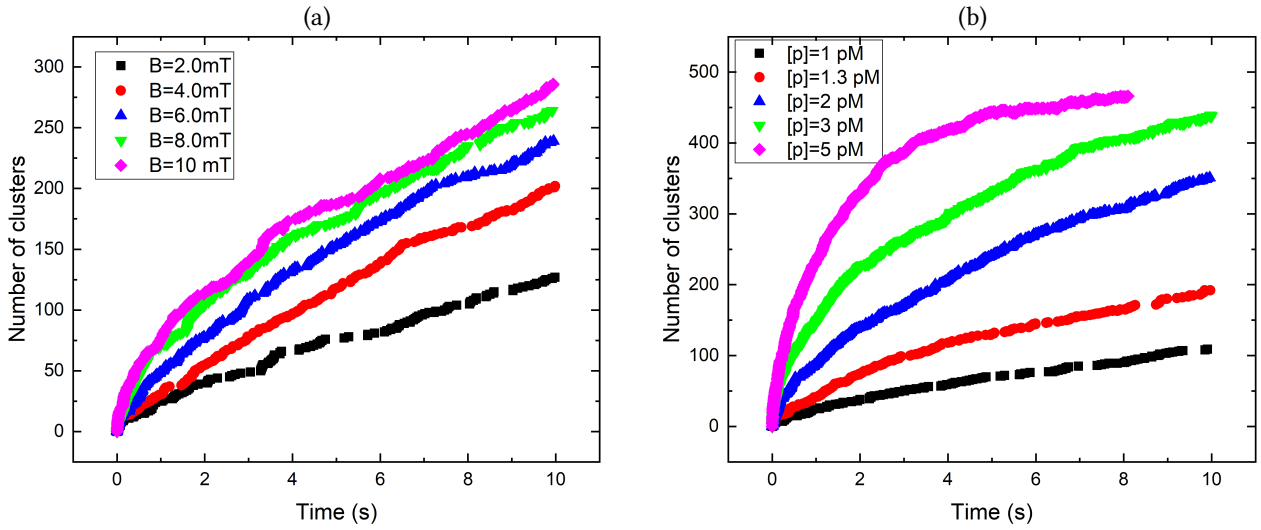

Fig. S2 **Simulation results.** The number of clusters are plotted versus the time, for varying magnetic field strengths and an initial particle concentration of $1.3\,\mathrm{pM}$**(a)**, and for varying particle concentrations and a constant magnetic field of $4\,\mathrm{mT}$ **(b)**.

the field strength with a factor 5 has less effect than increasing the concentration with a factor 5. This is because the encounter rate initially depends on Brownian motion. At distances smaller than about $3\,\mu\mathrm{m}$ the magnetic interaction become significant. At higher concentrations the average initial distance are decreased which causes faster encounter rates.

S4 Scattering simulation

In order to get quantitative insights in the light scattering by rotating dimers, a Mie-scattering simulation is used. This simulation has been developed by Mackowski et al.[36]. The simulation is performed using a $660\,\mathrm{nm}$ light source with S-polarization. The dimers consist of particles with varying diameter and a constant interparticle distance of $10\,\mathrm{nm}$.

For the simulations of the polystyrene and silica particles, sizes of respectively $536\,\mathrm{nm}$ and $511\,\mathrm{nm}$ are used, without any size dispersion. For the Ademtech particles the size varies from $200\,\mathrm{nm}$ to $800\,\mathrm{nm}$ to account for the large CV. The effective refractive index of the particle can be calculated with equation 51 [40].

$$n_{eff}^2 = n_{mat}^2 \frac{(1+2f_{gra})n_{gra}^2 + 2(1-f_{gra})n_{mat}^2}{(1-f_{gra})n_{gra}^2 + (2+f_{gra})n_{mat}^2}, \tag{51}$$

where n_{gra} and n_{mat} are respectively the refractive indices of the iron-oxide grains and the matrix material, f_{gra} is the volume fraction iron oxide. The volume fraction can be calculated from the weight fraction iron-oxide, which was determined earlier in this chapter. The derivation of the volume fraction iron-oxide is discussed in appendix A2 and is given by

$$f_{gra} = \frac{V_{gra}}{V_{total}} = \frac{\rho_{mat} f_{gra}^{weight}}{\rho_{gra} + f_{gra}^{weight}(\rho_{mat} - \rho_{gra})} \tag{52}$$

in which ρ_{gra} and ρ_{mat} are the densities of the iron-oxide grains and the matrix material respectively in $\mathrm{g\,cm^{-3}}$, and f_{gra}^{weight} is the weight fraction iron-oxide, which is 0.62 for the Ademtech, and 0.36 for the polystyrene and Silica particles. All the physical properties that are used in the above equations, as well as the calculated average volume fraction and refractive indices, are listed in the table 1. The iron-oxide in the microparticles is a mixture of magnetite and hematite, which have respectively a refractive index of 2.36 and 3.05. So the effective refractive index of the iron-oxide is somewhere in between and is estimated to be 2.7 ± 0.3.

The simulated scattering signal of the three different particle types is plotted in Fig. **??**a. For the Ademtech particles, two examples of dimers (one dimer consisting of a particle of $350\,\mathrm{nm}$ and a particle of $500\,\mathrm{nm}$, and one dimer consisting of a particles of $550\,\mathrm{nm}$ and a particle of $650\,\mathrm{nm}$) are simulated. Note that the y-axis of both graphs are not the same. The amplitude of the signal of the Ademtech particles is much larger than the signal of the polystyrene and silica particles, due to the larger effective refractive index of the Ademtech particles. This corresponds to a real measurement: the scattering signal of a sample with Ademtech particles in an OMC experiment is also much larger than a sample with silica particle. The measured Fourier amplitudes for the Ademtech, polystyrene, and silica particles are respectively 0.9, 0.3, and $0.09\,\mathrm{mV}$, at a particle concentration of $1.3\,\mathrm{mV}$.

Table 1: **Left**: The density and refractive indices of the materials iron-oxide, polystyrene and silica. **Right**: The average weight and volume fraction, and the refractive index of the three different particle types: Ademtech, Polystyrene, and Silica.

Material	Density	Refective index
Iron-oxide	$5.2\,\mathrm{g\,cm^{-3}}$ [41]	2.7 ± 0.3 [42]
Polystyrene	$1.1\,\mathrm{g\,cm^{-3}}$ [43]	1.582 [44]
Silica	$1.3\,\mathrm{g\,cm^{-3}}$ [43]	1.475 [45]

Particle type	f_{FeO}^{weight}	f_{FeO}	n_{eff}
Ademtech	0.62 ± 0.08	0.26 ± 0.03	1.83 ± 0.08
Polystyrene	0.36 ± 0.04	0.11 ± 0.01	1.68 ± 0.04
Silica	0.36 ± 0.04	0.12 ± 0.01	1.59 ± 0.04

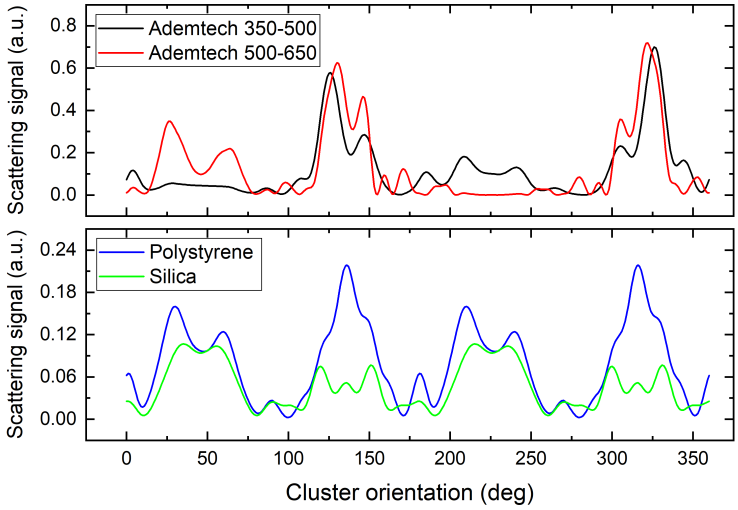

Fig. S3 **Results of the Mie-scattering simulation** The top graph shows the simulated signal that plotted as a function of the dimer orientation of two Ademtech dimers, one with particles of 350 and 500 nm, and one with particles of 500 and 650 nm. The bottom graph shows the simulated signal of a polystyrene and silica dimer. Note that the y-axis of both graphs is different.